MICROPATTERNED CHEMISTRY AND STRUCTURE IN LAYERED BIONANOCOMPOSITES

A Dissertation
Presented to
The Academic Faculty

by

Ruilong Ma

In Partial Fulfillment
of the Requirements for the Degree
Doctor of Philosophy in the
School of Materials Science and Engineering

Georgia Institute of Technology
August 2018

MICROPATTERNED CHEMISTRY AND STRUCTURE IN LAYERED BIONANOCOMPOSITES

Approved by:

Dr. Vladimir V. Tsukruk, Advisor
School of Materials Science and Engineering
Georgia Institute of Technology

Dr. Meisha L. Shofner
School of Materials Science and Engineering
Georgia Institute of Technology

Dr. Andrei G. Fedorov
George W. Woodruff School of Mechanical Engineering
Georgia Institute of Technology

Dr. Paul S. Russo
School of Materials Science and Engineering
Georgia Institute of Technology

Dr. Yulin Deng
School of Chemical and Biomolecular Engineering
Georgia Institute of Technology

Date Approved: June 15, 2018

Dedicated to my family and friends.

ACKNOWLEDGEMENTS

I am fortunate to have received an overwhelming amount of support at every step of my PhD studies from everyone around me. First, I would like to express my deepest gratitude to my advisor Prof. Vladimir V. Tsukruk for providing so much inspiration, knowledge, guidance, and car wisdom. Since joining SEMA Lab in September 2014, I have received so many opportunities to hone my technical and professional skills through participating in cutting-edge research, attending academic conferences, and working in an industry internship. I would also like to thank Prof. Meisha L. Shofner, Prof. Paul S. Russo, Prof. Andrei G. Fedorov, and Prof. Yulin Deng for their kind willingness to take part on my committee, delivering critical feedback to strengthen my work.

I would like to acknowledge all the past and current SEMA Lab members who have all played a key role in helping create this wonderful research environment. Special recognition goes to Dr. Kesong Hu, Dr. Weinan Xu, Dr. Ren D. Geryak, Dr. Chunhong Ye, and Dr. Rui Xiong for teaching me how to use research tools and introducing me to key materials concepts; and my project teammates Anise M. Grant and Michelle C. Krecker for valuable discussions over coffee. I also want to extend my gratitude to my strong network of research collaborators: Prof. Igor Luzinov from Clemson University and Prof. David L. Kaplan from Tufts University for help and insights on component processing; Changsheng Wu, Prof. Zhong Lin Wang, Dr. Daniel Gordon and Prof. Gleb Yushin for support on energy transduction.

Finally, I would like to acknowledge my parents, and my brother Toby for being awesome people, and for providing me boundless amounts of love and support.

TABLE OF CONTENTS

LIST OF TABLES

LIST OF FIGURES

LIST OF SYMBOLS AND ABBREVIATIONS

Acronym	Full term
AFM	atomic force microscopy
B. mori	*Bombyx mori*, common silk worm
CNC	cellulose nanocrystal
CNF	cellulose nanofibrils
DLS	dynamic light scattering
EDLC	electric double layer capacitance
E-beam	electron beam deposition
FEP	fluorinated ethylene polymer
FTIR	Fourier transform infrared spectroscopy
GO	graphene oxide
GO-SF	graphene oxide / silk fibroin composite
LbL	layer-by-layer
PDMS	polydimethylsiloxane
PR	photoresist
PTFE	polytetrafluoroethylene
rGO	reduced graphene oxide
SEM	scanning electron microscopy
SF	silk fibroin
SA-LbL	spin-assisted layer-by-layer
TEM	transmission electron microscopy
TENG	triboelectric nanogenerator
UV-Vis	ultraviolet-visible light spectroscopy
VAF-LbL	vacuum-assisted filtration layer-by-layer
XRD	x-ray diffraction
XPS	x-ray photoelectron spectroscopy
ζ-potential	zeta potential

SUMMARY

The quest for humankind's increased capabilities in gathering information, analyzing data, and controlling our surrounding environment is leading to a proliferation of connected physical objects that can sense, compute, and communicate. Conventional classes of electronic materials such as metals and semiconductors cannot meet this new demand alone due to challenges in scale, and ability to function in new use-environments such as on clothing, on skin, and in the human body.

In this research, 1D biopolymers (silk fibroin, cellulose nanocrystals) and 2D synthetic components (functionalized graphenes) are assembled into bio-derived nanocomposite papers. Through post-processing conversion of geometry and surface chemistry at the microscale, these biopapers are transformed into a platform for flexible and stretchable electronics for diverse applications including stretchable wiring, energy harvesting, energy storage, and haptic sensing. The key to realizing these applications is leveraging the intrinsic properties of nanoscale components through the controlled, localized application of annealing, cutting, printing and stenciling. Elements of directed microstructural design include patterned voids to generate algorithmic pop-up deformations, partial cuts to inhibit metastable buckling, conductive traces to enable sensory circuits, and interdigitated electrodes to support double layer capacitance. The set of techniques and the structure-property relations explored in this work can serve as a framework for understanding microstructural manipulation that is generalized across layered nanocomposites.

CHAPTER 1. Introduction

1.1 Background

The extreme environments endured by next-generation devices require robust lightweight multifunctional materials to assure success. For instance, clothing and apparel should not only protect against abrasive external forces, but could provide real-time monitoring of the wearer's health, and protect the wearer from noxious environmental agents.[1,2] High surface-to-volume ratio by nanoscale components also confer exceptional mechanical, electrical, thermal and optical properties not seen in traditional bulk materials. Bio-nanocomposites are materials interfaced at the nanoscale with bio-derived components, and represent an emerging class of sophisticated materials that has potential to meet these advanced characteristics.

One class of bionanocomposites, graphene-based biolaminates, have generated intense recent research interest, with many novel materials reported within the past year pushing the boundary of strength and toughness in flexible engineering materials.[3–9] Materials design affords novel, lightweight bionanocomposites that synergistically combine the structural and functional capabilities of constituent biotic and abiotic nanoscale components. This array of unique properties offers an opportunity to create devices that are not only strong and flexible, but with added functionalities in sensing, actuation, and energy transduction (Figure 1.1).[10–12]

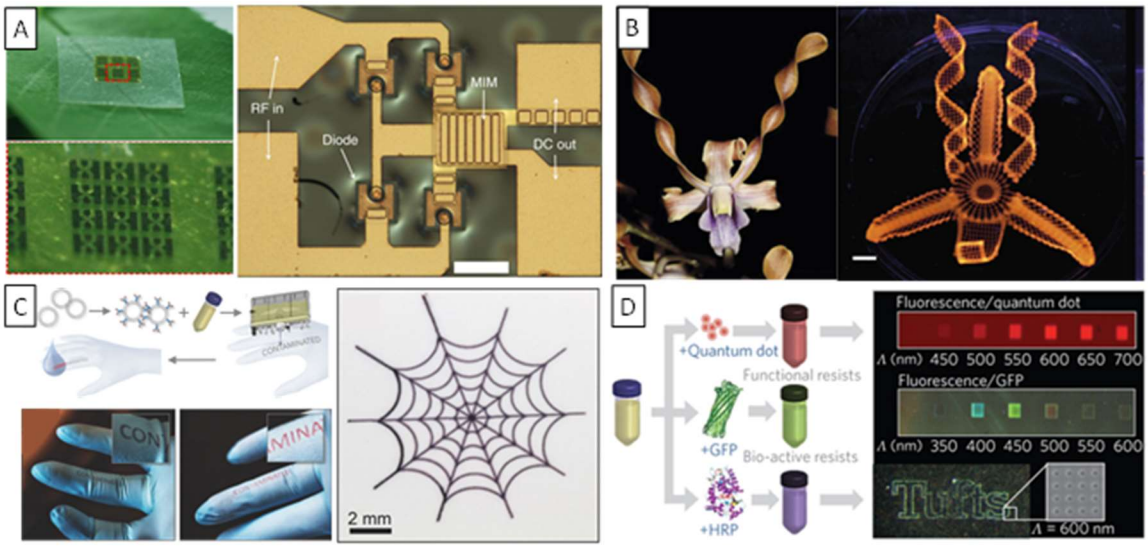

Figure 1.1. Cellulose (A,B) and silk (C,D)-based biocomposites as functional materials. A) Nanofibrillar cellulose as a biodegradable platform for flexible electronics.[13] B) Cellulose-loaded ink printed into biomimetic actuating 3D structures.[14] C) Printed silk ink loaded with bio-targeting agent undergoing color change upon contact with bacteria.[15] D) Silks loaded with bio- and chemi-active agents as water-solvated e-beam lithography resist.[16] (Reproduced from Creative Commons licensed work,[13] and with permission from copyright holders[14–16])

Publication trends show that interest in composites comprised of bio-derived components (silk and cellulose) and graphene components is accelerating. **Figure 1.2** plots the number of publications indexed in Elsevier's citation database with the keywords "composite", and "cellulose", "graphene" and "silk" respectively. In 2018, the number of publications on graphene composites is expected to exceed 6,500. However, the majority of research interest has focused on the use of bionanocomposites as passive materials for structural applications.[17–19] These works discuss the nanoscale engineering of component interfaces to achieve record-breaking mechanical properties including mechanical strength, yield strain, fracture toughness. However, comparatively few works discuss how to transform this new class of nanocomposites into active, functional materials that can leverage their unique features such as superior strength, toughness and flexibility.

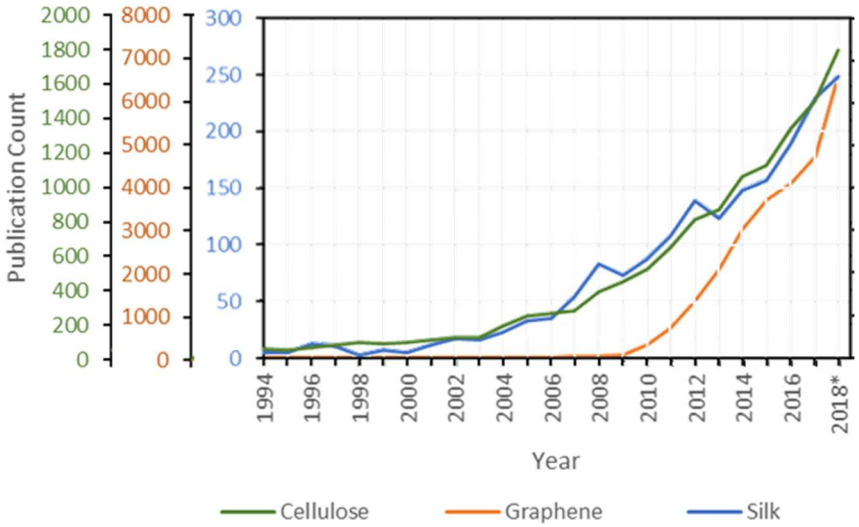

Figure 1.2. Number of publications index in Scopus on the topic of "cellulose-", "graphene-" and "silk- composites". Number of publications for 2018 is a straight-line projection from number of publications on topic as of May 1, 2018.

For instance, high-performance electronics typically utilize semiconducting materials such as instance silicon (Si), or III-V systems such as gallium arsenide (GaAs); and are integrated into rigid substrates such as copper-clad laminate (CCL).[20–22] These materials have advantages built upon decades of research and development from the semiconductor industry pursuing Moore's law for products such as integrated circuit components. Their rigidity enables the efficient performance of a task at a fixed form-factor. However, while all materials can be reversibly deformed at small applied strains, the rigid components of conventional electronics are prone to brittle fracture or permanent deformation at small strains, either of which can lead to device failure. Next generation pervasive devices such as sensors, energy tranducers, and optoelectronic components will require operation under diverse use cases that require fabrication on non-rigid material platforms.

1.1.1 Degrees of non-rigidity

Non-rigid material platforms can refer to a wide range of material classes according to how they behave to externally applied stresses (flexible materials, stretchable materials, soft materials), and according to the length-scale over which the permitted motion occurs (intrinsically non-rigid at material level, structurally non-rigid at macro/micro level). Flexible refers to materials and components that can retain functionality after undergoing bending, for surviving movement in the position of a hinge or joint. Stretchable refers to materials that can survive applied strains, and by proxy, a level of material robustness that also enables survival under compression, twist and complex deformations. The combination of flexibility and stretchability for instance, would enable materials to conform into new form factors on substrates ranging from textiles, moving machine components, and biological tissue. Additionally, softness entails materials whose deformation would not induce damage to surroundings. For instance, biological tissues such as fat tissue, internal body tissue linings and external body skin having elastic moduli of 10^2, 10^3 and 10^5 Pa respectively,[23] which is outside the range spanned by conventional electronic devices, but rather within the range of fluids, hydrogels and polymers, making them an ideal platform for components that interact safely, and comfortably in complement to living organisms.

1.1.2 Flex and stretch by geometry

The realization of non-rigid materials for electronics have primarily been driven by two types of approaches—1) the transformation of conventional electronic materials (i.e. metals, metal oxides, and semiconductors) through structure, and 2) the creation of new inherently non-rigid molecular assemblies (i.e. conducting polymers, percolating nanomaterials) that are conductive or electronically-active.

The first type of approach relies upon exploiting design of materials into configurations that introduce flexural properties. For instance, conventional electronic materials such such as metals (Cu, Al), metal oxides (ITO) and semiconductors (Si, GaAs) have limited bending and stretching tolerance (typically under one percent) in the bulk 3D state. However, by reducing one or more dimensions into micro- and nano-scale, the strain of bending decreases proportionally. Consider that in thin "film-on-foil" devices, the strain at the top surface film (ε_{top}) is defined by the film and substrate thicknesses (d_{film}, $d_{substrate}$) and bending radius (R) by the relation: $\varepsilon_{top} = (d_{film} + d_{substrate}) / (2R)$, whereby strain at the edge is directly related to the distance away from the neutral surface.[24] The increased flexural properties associated with reduced dimensions have been investigated for all classes of materials (metals, semiconductors, polymers, ceramics) in the form of 1D nanowires,[25–28] and in 2D nanomembranes.[29–32] Through control over the geometry of structurally thin materials, flexion can be engineered into stretch.

Notably, Rogers *et al.* pioneered the use of the controlled placement of silicon nanoribbons with fixed anchor points onto pre-strained substrates for geometry control, in structures referred to as 'wavy' silicon. The wavy silicon structures are capable of flexing, buckling,

and popping up.[33–35] However, because these techniques are built upon semiconducting materials such as Si, they rely upon complex, multi-step clean-room techniques including thinning of the Si substrate by hydrofluoric acid, and masked etching under ultrahigh vacuum conditions. As proof of concept, these wavy structures have been demonstrated as wireless skin-mounted antenna, as stretchable mounts of MOSFETs, and as sensors mounted in internal body tissue.[36–38]

Cuts placed into a thin 2D material, either by lithography or by laser-cutting, also provide a structural means to convert flexion into other desired properties such as stretchability and controlled buckling by invoking 2D material cutting (kirigami) with 2D material folding (origami).[39–42] Here, Kotov *et al.* notably demonstrated the applicability of kirigami techniques for the robust engineering mechanical properties in experimental paper and thin films material systems by laser cutting.[43] Preliminary works have also demonstrated simple rectangular kirigami cuts for applications as shape-morphing materials, diffraction gratings, and solar trackers.[44–47] Due to how recently research has begun on utilizing geometry controls, such as through kirigami cutting techniques, the application of these techniques to real-world use cases is an emerging area of research interest.

1.1.3 Flex and stretch through molecular assembly

The capacity to recover from deformations can also arise from design of the material at the molecular level. Rather than geometric deformations through buckles, waves or cuts, these materials contain polymeric molecules connected at physical or chemical entanglements,

and micro-cracks within the material that serve as a mechanical means to enforce recovery of deformations.[48,49] These extended entanglements and microcracks offer much higher recoverable strains than can be accommodated through stretching of crystalline lattice. Molecularly stretchable materials such as elastomers can be loaded with active electronic materials to form a composite that retain capacity to recover from mechanical deformations, and the properties of the active component. For instance, metal nanoparticles,[50–52] metal nanowires,[53–55] and conjugated polymers[56,57] have all been loaded into polymer-reinforced stretchable matrices. Some work has also gone into the chemical modification of electronically active molecules. Typically, these molecules are conjugated polymers with rigid backbones that do not permit significant bending or allow formation of entanglements. However, through introduction of modified side-chains and segmented back-bones, these molecules become more flexible, and better able to accommodate small strains while retaining conductivity or semiconductor properties.[58–61]

1.2 1D Bio-derived Components

Novel nanomaterials are often inspired by nature, which offers both the robust building blocks and innovative designs that can be leveraged to assemble next-generation functional nanomaterials. Figure 1.3 organizes by row the classes of earth-abundant materials used in this research (nanocellulose, silk, graphene oxide), while the columns show the different levels of organization within the material (raw source, secondary structure, primary structure).[17,62–65]

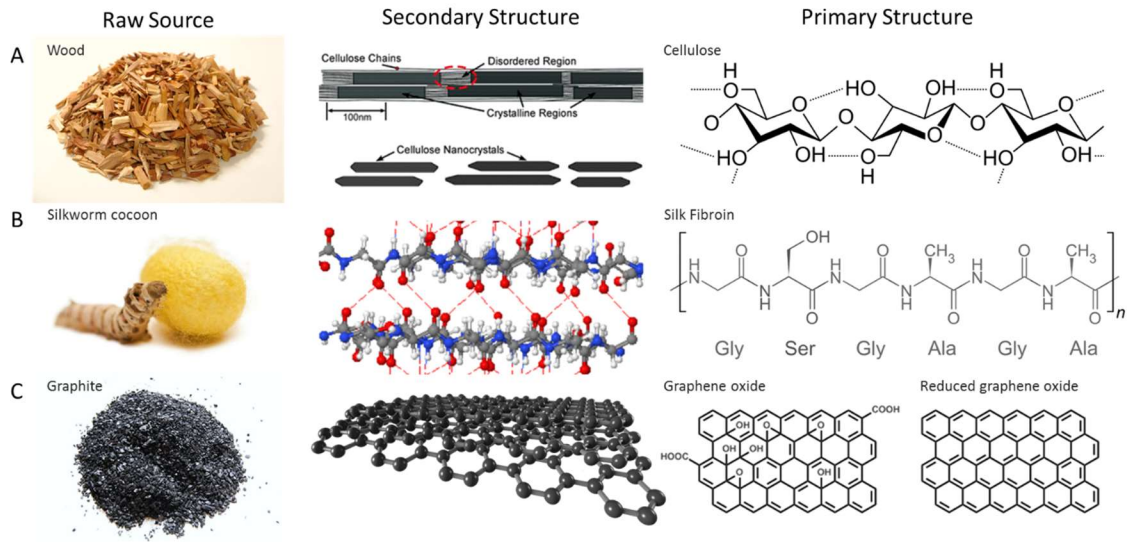

Figure 1.3. Comparison of structure and source of materials used as components in biopapers in this research: A) nanocellulose, B) silk fibroin, C) graphene oxide.[63,64,66] (Reproduced with permission from Creative Commons license images, and from copyright holders[63–65])

1.2.1 Silk Fibroin

Silk fibers extruded by spiders and the mulberry silkworm (*Bombyx mori*) have elastic moduli that rival the strongest commercial polymers as a consequence of their hierarchical organization (Figure 1.1).[66] The silk worm cocoon not only protects against predation and weather, but also blocks out solar radiation that could be detrimental to the developing pupae within.[65,67] Many species of plant and animal life produce materials with comparably intriguing properties that could be co-opted for applications engineered to meet technological needs.

Natural materials to be explored in the proposed study include naturally sourced silk, and cellulose nanomaterials. These bio-derived materials share favorable characteristics for materials processing, including being renewable, biodegradable, biocompatible, highly soluble in aqueous buffers and under ambient conditions, and rich in accessible surface

moieties for chemical modification.[62] Understanding the mechanisms and design features that can yield extraordinary properties in bio-derived polymers such as cellulose, and silk-based nanocomposites will enable the development of novel composites of bio-derived materials that mimic their properties for applications. Because these composites consist of bio-derived materials, they are often capable of degradation, reduced cytotoxicity, and enhanced bio-compatibility making them eco-friendly.[68–70] However, the ultimate realization of their extreme properties usually *requires addition of synthetic reinforcing components*.

1.2.2 Cellulosic Nanomaterials

Another attractive class of natural materials are nanocelluloses, an abundant, nearly inexhaustible natural nanomaterial that can be extracted from numerous organisms such as various plants, bacteria and tunicates.[26] Even at low nanocellulose content, these natural materials have shown exceptional reinforcement effects in the nanofillers-polymeric matrix due to their high tensile strength, anisotropic shape, ease of tuning dispersion, as well as their wide array of accessible complementary interfacial interactions facilitated by the dense network of surface hydroxyl groups. For example, the incorporation of only 1 wt.% cellulose nanofibers into the cellulose coatings results in a two-fold increase in Young's modulus.[71] Interestingly, when the concentration of cellulose nanocrystals in the nanocomposites exceeds a critical value, a unique self-assembly of 1D rigid cellulose nanocrystals can result in spectacular liquid crystalline (LC) organization, possessing the splendid iridescent structure color.[63]

The fundamental unit of nanocellulose is a highly crystalized rigid 1D nanostructure with diameter of 3 nm, consisting of 5-6 parallel rigid cellulose molecular chains bonded by hydrogen bonding.[72] This structure provides individual nanocellulose particles with excellent mechanical characteristics with elastic modulus as high as 150 GPa, comparable to that of Kevlar fibers (Figure 1.4a).[73,74] Another notable example of nanocellulose nanocomposites is its combination with 2D materials to build up a matrix-free bionanocomposites.[17]

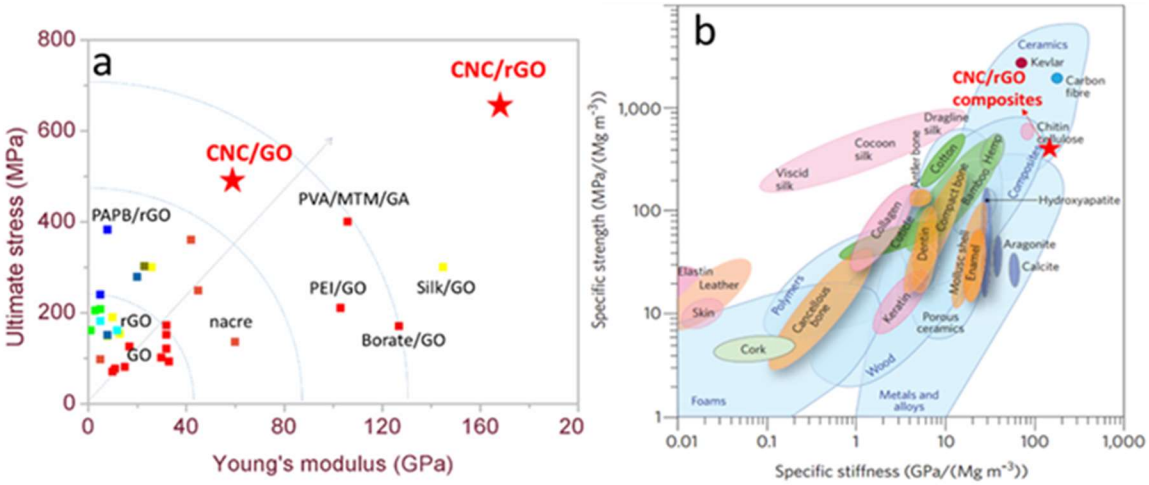

Figure 1.4. Comparison of mechanical properties between (a) layered bionanocomposites, and (b) the both natural and artificial materials.[75] (Reproduced with permission from copyright holder)

Inspired by hierarchical natural nanostructure, various nanocomposites have been constructed from 1D nanocellulose and 2D materials with exceptional mechanical properties far exceeding natural and synthetic composites both in terms of absolute strength values (Figure 1.4a) and in terms of specific (per mass) strength (Figure 1.4b). Additionally, this unique combination not only results in the largely enhanced mechanical performance, but also significantly benefit other additional functionalities. For example, super-insulating, fire retardant and highly anisotropic foams can be constructed through

freeze-casting suspensions of cellulose nanofibres, graphene oxide and sepiolite nanorods.[1] These foams exhibit excellent combustion resistance and exhibit a thermal conductivity of 15 mW m^{-1} K^{-1}, superior to conventional polymer-based insulating materials.[76] Additionally, nanocellulose materials possess a low coefficient of thermal expansion of $5*10^{-6}$ K^{-1} and high optical transmittance (98% at 550 nm)—making these materials attractive for flexible transparent electronic devices.[77]

Nanocellulose can be isolated from natural hierarchical structural materials such as wood and bamboo by different fabrication methods, including acid hydrolysis, mechanical treatment and bacterial synthesis.[78] These nanocelluloses combine important natural materials properties—such as hydrophilicity, broad chemical-modification capacity, biodegradability, and biocompatibility—with phenomenon arising from its nanosize-scale such as its high aspect ratio (up to several hundreds), high rigidity, and large surface area. Nanocellulose materials can be classified into three main categories: cellulose nanocrystals (CNC), cellulose nanofibers (CNF) and bacterial nanocellulose (BNC) based on their cellulosic source and on the processing conditions. CNC generally only contains highly crystallized nanostructures, while CNF and BNF consists of highly crystalline arrangements and slightly perturbed domains referred to as amorphous region, which can provide them more flexibility than stiff CNC structures.[78]

1.3 2D Synthetic Graphene Components

1.3.1 Graphene Oxide Flakes

Graphene oxide (GO) is widely used as a functional derivative for graphene or as a precursor for pure graphene due to its bulk quantity availability, as well as its dispersibility and processability under aqueous conditions (**Table 1-1**).[79,80] Its single atomic layer structure possesses a high density of epoxy and hydroxyl groups across the basal planes and carboxyl groups at sheet edges (up to 30% of surface area).[64] Graphene oxides have been shown to increase the oxygen barrier of composites so it is expected that various combinations of modified GO and biopolymers could arise for advanced applications that have hitherto largely been limited to passive barrier applications (**Table 1-1**).[81,82]

For instance, the incorporation of graphene oxides increases the tensile strength of composite films to several hundred MPas while preserving an elastic modulus around 3 GPa.[83,84] In laminated bionanocomposites, an extremely high elastic modulus of 170 GPa and high strength of 650 MPa can be attained--both parameters much higher than any values reported for regular GO nanocomposites with only synthetic components.[83] Moreover, graphene-containing nanocomposites show impressive functional properties such as tunable (semi-) conductivity, unique photonic/optical transportation, and fluorescence quenching.[18] Furthermore, recent work has shown remarkably high toughness of 4 MJ m^{-3} in cellulose nanocrystal-graphene oxide membranes (Figure 1.4a).[75]

By leveraging the complex surface chemistry of graphene and graphene derivatives, a myriad of surface chemical structures can be functionalized to the graphene basal plane or plane edge. In both exfoliated graphene and graphene oxide, π-π stacking (10-50 kJ/mol) and van der Waals interactions (0.5-5 kJ/mol) can serve as driving forces for the nonconvalent conjugation with molecules, nanoparticles, and polymers, especially those with extended π-conjugated systems and strong hydrophobic character.[85,86] The abundance of hydroxyl and epoxy moieties present in GO sheets open a route to noncovalent functionalization by means of ionic dipole interactions (50-200 kJ/mol) and hydrogen bonding (12-30 kJ/mol) (Figure 1.5).[87] Although these noncovalent interactions leveraged for binding graphene derivatives are significantly weaker than individual covalent interactions (i.e. carbon single bond dissociation energy is 350 kJ/mol), they are reformable, abundant, and do not interrupt the underlying graphene electronic or chemical structure (Figure 1.5).

1.3.2 Modified and Functionalized Graphenes

Graphene derivatives (such graphenes, graphene oxides, and their chemically modified derivatives) are considered among the most promising synthetic components for nanocomposites (**Table 1-1**). Graphene-containing bionanocomposites can be modified and tuned for specific applications, and possess enhanced robustness, strength, enhanced tunable conductivity, and tunable transport/barrier properties. Many of these materials have dual functionalities (e.g., mechanical reinforcement and induced electrical

conductivity) and have been utilized as actuating elements for artificial muscles or as mechanical enhancing elements with antimicrobial properties.[88,89]

Table 1-1. Recently report graphene composites with other bio-derived materials.

Bio-derived material	Surface Modification	Method of assembly	Reported Application	Challenges	Ref
Chitosan	Nitrene reduced; pendant sulfonation,	Drop cast	Biosensors, packaging, actuation	Poor ordering and low mechanical strength	68,69
Polylactic acid	Starch	Compression molding	Thermally stable, structural, gas barrier film	Low mechanical strength and gas barrier	90
Cellulose acetate	Sulfonated poly (ether-ether-ketone)	Drop cast	Strong, thermally stable, gas barrier film	Low mechanical strength and gas barrier	91
Sodium Alginate	Tetraethylene pentamine	Drop cast	Strong, thermally stable, biodegradable film	Low mechanical strength	92
Polylactide	Grafted polylactide	Drop cast	Bone replacement, packaging	Aggregations, low transparency	70

The diversity and abundance of strategies available for functionalizing graphene derivatives means that there are many accessible surface chemistries for the graphene components to interact with its surrounding matrix in graphene-based biocomposites. These modifications not only tune the solubility of graphene flakes, but may also impart advanced functional properties including tuning band properties by doping,[88,93] changing surface absorptivity to select molecules,[89,94] tuning inter/intra-sheet charge transport,[95,96] modifying bio-response,[97] modifying single-sheet mechanical properties,[98] modifying sheet lubricity,[99,100] and serving as handle for decoration of GO flakes with functional components such as metal nanoparticles, quantum dots, aptamers and antibodies.[87,101] A few studies also demonstrate that through sequential application of two or more functionalization strategies, different modifications can simultaneous exist on individual

graphene oxide flakes.[102–104] This recent explosion in development of novel chemical strategies for functionalizing graphene derivatives opens up extensive opportunities for the utilization of these novel functional graphenes as a constituent component in natural polymer composites-- not only for structural applications, but also for functional applications such as in sensing and actuation (Figure 1.5).[105–111,111–131]

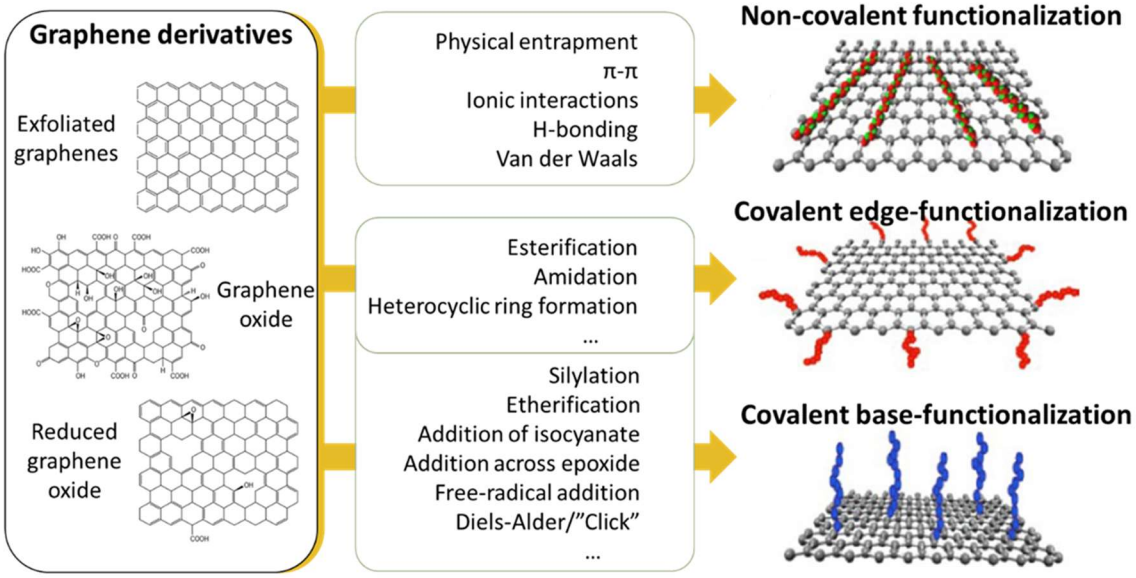

Figure 1.5. A highly diverse set of non-covalent and covalent routes toward functionalizing graphene derivatives along the sheet edge and basal plane. Illustrations are modified from recent review on graphene functionalization.[91]

To date, graphenes have been implemented in a variety of sensing, biosensing, and actuation applications. However, these works have been primarily limited to the application of pristine graphenes, and not the diverse gamut of functional graphenes, or their composites with the diverse bio-derived materials.[133–135] Functional graphenes can have tunable basal plane stiffness, variable conductivity, and can act as platform to support decoration by ligands, polymers, and bio-targeting agents that enable additional response to environmental conditions such as changes in ionic strength, pH, temperature, moisture,

or presence of targeted molecules. The confluence of emerging properties that could be incorporated into graphene sheets via facile synthetic processing (i.e. physical entrapment, covalent and non-covalent binding) (Figure 1.5), opens the possibility of implementing functionalized graphenes in a variety of sensing, biosensing, and actuation applications rarely explored to date.[87]

1.4 Processing Nanocomposite Biopapers

To assemble the component materials into robust, strong biocomposite papers, two classes of methods will be used: layer-by-layer (LbL) assembly, and one-pot assembly approaches (**Figure 1.6**).[136–138] Subsequently, printing and cutting processes will be invoked to generate additional functionalities in the biopapers.

1.4.1 Assembly of Nanocomposite Biopapers

The LbL technique allows for the placement of selected components with nanoscale precision within multilayered matrices which can be released to a free-standing state for further investigation or post-processing. LbL shows diversity in substrate materials, capable of assembling components via spin-coating and spray-coating on diverse substrates such as flat wafers, flexible films, fibers, particles, fibers and textiles.[136,137]

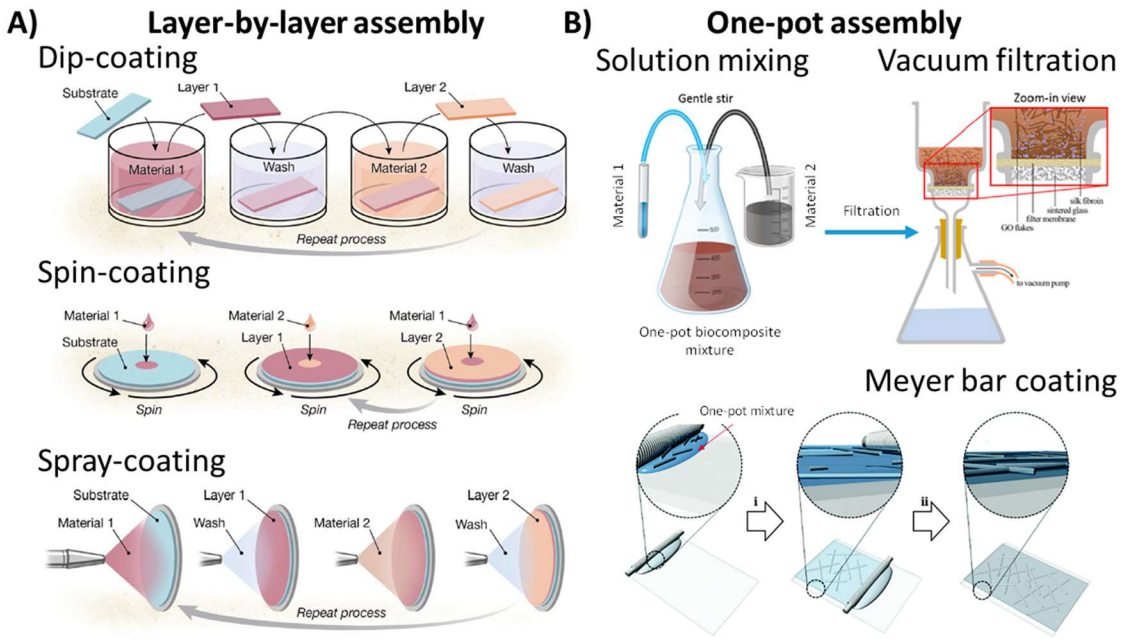

Figure 1.6. Assembly of organized bionanocomposites by A) layer-by-layer methods,[139] and B) one-pot assembly.[140,141]

An alternative path to biocomposite materials is via a one-pot directed assembly mixing. This method overcomes major obstacles for developing laminated structures such as cost, and time, allowing for the realization of nanocomposites with high efficiency and on a large scale (**Figure 1.6**). This method affords improved solubility and compatibility of the bio-derived constituents and inorganic materials and, therefore, may result in highly homogeneous materials, a critical challenge in the case of conventional LbL assemblies.

On the other hand, it gives an opportunity to obtain well-defined and stratified films with precisely designed laminated morphology, structure, and composition at the nanoscale level, which cannot be accomplished when casting solution mixtures. The bioderived and synthetic components used in this research will be co-dispersed and assembled by vacuum-assisted filtration over a nanoporous membrane or by Meyer rod casting to yield layered bio-papers (**Figure 1.6**).[137] Varying the mass of components deposited can be further

exploited to assemble freely standing films of variable thickness (from 100 nm to 50 μm).[142–144]

1.4.2 Post-Processing of Nanocomposite Biopapers

The generation of anisotropic stresses in multicomponent layered composite materials also enable designs for actuating and sensing elements.[145–148] In graphene-derivatives, internal stresses can be generated via selective anisotropic surface treatment of graphene composite, or contact of graphene composite with a material with thermal/solvent triggered expansion. Existing methods of patterning of graphene oxide nanocomposites for these purposes can be divide into mask based pattern techniques (e.g. lithography), and direct-pattern techniques (e.g. printing or write process).[141,149,150] Recent works have demonstrate laser-triggered graphene fibers actuators,[145] ionic strength triggered actuation of laser-scribed pristine graphene oxide films,[146] and electric-field triggered actuation of graphene-silver nanoparticle composites.[147]

While these reports demonstrate the potential of graphene-based materials in actuation and sensing devices, there is a dearth of graphene-natural polymer composites for such applications. Unlike pristine graphene-based materials, graphene biocomposites have added functionalities induced by biopolymers, including the possibility of assembly under ambient temperature and pressure conditions without requiring toxic reagents. Also, researchers have shown that 3D printing can be used to fabricate graphene materials in

complex patterns.[148,151] Such techniques can progress the implementation of graphene composites in solar cells, sensors, circuit boards, transistors, and LEDs.

In our recent study, the mechanisms of GO reduction by aluminum and deprotonation of GO moieties by humidity were invoked to develop a sensor element that is activated by human touch (Figure 1.7).[152] Touching the interface between GO and the deposited Al coating produces a strong voltage reading on the order of hundreds of millivolts. This setup can resolve very fast (20 Hz) repeated tapping by the human finger. We found that this device design is also specific to touch by a human finger, as the presence of salts activate the interfacial reduction of GO and triggers the voltage response.

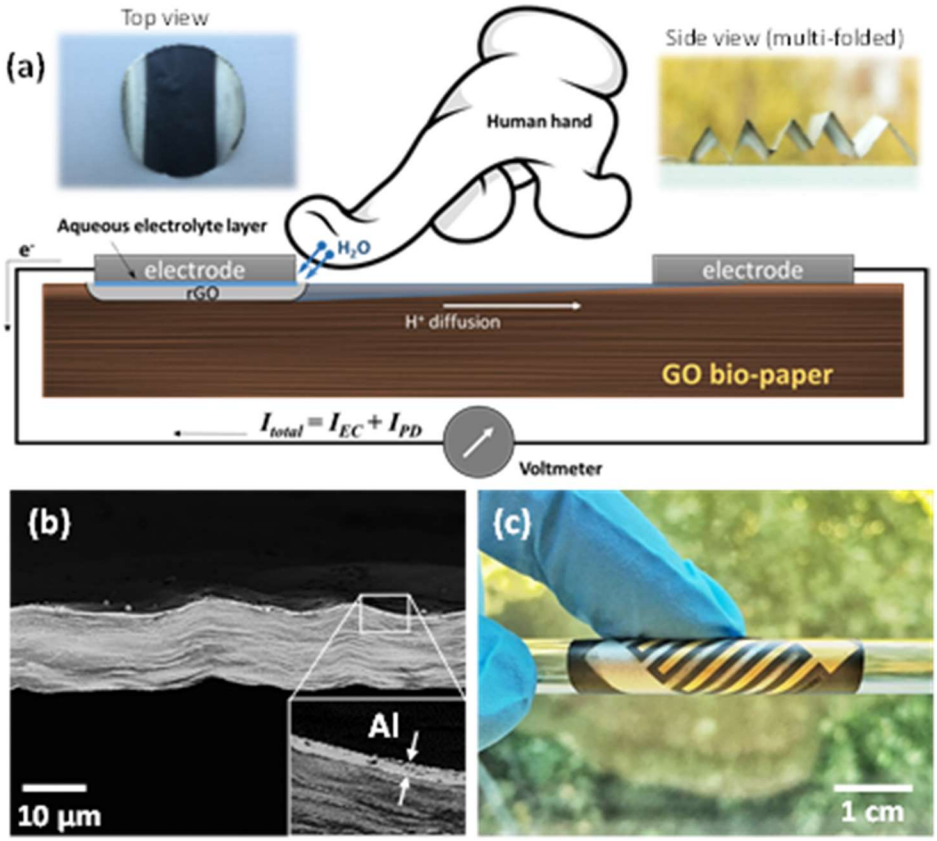

Figure 1.7. a) The moisture-injection behavior of a symmetrical GO-Al junction pair as a bio-tactile touch sensor. b) Layered microstructure of GO bio-paper beneath GO-Al electrode. c) Bending robustness of interdigitated Al and Au electrodes.[132]

1.4.3 Fabricating 3D and Stretchable Structures

Large volume top-down fabrication schemes of functional biocomposites have largely been confined in two dimensions, whereas three-dimensional shapes enable more complex, hierarchical organization of molecules through non-covalent interactions. The facile conversion of 2D bionanocomposites into 3D shapes extends the advanced properties designed in 2D films toward associated sensing and actuation applications that can interact with the 3D world. The combination of the ease of 2D fabrication with the functionality of 3D structures has rarely been demonstrated to date. Whereas the processing of bulk materials either through casting or extrusion cannot generate micro- or meso-scale architecture by design, methods for generating high resolution 3D structures such as 3D printing or 3D photo-fabrication techniques are fundamentally serial in nature, and cannot produce components in sufficient volumes beyond prototyping or customization applications.[151,153] To date, there are few approaches capable of converting 2D films into organized 3D hierarchical structures (**Figure 1.8**).[33,43,154] Existing strategies are largely based on lithographic cutting, then generating interfacial stresses to induce self-folding in the material whether through the interface of dissimilar materials, or through transfer of stresses along pre-defined points of contact.

External stresses can also be applied to the material to induce deformations to accommodate differential interfacial stresses distributions. For instance, Rogers *et al.* use lithography to generate kirigami cuts in an ultrathin silicon structure in the shape of serpentine twists, pinned to an elastomeric substrate at select anchor points. Compression of the substrate causes the elevation of unanchored features off the substrate into the z-

dimension. Kotov *et al.* employ lithography to generate cuts into graphene films, whereby deformation induces folding of the 2D film in the z-dimension.[43] Hu *et al.* also demonstrate using the solidification of water in GO hydrogels to induce the formation of a highly porous cellular structure formed by 2D graphene flakes.[150] The 2D architecture is well defined by the crystallization in the GO solution prior to freeze drying with the porous 3D structure withstanding high compressive strains.

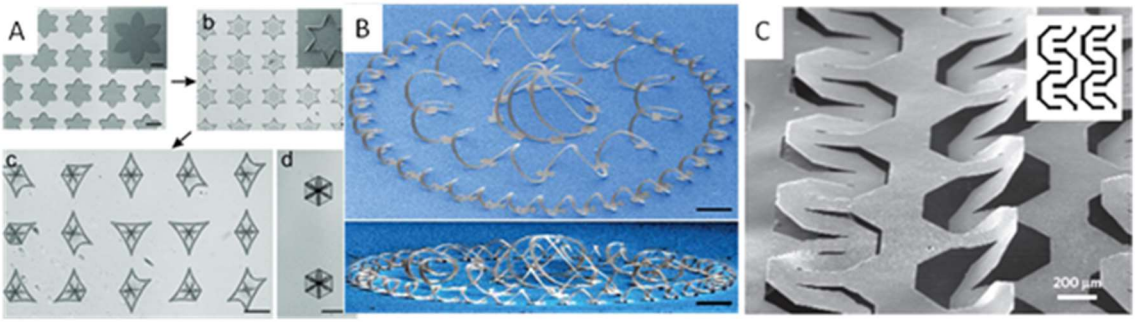

Figure 1.8. A) External source of stress inducing the extension of 2D structure into third dimension. B) Serpentine thin silicon patterns on strained elastomer. C) Lithography generated kirigami for stretchable graphene films.

We suggest that exciting recent advances, particularly in the areas of refining, functionalizing and assembling nano-scale 1D bio-derived components and 2D graphenes, will lead to the design of next-generation bionanocomposites aimed on application spaces beyond simple structural or passive applications. Accelerating development of these nanomaterials for multifunctional structural, sensing, barrier, and energy transduction applications requires developing a deep understanding of interfacial interactions between nanoscale components, and how sophisticated assembly techniques can guide synergistic micro- and nano-structural organization to control emergent additive physical properties.

CHAPTER 2. Research Design and Objectives

The overarching goal of my research is to establish the chemical and physical manipulation of layered bionanocomposite systems, or biopapers, localized across micro length scales. Controlling layered material behavior at this length scale is key to leveraging the unique properties arising from nano-scale interactions to produce effects at human-centered length scales (**Figure 2.1**). Whereas miniaturized devices for ubiquitous sensing, energy storage, and system components have traditionally been fabricated from hard materials with a fixed form-factor, and assembled from relatively rare or toxic components (i.e. metals, semiconductors)—layered nanocomposites is a new class of materials that harness the inherent exceptional flexibility, mechanical strength, mechanical robustness and chemical stability of its polymeric components.

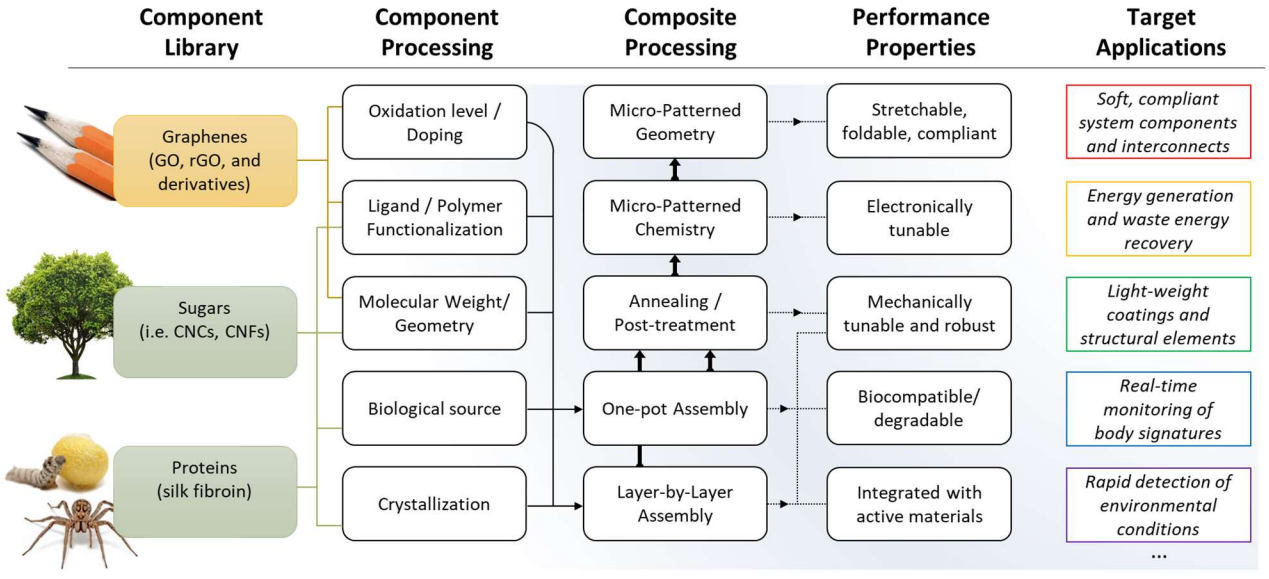

Figure 2.1. A systems approach for the rational design of hierarchically structured biopolymer-graphene nanocomposites for diverse structural, energy, and sensing applications.

Previous published works in the field of bionanocomposites control final composite properties through a narrow focus on parameters within component processing and composite assembly.[18,19,155] The major theme of this dissertation is to exploit intrinsic properties of the constituent components through micro-patterned post-processing (**Figure 2.1**, see 'composite processing' column) to generate a host of new emergent properties such as stretchability, tunable electronic properties, and tunable mechanical robustness. Combining these previously unexplored composite processing parameters yields a gamut of new performance properties, and consequently opens these materials for use in new application areas of such as for energy harvesting, flexible interconnects, and environmental sensing.

This research theme is realized through the accomplishment of the following specific objectives:

- Introducing functional synthetic components (graphene oxide sheets, graphene derivatives) to into nanocomposite biopapers as levers for microstructural control over mechanical and electronic properties.
- Using a combination of assembly and post-processing approaches such as guided assembly, large-scale printing, lithographic techniques, and drag-knife cutting to fabricate bionanocomposites with well-defined micro- and nanoscale materials with patterned electrical conductivity and enhanced mechanical properties.
- Manipulating GO-SF biopaper surface chemistry through the directed micro-patterned reduction of the graphene component. Through parametrizing reduction conditions, highly complex reduction patterns can be transferred rapidly onto the robust biopapers, with great control over material properties such as conductivity,

luster, mechanical strength, and hydrophilicity; and derived properties such as double layer capacitance, and energy harvesting capacity.

- Applying inspiration from kirigami (art of cutting) and origami (art of folding) methodologies toward the directed micro-patterned geometry of bionanocomposite papers. This enables the fabrication of constructs capable of functioning under extreme mechanical flex and stretch states. Through kirigami, we realize redistributed applied stresses via the generation of patterned cuts using high-throughput techniques that also enable the transformation of well-defined 2D-patterned features into complex 3D configurations for prospective applications in pop-up electronics.
- Advancing orthogonal control in bionanocomposite materials over critical functional properties such as mechanical robustness, stretchability, and electrical conductivity as a base for high fidelity sensing elements and energy storage and harvesting devices from nanocomposite biopapers.

A bionanocomposite model system was used to investigate these objectives. Two classes of 1D biopolymers, polypeptides (i.e. silk fibroin) and polysaccharides (i.e. nanocellulose), are assembled with synthetic 2D components (functionalized graphenes) to yield stable, robust layered graphene-based biopapers. These biopapers are judiciously manipulated in post-processing steps (annealing, micro-patterned chemistry, and micro-patterned geometry), leveraging nanoscale properties to adopt structural and chemical changes at the microscale. Localized and bulk material property changes are investigated by a suite of characterization tools to build understanding of structure-property relations. These

findings are leveraged for proof-of-concept devices and components fabricated into GO bionanocomposites.

The prospective results of this research are to embed powerful new functionalities into layered bionanocomposites, beyond applications as passive, structural materials for weight/size-reduction. The work presented here shows how highly localized control over structure and chemistry across areal dimensions at the micro-length scale allows for new methods to tuning macroscopic properties in bionanocomposites, transforming this class of materials into an active material for prospective applications in real-time sensing, energy storage, and energy harvesting.

Preparation of materials components, tools for understanding their fundamental organization and properties, and approaches for assembling and processing composites is summarized in the following chapter.

CHAPTER 3. Research Methodology

3.1 Component Selection and Processing

3.1.1 Silk Fibroin

Aqueous suspensions of 50 mg/ml regenerated silk fibroin (SF) will be prepared from the cocoon of the *Bombyx mori* by degumming, dissolving, purification, and dialysis based on a procedure described by Kaplan *et al*.[156] Silk cocoons are boiled in an aqueous solution of 10^{-2} M sodium carbonate for 30 min and washed against water to remove the sericin to yield SF fibers. SF fibers are dissolved in 9.3 M LiBr at 60°C for 2 hours. Centrifugation was used to separate residual aggregates and impurities from the dissolved SF in supernatant. The dissolved SF is dialyzed (using 3 kDa MWCO dialysis membrane) against ultrapure 18.2 MΩ water to yield 2 mg/ml SF.

3.1.2 Nanocellulose Materials

Aqueous suspensions of cellulose nanomaterials are produced from cellulosic fibers by acid hydrolysis (cellulose nanocrystals, CNCs), and homogenization (cellulose nanofibrils, CNFs). The properties of resultant cellulose nanomaterials (CNs) are dependent on hydrolysis conditions, time and cellulosic source—with typical CNCs with a diameter of 5-10 nm, and length of 100-300 nm, and typical CNFs 3-4 nm in diameter, and several microns in length.[78]

3.1.3 Graphene Oxide

Aqueous solutions of 2 mg/ml graphene oxide (GO) is prepared from natural graphite powder (325 mesh, 99.999% purity, Alfa Aesar) using a modification of the method proposed by Hummers.[157] In a typical preparation, graphite flakes (10 g) and sodium nitrate ($NaNO_3$, 5 g) are thoroughly mixed with 98% sulfuric acid (H_2SO_4, 200ml) while keeping the mixture temperature at 0°C. Potassium permanganate ($KMnO_4$, 30 g) is then added to the mixture while keeping mixture temperature at 20°C. The reaction is allowed to initiate at 35°C for 30 minutes before adding 500ml of water and bringing the reaction vessel to 98°C for 15 min. 1.5-L of water is added to the reaction vessel, lowering the temperature and arresting the reactions. Hydrogen peroxide (H_2O_2) is titrated dropwise to reduce residual permanganate. GO flakes are purified by cycles of centrifugation and washing to yield GO flakes suspended in water at pH 3.

3.2 Bionanocomposite Assembly

3.2.1 One-pot GO Biopapers by Vacuum Filtration

One-pot GO biopapers is assembled by vacuum filtration using a method based on Ruoff *et. al.*[144] The pH of the GO solution is adjusted to 10 by titration with 1M NaOH. The pH-adjusted GO dispersion is added to a bio-derived polymer suspension (i.e. silk fibroin solution at a 98:2 GO:SF weight ratio). GO-biopolymer dispersions are mixed by stirring,

and dried via vacuum filtration on an acrylic copolymer membrane filters to yield GO-SF films with areal dimensions fixed by the filter and thickness defined by GO-SF volume.

3.2.2 One-pot GO Biopapers by Cast-Drying

Large-area GO biopapers, easily exceeding hundreds of cm^2, can be formed from cast-drying a GO-biopolymer dispersion onto a fluorinated ethylene polymer (Teflon FEP, DuPont) sheet to yield. Drying is conducted in a humidity chamber (typically 50% RH) to slow the rate of drying, and reduce residual stresses arising from dissimilar drying on exposed and unexposed surface. The cast bionanocomposite films are removed from their FEP backings to yield large-area, freestanding films across large areas (hundreds of cm^2 in studies reported here).

3.2.3 Layer-by-Layer GO Biocomposites by Spin-Casting

Layer-by-layer (LbL) biocomposite films is formed by spin coating alternating layers of GO solution and bio-derived polymer onto a silicon wafer-bit coated with a polystyrene sacrificial layer based on a method developed in our group.[158] For example, 0.2 wt% silk fibroin solution can be alternatively spun-cast with a 0.04 wt% GO dispersion to yield nanomembranes that are free-standing after dissolution of the sacrificial layer.

3.3 Biopaper Post-Processing

3.3.1 Patterned Reduction of GO Biopaper by Screen Printing

Localized reduction of GO-based films is produced by printing an aluminum (Al) metallization paste (EFX-37, Monocrystal) using a semi-automatic screen printer (MPM SPM-V, Speedline Technologies).[159] Alternatively, patterned reduction is accomplished using a hobbyist setup for low-cost screen printing of GO-SF, and using a polyester screen with a laser-cut (Q-switched Nd:Ylf 1047 nm, Resonetics) paper stencil. Residual solvent in the Al-patterned GO biopaper is removed by treatment in vacuum oven (60 °C, 10 minutes). The Al-patterned GO biopaper is then be dampened with ultrapure water (18.0 MΩ-cm), and sandwiched between PTFE blocks for overnight. Subsequent rinsing under a stream of ultrapure water, then isopropanol, will then remove the patterned Al to yield conductive reduced GO features in the negative image of the stencil.

3.3.2 Patterned Reduction of GO Biopaper by Photolithography

High resolution localized reduction is performed by using a resist-mask patterned via photolithography to act as a shadow mask. Briefly, a resist is spin-coated onto the GO biopaper. The resist is soft baked, exposed through a chrome photomask, hard baked, then developed in a solvent that dissolves regions revealing underlying GO biopaper. An electron-beam deposition process is used to bring unmasked regions of the GO biopaper into contact with the anodic reducing metal (typically Al). The GO in contact with the reductant is dampened with ultrapure water, and sandwiched between PTFE blocks for 4

hours. Rinsing away the deposited metal, and dissolving the residual resist yields conductive patterns written into the GO biopaper in the negative of the photomask.

3.3.3 Cutting by numerical controlled dragknife

Micro-structured cuts are made in GO-based bionanocomposites using a two-step water-vapor plasticization followed by numerical controlled cut by dragknife. Briefly, the GO-SF biopaper is mounted onto a vinyl substrate release liner (OraCal 651), then placed in a ~100% RH environment for one hour. The water-plasticized bionanocomposite is cut by a 60° carbide blade from Tormach under computerized numerical xy-control (Silhouette CAMEO 3), and manual z-depth control via knife overhang. Cut structures can form full and (mountain- and valley-) partial cuts that enable control over bionanocomposite stretching and buckling.

3.4 Characterization

3.4.1 Atomic Force Microscopy (AFM)

Topological, phase and nano-scale mechanical properties were bionanocomposites were probed using atomic force microscopy (AFM), using the Bruker Dimension ICON and Dimension 3000 instruments. AFM measurements were typically conducted under tapping mode with Si cantilever tips with resonant frequencies ranging from 100 to 500 kHz , a

spring constant of 50 N/m, and tip radius of 15 nm as verified by tip reconstruction with calibration grating.

3.4.2 Fourier Transform Infrared (FTIR) Spectroscopy

A Bruker Vertex 70 FTIR was used to study protein secondary structure at bionanocomposite interfaces. The layered bionanocomposite is assembled on top of an attenuated total reflectance (ATR) crystal by spin-casting. Sample layers interact with the evanescent wave of the attenuated beam as an IR interferogram, which is transformed by software to an IR spectrum. For silk studies, the spectra from the amide III band (1200-1300 cm^{-1}) was used due to its insensitivity to ambient humidity conditions.

3.4.3 Confocal Raman Spectroscopy

A WITec Alpha 300R confocal Raman microscope was used to analyse and map Raman signatures from graphene components in bionanocomposites. In particular, we focused mapping the graphene Raman D and G bands to evaluate extent of reduction, damage to graphene flake, and carbon hybridization state. We used a Nd:Yag 514-nm laser at 0.5 mW was used, taking a 1-second exposure per pixel for mapping measurements, and 30 integrations of 1-second exposures for single-point spectra.

3.4.4 X-ray Photoelectron Spectroscopy (XPS)

Information about elemental composition and chemical state was collected using a Thermo Science K-Alpha x-ray photoelectron spectroscopy (XPS) system. X-ray source spot size was selected to be 30-μm to target regions that have patterned and unpatterned reduction features. XPS survey spectra with binding energy up to 1400 eV was collected to compare elemental composition. High-resolution elemental spectra (i.e. C 1s,.) were collected and fitted to elucidate elemental chemical states (i.e. C-C, C-H, C-O, O-C=O). Binding energy shifts were normalized against adventitious carbon at 284.4 eV.

3.4.5 Tensile/Compressive Test

Mechanical properties of macroscopic bionanocomposites were gauged using a Shimadzu EZ-SX tester. A typical biopaper coupon has dimensions 30 mm × 2 mm × 40 μm, and is tested under tensile mode at a rate of 0.5 mm/s. The tensile test mode was also used to stretch GO-SF biopapers processed by dragknife kirigami for 1D stretch pattern slits, and 1D stretch slits with controlled buckling by partial cuts.

3.4.6 Bulging Test

Stress-strain measurements for ultrathin (i.e. <10-μm) membranes were collected using an in-house bulging test setup. Nanomembranes are supported on a circular aperture TEM

grid (i.e. 50-300 μm gap). Using a vacuum setup, a force is applied to the membrane. Film bulging toward the vacuum is tracked using a 632.8 nm He-Ne laser setup by interferometry. The central point deflection, *d*, is obtained by tracking the number of interference bright-dark transitions (one transition cycle at 316.4 nm of deflection), and is correlated to film strain, whereby $\varepsilon = 2d^2(3r^2)^{-1}$, whereby ε is film strain, , r is aperture radius. Vacuum pressure is correlated to film stress by the relationship $\sigma = Pr^2\ (4hd)^{-1}$, whereby σ is stress and P is vacuum pressure.

3.4.7 Ellipsometry

Optical and thickness parameters of LbL bionanocomposite films, and single-material spin-coated films (i.e. analysis of SF and GO source) was collected and modelled using a Woollam M-2000U spectroscopic ellipsometer. Raw ellipsometry data was fitted using a Cauchy model.

3.4.8 Scanning Electron Microscopy (SEM)

Surface morphology of processed bionanocomposite papers were observed using secondary-electron imaging on Hitachi S8230 field-emission SEM operating with voltage deceleration due to prevalence of charging on polymeric samples. Reduced micro-features on biopapers exhibit less charging due to movement of collected charges along conductive pathways, showing charge contrast on SEM images.

3.4.9 Transmission Electron Microscopy (TEM)

Transmission electron micrographs were collected using a Hitachi HT7700 TEM. For imaging crack propagation, LbL bionanocomposite films are suspended in a 50-300 μm circular-gap TEM grids. Using the vacuum from mechanical bulging test, the grid-supported film is ruptured, and imaged on TEM at 80 keV, and objective aperture 4 to reduced effect of beam damage.

CHAPTER 4. Enhancing GO-SF biopaper mechanical properties by water-vapor annealing

4.1 Introduction

We demonstrated that much stronger and robust nacre-like laminated GO (graphene oxide)/SF (silk fibroin) nanocomposite membranes can be obtained by selectively tailoring the interfacial interactions of "bricks"-GO sheets and "mortar"-silk interlayers via controlled facile water vapor annealing. This annealing has been utilized to relax the secondary structure of silk backbones confined between flexible GO sheets, and leads to a significant increase in ultimate strength (by up to 41%), Young's modulus (up to 75%) and toughness (up to 45%). We suggest that silk recrystallization is initiated in the proximity to GO surface by the hydrophobic surface regions serving as nucleation sites for β-sheet domains formation and followed by SF assembly into nanofibrils. Strong hydrophobic-hydrophobic interactions between GO layers with SF nanofibrils result in enhanced shear strength of layered packing. The work presented here not only gives the better understanding of SF and GO interfacial interactions, but also provides insight on how to enhance the mechanical properties for the nacre-mimic nanocomposites by focusing on adjusting the delicate interactions of heterogeneous "brick" and adaptive "mortar" components.

Nacre-like materials show distinctive laminated structure with superior mechanical properties. Nacre consists of 95 wt% aragonite and 5 wt% softer organic biopolymers that

result in a layered structure 1000-fold tougher than its constituent components.[160–162] Such extraordinary enhancements to mechanical properties have been attributed to nacre's highly regular brick-and-mortar structure.[17,163,164] However, the notion of making a nacre-like brick-and-mortar structure seems to be deceptively simple and easy to emulate, the fact is that it's extremely difficult in reality. Not to mention there are no processing techniques capable of generating composites with high mineral content in a large scale at present.[73] The translation of natural design motifs also requires a deep understanding of the mechanical behavior of materials and interfaces in volumes down to the nanoscale.[89]

Current fabrication methods for nacre-like materials include: (1) conventional synthetic methods adapted for bulk ceramic materials (2) freezing casting, (3) layer-by-layer (LbL) assembly, (4) electrophoretic deposition, (5) flow-assisted mechanical assembly (e.g. vacuum filtration) and (6) chemically-driven self-assembly.[167–174] Among these techniques, spin-assisted layer-by-layer (SA-LbL) assembly is one that allows for accurate control of hierarchical laminated structure with well-defined component packing.[75,175] Precisely tailoring the thickness, size, and surface roughness of each layer allows structural control down to the nanoscale and tunable mechanical performance. The optimized distribution and dispersion of components result in highly enhanced mechanical performance with improved characteristics, which, however, should be improved to become highly competitive.

For further improvement of nacre-like materials, there should be careful consideration on the selection of bricks and mortar components. The alignment, shape and roughness of the

"bricks" must be controlled and the interfacial properties of components should be matched. Graphene oxide (GO), a two-dimensional carbon material with rich functional groups on its surface, outstanding mechanical properties, high flexibility, and aqueous processability, is an excellent ''brick'' component for fabricating the robust brick-and-mortar structures. Graphene/graphene derivatives were combined with different organic components composite materials such as dopamine/poly (dopamine),[173,174] PVA,[164] chitosan,[7] and cellulose.[75] On the other hand, silk fibroin (SF), a natural fibrous protein derived from silkworm silk with multidomain structure, amphiphilic properties and adjustable secondary structures, is not only known to be one of the strongest natural biomaterials, but also could be regarded as a promising candidate for "mortar" in nacre-like laminated structures.[67,176] Several examples of high performance GO-SF laminated materials have been reported to date.

As these studies clearly demonstrate, carefully engineered interfaces between components are crucial in designing organized robust laminated materials.[165,177] Not only the organic component should be engineered to template the nucleation and growth of the mineral phase at the nanometer level, but also, the interfaces in the materials should be designed to avoid catastrophic failure at a large scale.[17,168,172] However, to the best of our knowledge, the focus of current studies on preparing high mechanical performance nanocomposite materials is mainly on choosing different brick-and-mortar components without full exploration of their matching properties. Even for some studies that focus on interfaces, the emphasis is on utilizing surface chemistry to enhance interfacial adhesion. Less attention is paid to tailoring local and global conformation of flexible backbones in close proximity to the interfaces. Through local relaxation of the soft component, it is expected

to realize more ordered structure and optimized the interface interaction, thus facilitating further enhancement of their mechanical performance.

In such nanocomposites with biopolymer mortar, water could play a key role to tune the soft component. It can create higher free volume, alternate the intermolecular interactions, reduce steric hindrance for movement and reorientation, and promote/hinder local crystallization.[178] For silk materials, Kaplan *et al.* conduct temperature-controlled water vapor annealing to demonstrate controllable crystallinity.[179] Previous work also showed the delicate and hierarchical interaction of graphene and SF components.[180] For example, during the reduction of GO, SF could assemble into nanofibrils and covered whole reduced GO sheets.[181,182] Thus, we speculate that water vapor annealing could be a promising way for further tailoring interfacial interactions of SF with GO in the nanocomposites in a broad range.[183]

In this work, we explore water vapor annealing as an effective method for achieving significant improvement in strength, elastic modulus and toughness in GO/SF nanomembranes. We suggest that through water vapor-initiated annealing, SF recrystallization could be induced by hydrophobic surface regions of GO flakes which serve as nucleation sites for β-sheet formation followed by SF assembly into nanofibrils. The well-ordered morphologies of GO layers and SF nanofibrils with high content of β-sheet domains are obtained with higher interfacial interactions between SF and GO components. These changes lead to the concurrent increase in toughness, Young's modulus and ultimate strength. The work presented here not only gives a better understanding of SF and GO interfacial interactions, but also provides insights on how to

enhance the mechanical properties for the nacre-mimic materials by tuning interfacial interactions.

4.2 Methods

The graphene oxide suspension, prepared by Hummer's method and re-dispersed in methanol, remained stable with no visible sedimentation for months. AFM of one time GO deposition by spin coating reveal a GO-layer thickness of 1-2 nm, corresponding to the major proportion of single GO sheet with a minor proportion of stacking GO layers (Figure 4.1a). This observation illustrates that GO monolayers in methanol can be easily transferred onto a substrate with uniform surface distribution and no aggregation, which is the foundation to realize the accurate control of hierarchical structure.

The thickness and the volume concentration of GO in the nanomembrane could be tuned from 9.7% to 53.7% by adjusting the concentration of GO suspension and SF solution (see Supporting Information). The thickness growth of GO/SF nanomembrane shows linear behavior with repeated deposition of GO and SF components. The thickness increment per bilayer is 5.2 nm. This value is common for such components which corresponds to 1 nm thick GO and about 4 nm thick silk layer. The inset of **Figure 4.1**b shows an optical micrograph of a representative nanomembrane freely suspended on a 300 μm aperture as was prepared for bulging testing. These suspended nanomembranes are flat, uniform, freely-standing, do not show cracks, pinholes, or wrinkles can sustain stresses associated with film transfer.

4.2.1 Water vapor annealing conditions

Annealing temperature and timing are the main factors to be considered in water vapor annealing experiments. As has been demonstrated, the crystallinity of silk materials increases with increasing annealing temperature from room temperature to 95 °C.[179] In this study, water vapor annealing was conducted at 40 °C, 60 °C and 80 °C which should promote steady crystallinity increase (β-sheet formation) among the whole crystallinity range. Also, since the kinetics of crystallization by water vapor annealing is not the focus in our study, all annealing time are set to be 20 hours to assure full transformation.[179] GO/SF nanomembranes with GO volume concentration of 26.9 % and intermediate mechanical characteristics were chosen as the example for illustration of typical changes (**Figure 4.1**).

As known, bulging test is a common procedure for evaluating mechanical properties for films that are too thin for traditional tensile tests. **Figure 4.1**c shows the typical stress–strain curves of the GO/SF nanomembranes derived from the bulging test data in accordance with this method. The residual stress of 20–70 MPa is caused by the shrinkage during drying on aperture.[184] From typical stress–strain curves, we can conclude substantial improvement of mechanical characteristics such as ultimate stress and Young's modulus, with ultimate strain remaining unchanged after annealing (**Figure 4.1**d). After water vapor annealing at 40 °C, nanomembranes show a 12% increase in ultimate stress along with a 20 % increase in Young's modulus. After 60 °C, 31% increase in ultimate stress along with 41% increase in Young's modulus. However, when annealing

temperature rises to 80 °C, both the ultimate stress and Young's modulus show no significant differences and, as known, long time high temperature treatment may bring thermally induced degradation.[178,185] Thus, 60 °C annealing was selected for the basis of subsequent morphological and mechanical behavior studies.

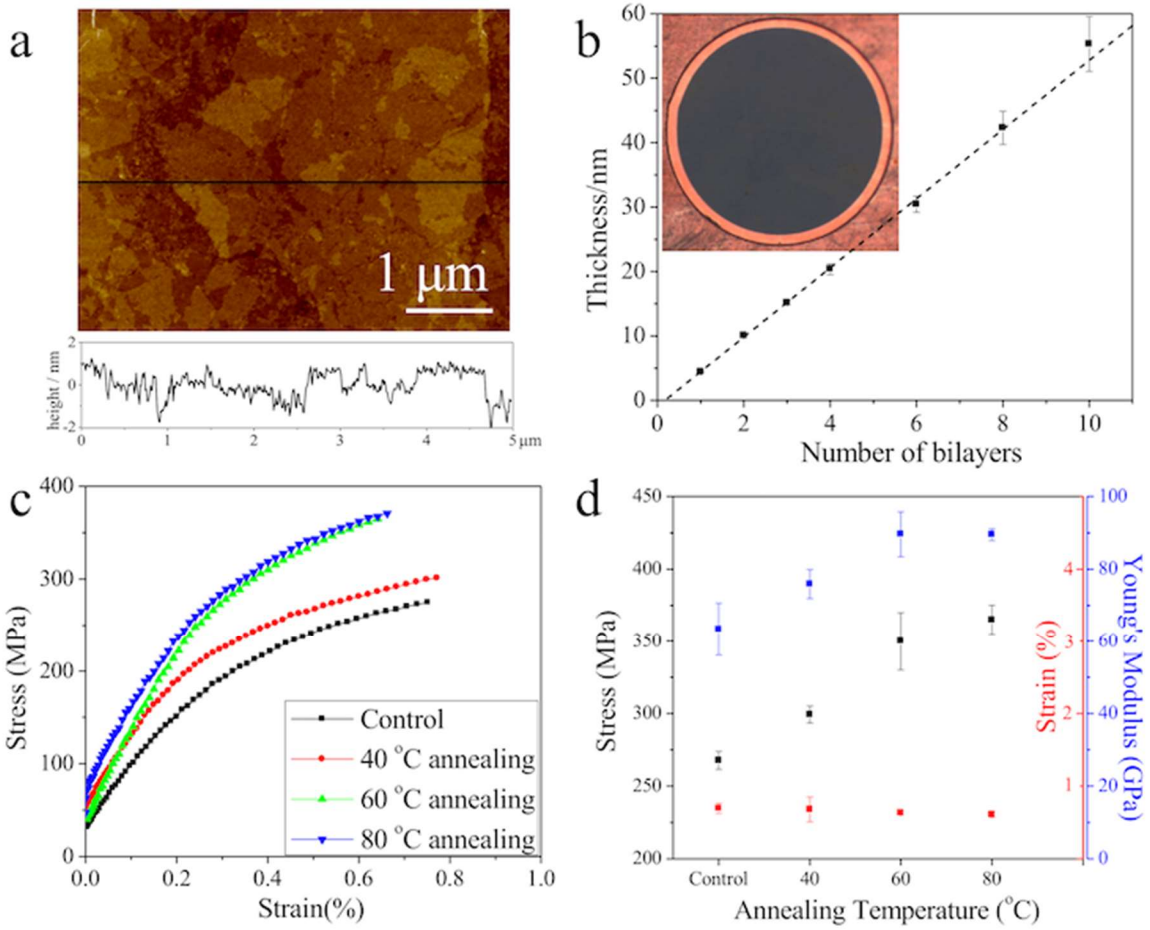

Figure 4.1. (a) AFM topographical image of a monolayer GO flakes on silicon wafer, the concentration of GO in methanol is 0.75 wt% (z-scale: 5 nm). (b) Ellipsometry data of the thickness of the GO/SF membranes (GO volume concentration of 26.9 %) increases with the number of the GO/SF bilayers assembled and the linear fitting curve. Inset: optical image of the membrane suspending on a 300 μm copper aperture. Mechanical properties of the nanocomposite membranes: (c) Representative stress–strain data from bulging tests at different annealing temperature; (d) The ultimate stress, ultimate strain and Young's modulus of the GO/SF nanomembranes at different annealing temperatures.

4.3 Results and discussion

4.3.1 Morphological and mechanical properties of GO/SF nanomembranes

GO/SF nanomembranes with different GO content from 9.7% to 53.7% were investigated water vapor annealing effects. First, it is worth to note that the thickness of all nanomembranes after annealing does not change significantly in comparison with initial samples stored at room temperature (**Figure 4.2**a,b). All nanomembranes show uniform surface morphology across large surface areas without significant aggregation and excessive wrinkling. The root-mean-square (RMS) roughness of GO/SF nanomembrane with 10 bilayers is relatively low, 2.6 nm ± 0.3 nm within 5 μm × 5 μm surface area (**Figure 4.2**c). After annealing, the surface morphology of GO/SF nanomembranes stays homogeneous as well with RMS roughness remaining unchanged, around 2.4 nm ± 0.2 nm (**Figure 4.2**d).

However, high-resolution AFM images show some difference in fine surface morphology: globular-like SF clusters for the samples before annealing show a trend to aggregate into the nanobundles with the common length below 100 nm and further forming SF nanofibrils at longer times (**Figure 4.2**f).

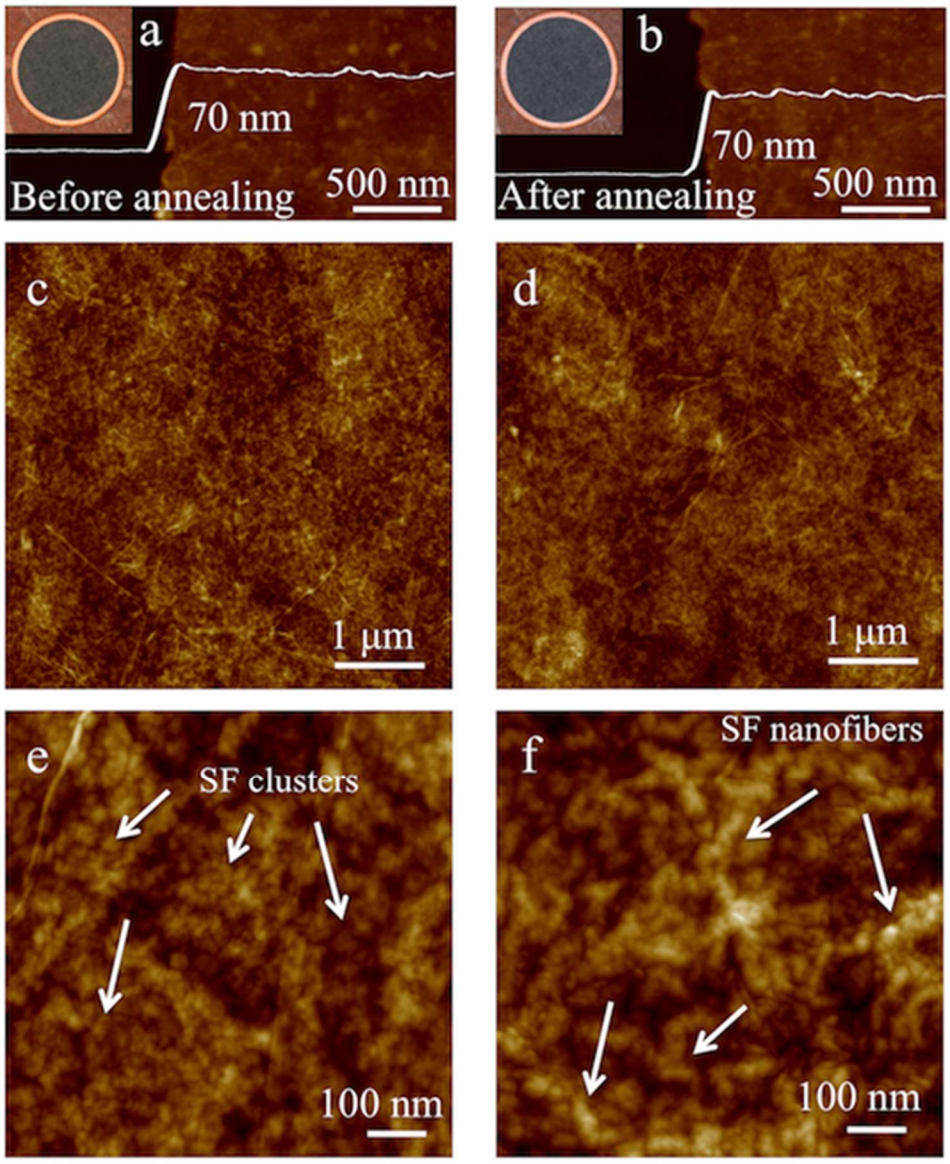

Figure 4.2. (a, b) The thickness evaluation of the GO/SF nanomembrane (GO volume concentration of 9.7%, 8 bilayers) before and after annealing with the section profile derived from the film edge. Inset: optical image of the membrane (GO volume concentration of 9.7%, 8 bilayers) suspending on a 300 μm aperture before (a) and after (b) annealing. (c, e) Surface morphology of the GO/SF nanomembrane (GO volume concentration of 26.9 %, 10 bilayers) before annealing (c, z-scale: 20 nm; e, z-scale: 10 nm). (d,f) Surface morphology of the GO/SF nanomembrane (GO volume concentration of 26.9%, 10 bilayers) after annealing (d, z-scale: 20 nm; f, z-scale: 10 nm)

4.3.2 Mechanical properties of GO/SF nanomembranes

Figure 4.3a shows the stress–strain curves of the GO-SF nanomembranes with different GO content acquired before and after annealing. It should be noted that the GO component we used is re-dispersed in methanol for better spreading. And, as known, methanol can induce β-sheet secondary structure in contrast to traditional aqueous dispersions. For direct comparison, the SF control sample was prepared by alternatively spin coating SF solution and methanol to minimize the difference influenced by different β-sheet content of SF matrix. The ultimate stress, Young's modulus and toughness of purely SF control sample are measured to be 120 ± 8 MPa, 13 ± 1 GPa and 1.1 ± 0.1 MJ/m^3, respectively. Further addition of GO component resulted in the dramatic rising of the ultimate stress and Young's modulus (**Figure 4.3**a,b,d).

The highest value achieved is for the nanomembranes with GO volume concentration of 53.7%, with ultimate stress of 326 ± 31 MPa, an increase of 170 %; the Young's modulus increases to 95 ± 9 GPa, an increase of 620 %, and the toughness increases to 1.53 MJ/m^3, an increase of 40 %. It's a common trend for composite materials with a good dispersion of nanoscale reinforcing components and strong interfacial interactions as was observed for many GO-based materials.[83,84,186] After water vapor annealing, the mechanical characteristics increased further. The highest values have been achieved for the nanomembranes with GO volume concentration of 53.7% after water annealing: ultimate stress of 460 ± 65 Mpa, Young's modulus of 105 ± 10 GPa and toughness of 2.1 ± 0.3 MJ/m^3, all characteristics among the highest values for GO based nacre-mimic

nanocomposites achieved to date.[83,164,173,174,176,183,186] Mechanisms behind this reinforcement will be discussed below.

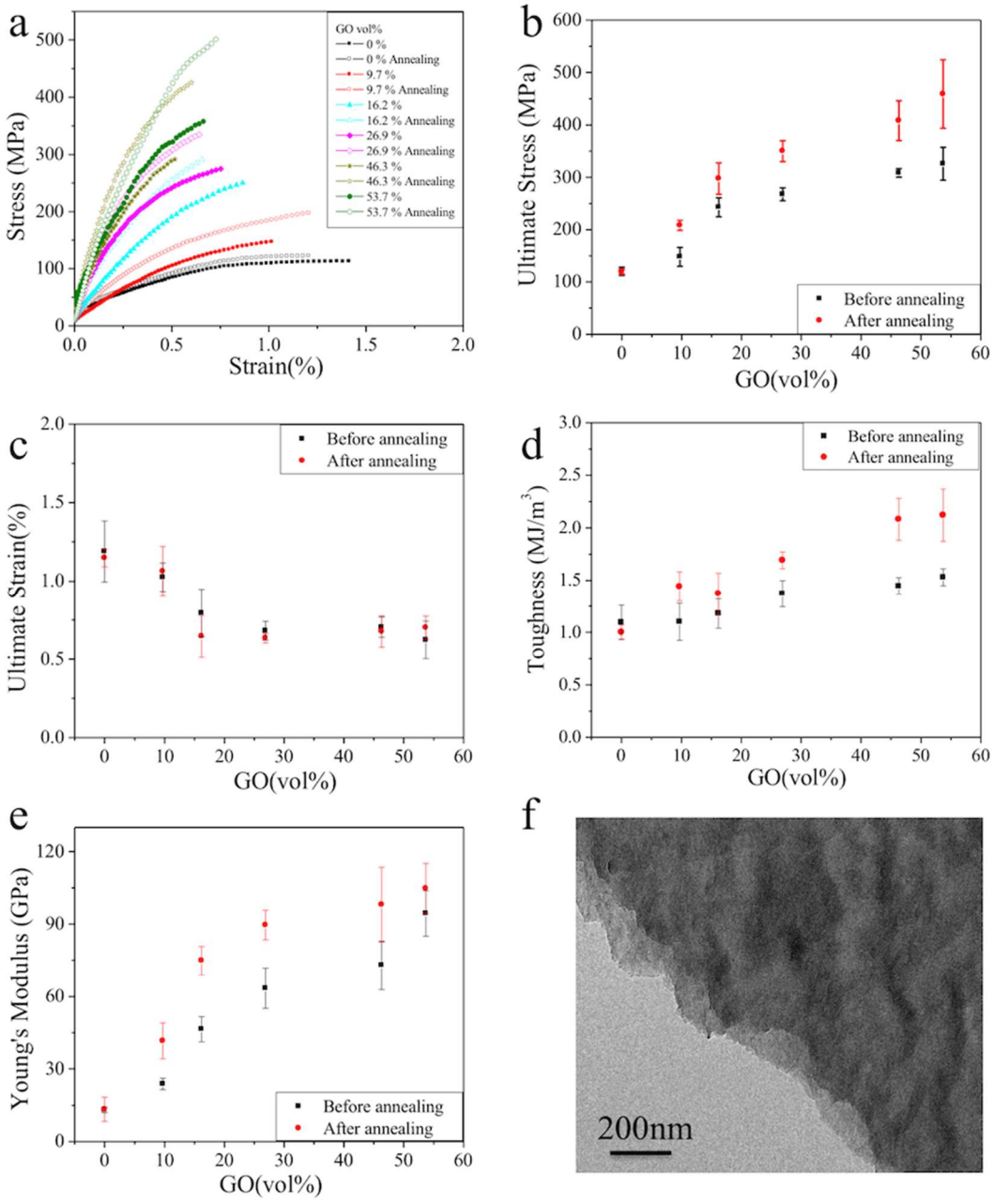

Figure 4.3. Mechanical properties of the nanomembranes: (a) Representative stress–strain plots from bulging tests for the samples before and after annealing (b–e) GO concentration dependence of ultimate stress (b), ultimate strain (c), toughness (d) and Young's modulus (e), (f) typical TEM image shows the edge of the fractured nanomembrane.

Next, there's little difference between ultimate behavior of before and after annealing, as both representative stress–strain curves present a linear elastic region followed by a plastic deformation region before fracture.[171] The representative edge of the membranes also shows obvious pull-out tracks (**Figure 4.3**f). Similarly with proteins in natural nacre, SF in the nanomembranes works as high performance adhesive, withstand tremendous stresses at the interface.[168,177] Generally, strong interactions between GO and SF components combined with high shear strength of silk layer cause significant improvement of mechanical performance.[166,187]

The important observation for this study is the fact that water vapor annealing resulted in concurrent and significant rise of ultimate stress, Young's modulus and toughness for the whole range of GO content with unchanged ultimate strain (**Figure 4.3**a-e). The ultimate stress increased between 23% to 41%; the Young's modulus increased between 11% to 75%, and the toughness increased between 16% to 45% (**Table 4-1**).

Table 4-1. Changes of the mechanical properties of different nanomembranes after annealing.

Sample-GO content	Ultimate stress change	Young's modulus change	Toughness change
SF control - 0	-1%	2%	-9%
GO/SF – 9.7	41%	75%	31%
GO/SF – 16.2	23%	61%	16%
GO/SF – 26.9	31%	41%	23%
GO/SF – 46.3	32%	34%	45%
GO/SF – 53.7	41%	11%	39%

Note: 9.7, 16.2, 26.9, 46.3, 53.7% represent the volume concentration of the GO in the GO/SF nanomembranes. Annealing condition: at 60 ^{o}C for 20 hours.

It is important to note that for control pure silk nanomembrane, the mechanical properties were not significantly affected by annealing. As known, in the hydrated environment, the

SF films show an increase in ultimate stress and elastic modulus with the decrease of the ultimate strain with water vapor annealing.[179] In contrast, in the dry state, the best results published reveal 43% increase in ultimate stress with 51% decrease in Young's modulus after annealing in water due to small content of β-sheets domains.[188] Therefore, special attention should be paid how the presence of the GO surface might affect the SF annealing behavior and resulting mechanical performance. In the next section, we will discuss how water vapor annealing affects the morphology, structure and interactions of GO/SF nanomembranes.

4.3.3 Annealing effect on GO and SF bonding interactions

FTIR spectroscopy is one of the well-established and powerful techniques for conformational analysis of polypeptides and proteins including SF materials (**Figure 4.1**). As known, the amide I (1600-1700 cm^{-1}) and amide II (1500-1600 cm^{-1}) bands commonly used for analysis of the secondary structure of silk materials are extremely sensitive to atmospheric water vapor, so it is difficult to analyze those two amide bands quantitatively unless water is completely excluded from the specimen and light path.[189] Moreover, another problem made it even harder for conventional conformational analysis in our case: a sharp peak at 1627 cm^{-1} corresponding to the vibration of the keto-enol equilibrium is shown in the FT-IR spectrum of GO, that is the same region of β-sheet absorption (at 1626 cm^{-1}) in amide I band.[190,191]

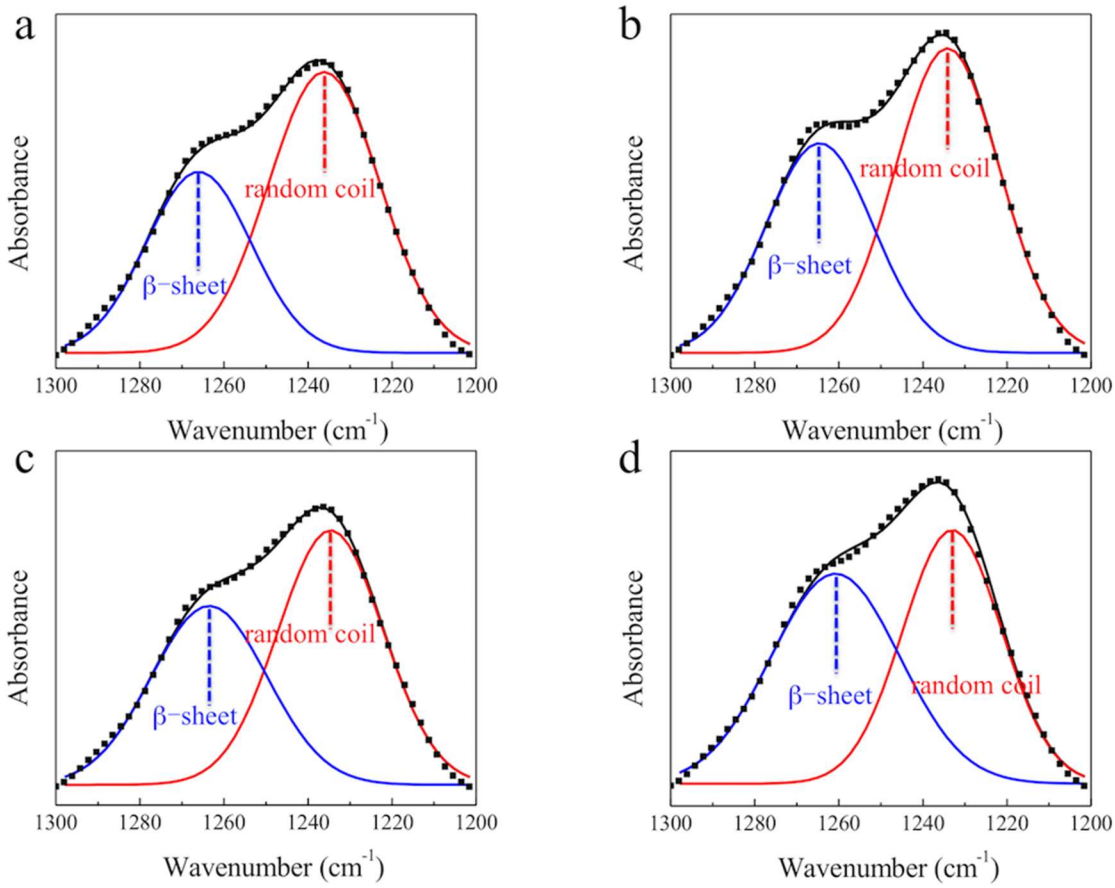

Figure 4.4. FTIR spectra and deconvolution of the corresponding amide III band of SF control membrane before (a) and after (b) annealing, GO/SF membrane under GO volume concentration of 46.3% before (c) and after (d) annealing (Note: circles, original spectrum; blue curve, deconvoluted β-sheet peak; red curve, deconvoluted random coil peak; black curve, simulated spectrum from summed peaks).

On the other hand, as seen in literature, the less-water sensitive amide III band (1200-1300 cm^{-1}) can be used alternatively to analyze quantitatively the secondary structure and composition of silk fibroin in place of traditional amide I band.[192,193] For *B. mori* silk fibroin, the absorption peaks in amide III band are assigned as follows: 1222 cm^{-1} to β-sheet, 1242 cm^{-1} to random coil and/or helical conformation. Also, GO film shows no strong absorption bends in the range of 1200-1300 cm^{-1} thus making analysis more reliable. Thus, in this study, we consider amide III bands to analyze β-sheet content of SF component through deconvolution of the spectrum. However, it should also be mentioned

that, GO component still shows some absorption with very slightly fluctuation in amide III region, which may influence the absolute value of β-sheet content to modest extent.

The analysis of these bands shows that first, as expected, β-sheet content of pure silk film significantly increased after water vapor annealing (**Table 4-2**). For SF control sample prepared by spin coating SF solution and methanol, the β-sheet content reaches 33.1 ± 0.3 %, which is naturally higher for SF/GO assembled with methanol treatment (28.8 ± 0.1 %). After further water vapor annealing, the β-sheet content increased to 36.4 ± 0.4 %, with a relative increase of 10% (**Table 4-2**).

Table 4-2. The β-sheet content in SF and GO/SF nanomembranes before and after annealing.

Sample	β-sheet content (%) /Before annealing	β-sheet content (%) /After annealing
SF control	33.1 ± 0.3	36.4 ± 0.4
GO/SF – 9.7	37.5 ± 0.3	43.5 ± 0.7
GO/SF – 26.9	38.1 ± 0.2	44.0 ± 0.8
GO/SF – 46.3	38.9 ± 0.6	45.2 ± 0.3

Note: 9.7, 26.9, 46.3% represent the volume concentration of the GO in the GO/SF nanomembranes. Annealing condition: at 60 ^{o}C for 20 hours.

Second, for all GO/SF nanomembranes, the β-sheet content of silk materials before annealing is already high, around 38 % because of methanol affect. After water vapor annealing, the β-sheet content reached even higher values, around 44 %, a relative increase of 16%. That is, not only the β-sheet content in our GO/SF nanomembranes is higher than that in pure SF control sample obtained without methanol treatment, but also the increase of β-sheet content during annealing is also much higher. With the β-sheet content of GO/SF nanomembranes not showing much difference under various GO contents, it is

reasonable to assume that the presence of the GO surface could promote higher content of β-sheet. In such a case, it is not only water vapor annealing could increase β-sheet content of SF, but the interfacial interactions of GO and SF becomes important in relative changes.

4.3.4 Annealing effect on SF backbone ordering of GO layers

The structures of GO, SF and GO/SF nanomembranes were further investigated by X-ray diffraction (XRD) in the low-angle scattering region (**Figure 4.5**). The XRD data for pure SF film (no GO component) and on the silicon wafer substrate show no diffraction peak in this region (**Figure 4.5**a). On the other hand, for purely GO film (no silk component) prepared by vacuum filtration, the (002) diffraction peak is centered at $2\theta=10.6^{o}$, corresponding to the interlayer distance (d-spacing) of 0.83 nm. This corresponds well with the value for laminated GO films (**Figure 4.5**a).

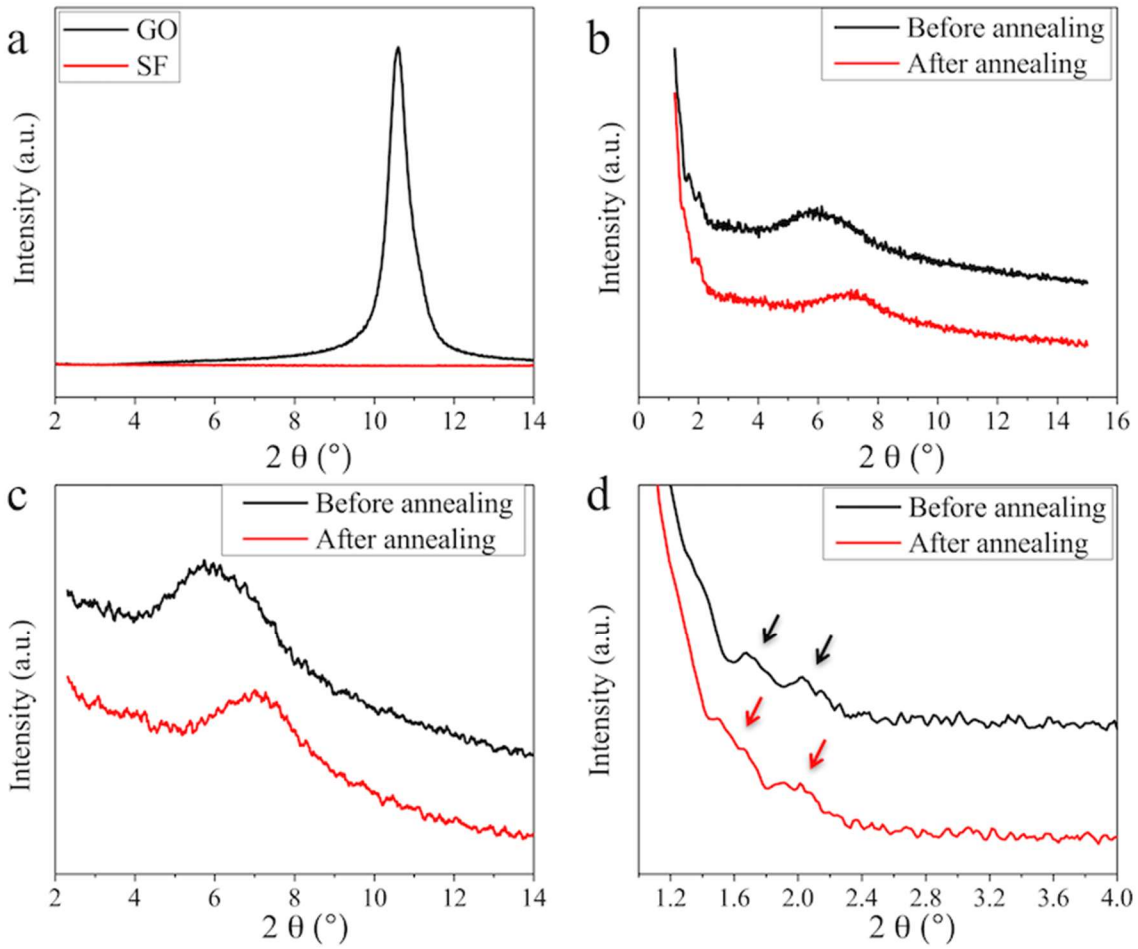

Figure 4.5. (a) XRD patterns of GO and SF, (b-d) XRD patterns of 80-bilayer GO/SF nanomembrane under GO volume concentration of 26.9% on silicon wafer and the zoomed in area.

To obtain higher signal to noise ratio, we prepared the thicker films with 80 bilayers under identical conditions with GO volume concentration of 26.9% (**Figure 4.5**b-c). For the GO/SF nanomembrane before annealing, the main peak becomes more diffused and is centered at 2θ=5.8°. Thus, the addition of silk layers between the GO layers resulted in dramatic d-spacing increase to 1.46 nm, which is almost doubled initial d-spacing for pure GO films.[7,186] After annealing, the XRD peak shifts to 2θ=7.0 °, corresponding to the slightly smaller d-spacing of 1.26 nm. The decrease of d-spacing indicates the denser

packing of the GO/SF nanomembrane after annealing that can be related to increasing content of β-sheets as suggested by FTIR analysis discussed above. Furthermore, the Scherrer equation was applied with a shape factor of 0.9 to the (002) reflection for evaluating the average thickness of the stacked monolayers.[194] These values are similar, 3.2 nm and 3.6 nm, for the GO/SF nanomembranes before and after annealing that correspond to the correlated packing of the 2-3 monolayers of GO sheets, a characteristic number for short-range local ordering.

Next, there're two relatively weak peaks at smaller scattering region: around 1.6-1.8° and 1.8-2.1° (**Figure 4.5**d). These weak peaks correspond to the d-spacing of around 5.2 nm and around 4.6 nm, correspondingly. Considering that the ellipsometry data shows the average thickness of GO-silk bilayer for these films is 5.2 nm, we can assign first peak to the total d-spacing of the bilayer packing with the second peak can be probably related to the regions with reduced thickness due to the incomplete coverage with GO sheets. Indeed, AFM image shows surface coverage after each GO deposition of about 69%, that indicates significant (30%) fraction of surface areas not covered by GO monolayers and corresponds well to our previous work (**Figure 4.1**a).[84]

4.3.5 Annealing effect on surface binding by SF on GO

To understand the assembly behavior of SF on GO during annealing, we prepared GO/SF/GO films with sandwiched structure (one layer of SF in the middle confined between monolayers of GO sheets) and compared their morphology with that observed on

a single layer of SF (**Figure 4.6**a,b, large ridges correspond to GO wrinkles). As observed, silk backbones in GO/SF/GO films before annealing exhibit uniform morphology of globular nanoclusters with approximately 1-3 nm in heights, usually observed for silk after adsorption (see sections in **Figure 4.6**).

As known, SF chains are constituted of alternating hydrophobic and hydrophilic blocks, which tend to aggregate into nanoscale clusters without preferential interactions in solution.[180,195] Generally, further assembly might result in the formation of bundles and nanofibrilles. With fast solvent evaporation during spin-coating, SF macromolecules attached on the substrate, kept their intrinsic morphology in solution and formed the dense SF layer. The surface morphology is comparable with those observed for a SF layer on silicon wafer before annealing (**Figure 4.7**a-c).

Annealing of single SF layer on a silicon surface at 60 ºC resulted in the formation of fibrillar network with individual aggregated fibrils of ca. 9 nm height (**Figure 4.7**d, e). However, annealing-related behavior of the GO/SF/GO counterpart is much different. The surface morphology of GO/SF/GO transformed to the much finer networked texture with GO wrinkles becoming more developed (**Figure 4.6**d, e). SF globular nanoclusters assembled into SF nanofibrils with a necklace-like morphology with a height of about 2 nm (**Figure 4.6**f), indicating much lower level of molecular aggregation compared with single layer SF on silicon wafer after annealing as described in the next section.

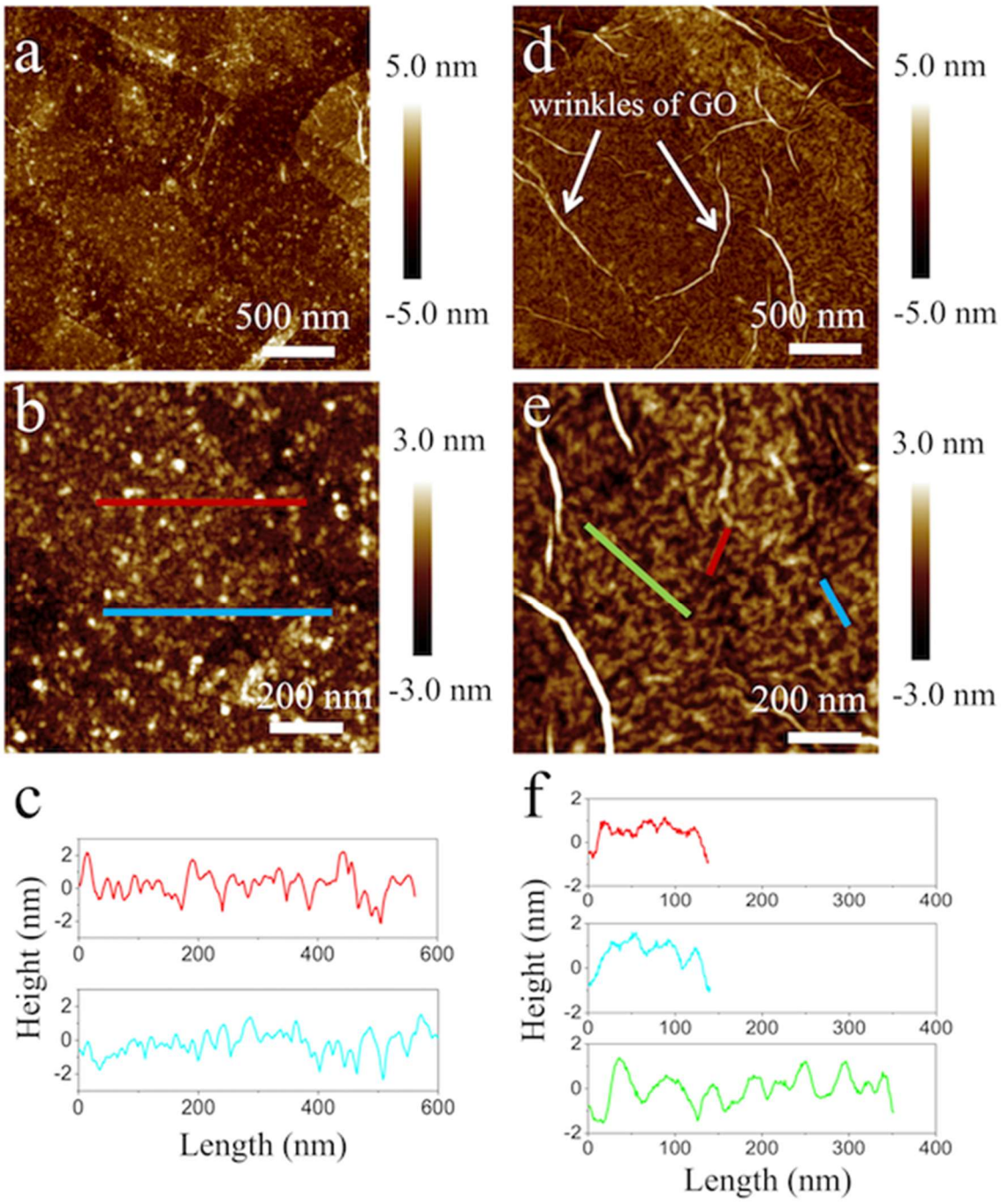

Figure 4.6. AFM surface morphology of the GO-SF-GO films before annealing (a, b) and after annealing (d, e) and their corresponding height profiles (c, f).

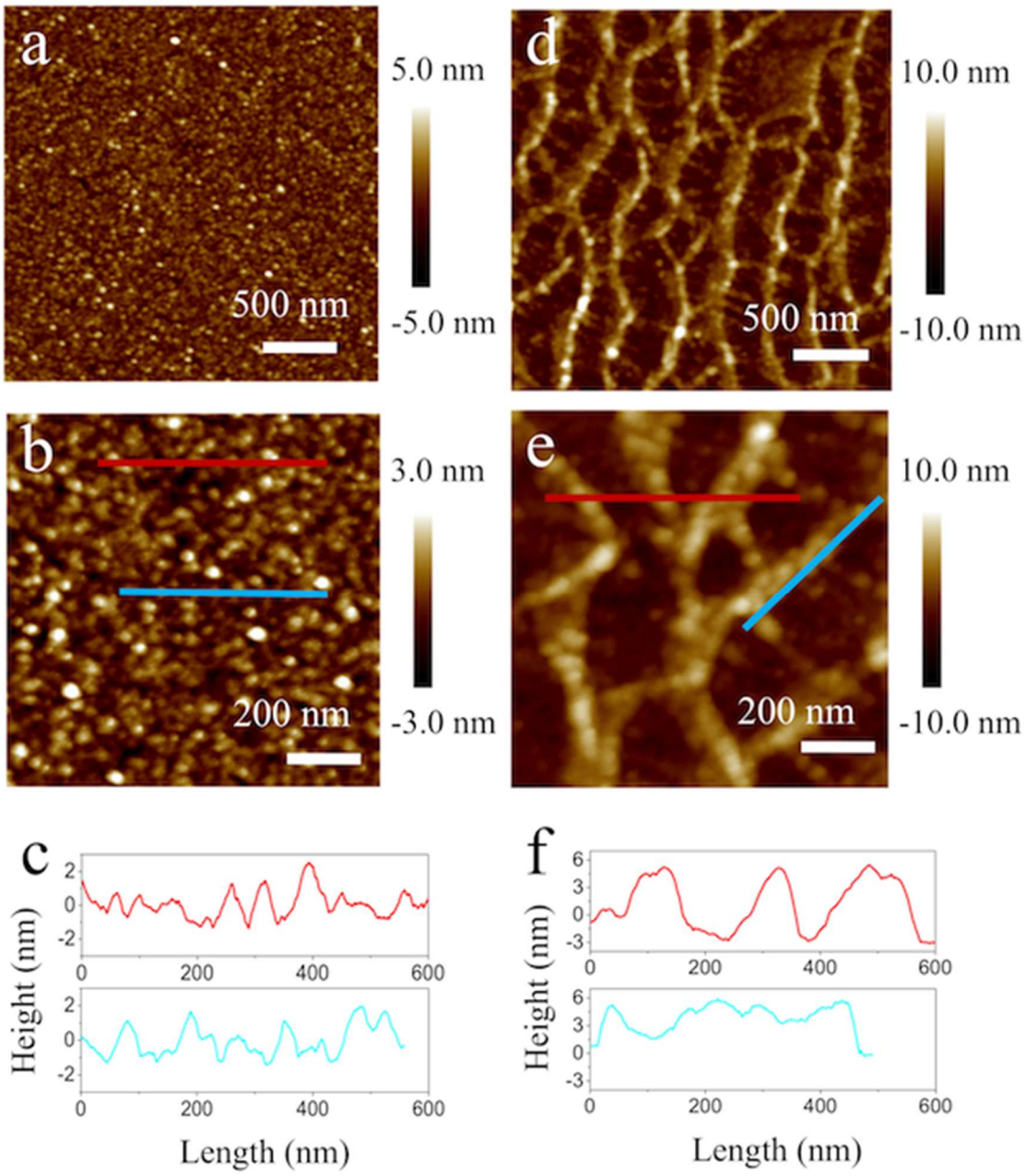

Figure 4.7. AFM surface morphology of SF layer on a silicon surface before annealing (a,b) and after annealing (d,e) and their corresponding height profiles (c, f).

4.4 Conclusion

Based on the all independent measurements discussed above, we suggest the mechanism of enhancement of the mechanical properties of GO/SF nanomembranes upon water vapor annealing (**Figure 4.8**).

The schematics of the structure of GO/SF nanomembrane before and after annealing is illustrated as **Figure 4.8**c (all parameters are GO volume concentration of 26.9%, see Supporting Information for detail). The average thickness increase after each GO and SF deposition is 1.4 nm and 3.8 nm, respectively (**Figure 4.8**, C1). The stacked GO layers (**Figure 4.8**, C2) represent 2-3 layers of GO with some SF molecular chains inserted according to the XRD results. Initially, the globular like SF nanoclusters between GO layers or on silicon wafer are both mainly constituted of disordered non-crystalline domains with a small percentage of β-sheet nanocrystal induced by the shearing as well as fast solvent evaporation after spin coating according to the FTIR results.[196]

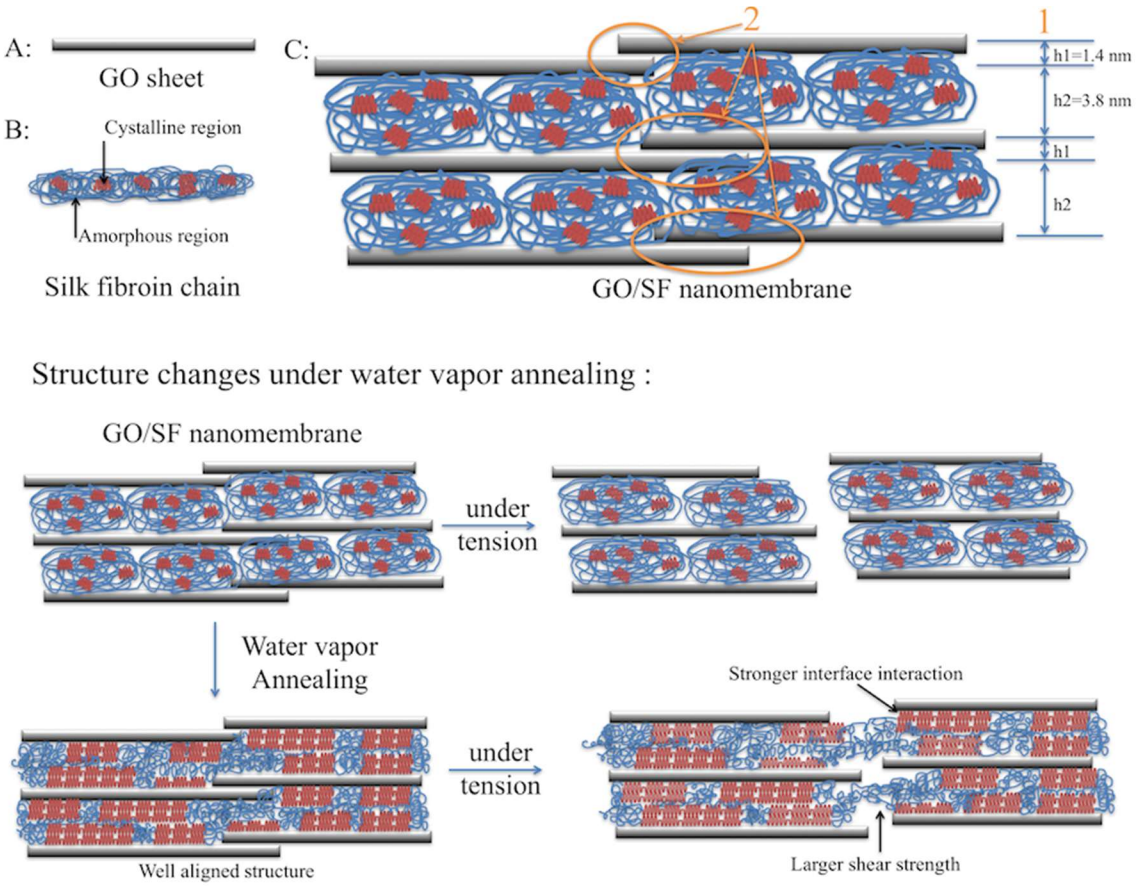

Figure 4.8. Structural changes of the GO/SF nanomembrane under water vapor annealing: A-C illustrates the simplified structure of GO sheet, SF chain and GO/SF nanomembrane (GO volume concentration of 26.9% as the example).

During the water vapor annealing process, water molecules gradually permeate into silk layer acting as a plasticizer and then increasing the mobility of SF chains.[178] Thus, the unstable SF mesosphase is firstly formed with bound water molecules, containing soluble amorphous regions as well as the hydrophobic β-sheet nanocrystal regions. As for single layer SF with annealing, the unstable SF mesosphase continue growing based on the existed β-sheet nanocrystal and transferred into larger 3-D β-sheet domains and connecting into the necklace-like fiber (as morphology shown in **Figure 4.7**d,e). Hence, for annealed SF nanofilm, larger but randomly distributed (along with no certain orientation) β-sheet

domains are formed. However, decreasing crystallite size and increasing degree of orientation of crystallites are proved to be more conducive to the strength enhancement of silk materials.[197,198] Thus, the mechanical prosperities don't show much difference for SF nanomembranes before and after annealing.

The unstable SF mesosphase transition between GO layers is more interesting. GO surfaces with significant fraction of hydrophobic area could provide strong interaction with hydrophobic GAGAGS motifs, which promotes silk backbones to further assemble on GO layers.[180,182] On the other hand, silk backbones are negatively charged in water with the zeta-potential of SF solution of -7.6 ± 0.5 mV. The localized charge densities of the hydrophilic, negatively charged oxidized areas of GO surfaces is higher and thus facilitate preferential assembling on the hydrophobic regions.[199] Confinement of SF chains between GO sheets should facilitate nucleation of disordered domains and the formation the β-sheets in nanoscale silk layers (thickness below 4 nm). In this way, not only SF can directly assemble into nanofibrils that strongly clinging to adjacent GO sheets increasing effective shear strength (Figure 9) , but also, SF molecular remains low level of molecular aggregation that ensures the uniform of the hierarchical structure.[199] Thus, well-ordered packing of GO layers and SF nanofibrils with more and aligned β-sheet domains is formed, leads to stronger interfacial interactions. Furthermore, the amorphous region of SF inter-molecule chain is connected different β-sheet domains after annealing, which formed continues "bridges" across all the SF layer and even adjacent SF layers.[17] Concurrent increase in modulus, toughness and strength of GO/SF nanomembranes are achieved by water vapor annealing.

In conclusion, stronger and robust nacre-mimic GO/SF nanomembranes can be assembled by modifying and enhancing the interfacial interactions between laminated GO "bricks" and SF "mortar". Water vapor annealing at modest elevated temperature is demonstrated to be an efficient way to dramatically improve the mechanical properties of nacre-mimic materials. For GO/SF nanocomposite membranes, water vapor annealing produced a simultaneous increase in strength (by up to 41%), Young's modulus (up to 75%) and toughness (up to 45%) via the relaxation of the confined silk backbones. By investigating the reinforcement mechanism of water vapor annealing, we found that water vapor annealing increases silk backbone recrystallization induced by hydrophobic surface regions of GO sheets with aligned β-sheets strongly clinging the GO sheets. Larger shear strength of confined and recrystallized silk layers leads to the concurrent improvement in mechanical properties. The work presented here not only gives the better understanding of SF and GO interface interactions, but also provides insight to improving the mechanical properties for the nacre-mimic laminated material by focusing on the delicate interaction of "bricks" and "mortar" and then further modifying the interfacial morphology by additional gentle annealing.

CHAPTER 5. Screen Printing-Guided Reduction

5.1 Introduction

Novel nacre-mimic bionanocomposites, such as graphene-based laminates, are pushing the boundaries of strength and toughness as flexible engineering materials. Translating these material advances to functional flexible electronics requires methods for generating print-scalable microcircuits (conductive elements surrounded by dielectric elements) into these strong, tough, lightweight bionanocomposites. Here, we present a new paradigm for printing flexible electronics by employing facile, eco-friendly seriography to confine the reduction of graphene oxide biopapers reinforced by silk interlayers to be strong and chemically-resilient. Well-defined, micro-patterned regions on the biopaper are chemically reduced, generating a 10^6 increase in conductivity (up to 10^4 S/m) in order to facilitate sensing electronic functionalities. Flexible, robust graphene-silk circuits in diverse, prospective applications as resistive moisture sensors and capacitive proximity sensors are showcased here. Unlike electronics generated from the printing conductive inks *on* substrates, seriography-guided reduction does not create mechanically weak interfaces between dissimilar materials, and do not require the judicious formulation of conductive (i.e. graphene- or Ag nanoparticle-loaded) inks. We demonstrate the unimpaired functionality of printed-in graphene-silk microcircuits after thousands of punitive folding cycles, and chemical attack by harsh solvents, hazardous conditions which usually ruin existing materials designs. This novel approach provides a low-cost, portable solution for printing micron-scale conductive features uniformly across large areas (>hundreds of cm^2) in layered composites for emerging applications including wearable

health monitors, functional electronic skin, as well as large-scale rollable antennas and conformable displays.

Next-generation enhancements in human awareness-of and command-over personal surroundings follows the development of compliant, mechanically-robust, chemically-resilient 'information interfaces' that integrate seamlessly onto moving surfaces, such as clothing or the human body.[200] One class of materials, flexible graphene-based composites, has been ever-expanding the envelope of the materials universe toward record-breaking strength and toughness figures.[4–8,18] However, these recent developments have largely been limited to engineering composites for passive, structural applications, due to challenges in manufacturing well-defined electronic architectures into this new class of ultra-robust graphene-based materials. Here, we report the first print-scalable transformation of graphene composite papers to flexible, mechanically-robust microcircuit elements by a novel method of patterned graphene reduction as confined by seriography, or screen printing. We showcase the versatility, volume and resolution of this seriography-guided reduction by printing foldable, flexible device components in nacre-inspired graphene-silk layered composites with electrically-based functionalities for the detection of environmental signals (resistive humidity sensor), and capture of fine-motor human-inputs (capacitive proximity sensor).

Whereas traditional wafer-based devices are heavy, prone to breaking, and confined to their as-manufactured form-factor—flexible devices overcome these orthodoxies by enabling devices with diverse applications such as displays, energy generation/storage systems, and man-machine interfaces to operate under mobile and wearable environments.[201,202] For

instance, in the rapidly evolving field of bio-interfaced (or skin-mounted) electronics, device flexibility opens routes toward the seamless and adaptive detection of fine-motor gestures, body health indicators, and environmental threats related to chemical or biological warfare. Integrated human-environment and human-device interfaces will open the door to the ubiquitous monitoring, communication and control by individuals of their natural and machine surroundings in integrated smart environments.[203,204]

Common strategies for introducing flexibility into electronics include fabricating devices to be ultra-thin to minimize thickness-dependent strains,[205–209] and manipulating device geometry (i.e. *via* kirigami cuts or buckling) to redistribute points of high strain-concentration.[43,210–212] Included in the first strategy are additive printing techniques that, while valuable as a fabrication route, require the application and subsequent curing of a layer of a judiciously formulated solution comprised of conductive materials (i.e. silver nanoparticles, graphene-derivatives), and cannot allow for the clean removal of residual ink binders and fillers.[213–216] Improper optimization of ink properties or continuous printing across large surfaces may result in clogged solutions or unstable drop injection.[217] Moreover, both the minimizing thickness and kirigami cut approaches increase compliance come at the precipitous cost of decreasing mechanical strength. Resultant conductive structures cannot resist material rupture for non-stationary applications in the absence of external support. Backing mechanically weak electronic structures onto robust yet flexible substrates introduce additional interfaces between dissimilar materials where delamination could occur under flexion. These conventional methods of fabricating and backing flexible electronics involve some combination of complex deposition and lithographic techniques that have a high barrier to practical realization due to tool costs and requisite user-skill. To

these ends, there is a need for the facile, rapid and reliable generation of large-area flexible electronics in inherently strong, tough and flexible materials.

In this work, we report a novel seriography-based approach for generating large-area (up to hundreds of cm^2 in this work) micron-scale conductive features (microcircuits) in flexible, strong and tough graphene oxide (GO)-silk fibroin (SF) biocomposite films capable of withstanding chemical attack and large bending deformations. The superior mechanical properties of thin (several microns across) GO-SF bionanocomposite films (tensile strength 327 MPa, toughness 2.5 MJ/m^3) can be attributed to the strong interfacial interactions between the constituent GO flexible sheets mediated by a biopolymer glue (added 2% silk fibroin by weight).[218,219] Furthermore, GO-SF composites exhibit a strong resistance to chemical attack and do not undergo water plasticization, properties that carry over into the fabricated devices.

While the printing of graphene-based materials—notably through inkjet nozzles,[220–225] stencils,[226,227] and rotogravure[228]—has always generated extensive research interest, these previous methods require distributing graphene flakes uniformly into solvent/stabilizer mixtures that have been judiciously formulated for their viscoelastic shear-thinning behavior and favorable graphene solubility. The carbon nanomaterial loading in these inks is typically low due to residual stabilizers that cannot be removed during firing and act as dielectrics that detriment conductivity in printed microcircuits. Furthermore, the applicability of these previous printing techniques to generating devices in mobile applications requires not only the ability to print features onto a robust flexible substrate, but also depends upon the mechanical and chemical properties of the dried inks. Either a

mismatch in modulus/compliance/expansion, or low interfacial adhesion between the ink and substrate could lead to delamination or rupture of conductive features during flexion, altering the electronic properties of the printed features. In these regards, the screen printing reduction approach presented here represents the first report of printed-in conductive graphene-based features into inherently strong, tough, and flexible biopapers, whereby the patterned circuits do not rupture or delaminate under repeated cycles of folding, and survive chemical attack under diverse solvent conditions.

The conversion of insulating GO to highly-conductive rGO often requires high temperature annealing, or harsh chemical treatments, and cannot generate patterned rGO features.[229–234] Previously reported methods for generating patterned rGO features are often prohibitively cumbersome for large-volume production due to their serial nature, or their requisite use of lasers and ultrahigh vacuum tools.[235–239] On the contrary, screen printing is a cost-effective, print-scalable technique capable of being incorporated into semi-continuous roll-to-roll (R2R) processes, and is actively used in diverse industrial applications ranging from graphic impressions on textiles, to metal contacts for photovoltaics.[240,140,241,242] Our approach of screen printing a reductant ink on to GO-based films allows for the simultaneous application of reductant and patterning of conductive features. Unique among methods for reducing GO, this screen printing-based approach is low-cost, print-scalable, and capable of generating microscale flexible conductive features across large-areas. Here, we show the successful generation of features with a critical dimension of 70 μm, and features across an area of 400 cm^2. As a proof of concept of the ease and reliability of screen printing of microcircuits, we fabricate position and humidity

sensing flexible films and show their exceptional sensitivity combined with chemical and mechanical stability under harsh conditions that easily destroy traditional materials.

5.2 Methods

Assembly of GO-SF nanocomposite film. Aqueous suspensions of 50 mg/ml regenerated silk fibroin (SF) were prepared from the cocoon of the *Bombyx mori* by degumming, dissolving, purification, and dialysis based on a conventional procedure described by Kaplan *et al*.[243] Aqueous solutions of 2 mg/ml graphene oxide (GO) were prepared from natural graphite powder (325 mesh, 99.999% purity, Alfa Aesar) using a modification of the method proposed by Hummers.[244] The pH of the GO solution was adjusted to 10 by titration with 1M NaOH. To the pH 10 GO dispersion was added in the silk fibroin suspension at a 98:2 GO:SF weight ratio. GO-SF dispersions were mixed by stirring and remained stable for over one week. The GO-SF dispersion was dried by vacuum filtration on a 0.2 μm acrylic copolymer membrane filter (Versapor 200, Pall) to yield GO-SF films with areal dimensions fixed by the filter and thickness defined by GO-SF volume. GO-SF dispersion was cast-dried on a fluorinated ethylene polymer (Teflon FEP, DuPont) sheet to yield large-area GO-SF sheet easily exceeding hundreds of cm^2. The GO-SF films were removed from their membrane filter and FEP backings to yield large-area, freestanding GO-SF films.

Micropatterned reduction of GO-SF films by screen printing. High resolution localized reduction of GO-based films was produced by printing an aluminum metallization paste (EFX-37, Monocrystal) using a semi-automatic screen printer (MPM SPM-V, Speedline Technologies) with a 45° passing blade, 1 mm snap-off distance, blade speed of 5 cm/s, masked by a purchased wire cloth screen with the designed pattern (500TW front-contacting, Haver&Boecker). The hobbyist setup for low-cost screen printing of GO-SF employed a polyester screen (16"x20" 110 monofilament, Speedball) with a laser-cut (Q-switched Nd:Ylf 1047 nm, Resonetics) paper stencil glued to the side of screen in contact with the substrate. The metallization paste was applied through the screen using a handheld squeegee was operated at ~45°, with a ~2 mm snap-off distance, and with a blade speed of ~25 cm/s. Residual solvent in the Al-patterned GO-SF was removed by treatment in vacuum oven (60 °C, 10 minutes). The Al-patterned GO-SF was then dampened with ultrapure water (18.0 MΩ-cm), and sandwiched between PTFE blocks for overnight. Subsequent rinsing under a stream of ultrapure water, then isopropanol, removed the patterned Al to yield conductive rGO-SF features in the negative image of the stencil.

Characterization of printed rGO-SF microcircuits. Screen printed reduction features in GO-SF films were imaged using optical microscopy (Leica DM 4000) and low-voltage cold field emission SEM (Hitachi SU8230). Chemical verification of reduction was undertaken using Raman spectroscopy mapping (Alpha-WITec 300R, 532nm laser) and X-ray photoelectron spectroscopy (Thermo Scientific K-alpha). Conductivity measurements were obtained using four-point probe measurements. Bending and folding tolerance was

tested by placing a screen printed GO-SF strip (50 x 5 x 0.1 mm) along inside of a folding hinge for 2000 cycles, ~1 cycle/s at 90° for bending tests and 180° for folding tests.

Characterization of position and humidity sensors. Time-resolved potential difference between capacitive plates were recorded using a potentiostat (VersaSTAT3, Princeton Applied Research) using a two-electrode open-circuit configuration. Conductivity measurements were collected using a Keithley 6220 source attached through a 2182 nanovoltmeter. Humidity response tests were carried out under ambient laboratory conditions (25 °C, 20% RH). The 97% RH chamber was maintained by a saturated solution of K_2SO_4 (Sigma-Aldrich, >99%).

5.3 Results and Discussion

5.3.1 Micro-Patterned Reduction by Screen Printing in Biopapers

Assembly of graphene-silk biocomposite papers. In this approach, first we assemble the GO-SF biocomposite substrates from a homogenous mixture of graphene oxide flakes and silk fibroin *via* vacuum-assisted filtration or evaporation-assisted casting.[144] Vacuum-assisted assembly generates GO-SF "paper" with lateral dimensions controlled by the diameter of the filter, while cast drying the GO-SF mixture onto PTFE blocks generates continuous films with areas easily exceeding 100 cm2 that can be lifted from the substrate using pressure-sensitive tape. The silk fibroin (typically 2% by wt.) in the composite film

act as a multifunctional binder to the GO matrix, resulting in a three-fold increase in ultimate strength (150 MPa), and ten-fold increase in toughness (2.6 MJm-3) of the GO biopaper when compared to pristine (no silk binder) GO paper.[219,144] Furthermore, unlike pristine GO paper, the GO-SF composite films do not decompose under common solvents such as water and isopropanol. This crucial property allows the reductant ink to be rinsed off after the reduction process without compromising the patterned GO-SF film's mechanical integrity.

Screen printing microcircuits across large areas in biopapers. In this seriography-guided reduction (**Figure 5.1**), a stencil masks the mesh -openings on a screen from the ink (a thixotropic aluminum paste capable of reducing the GO component) in the stencil's positive image, preserving the underlying substrate. During the print step, ink is pressed by a fill blade through uncovered mesh openings to bring the aluminum paste into contact with the underlying biopaper. GO in contact with an anodic metal undergoes reduction due to a redox reaction in a mechanism suggested in another work.[219]

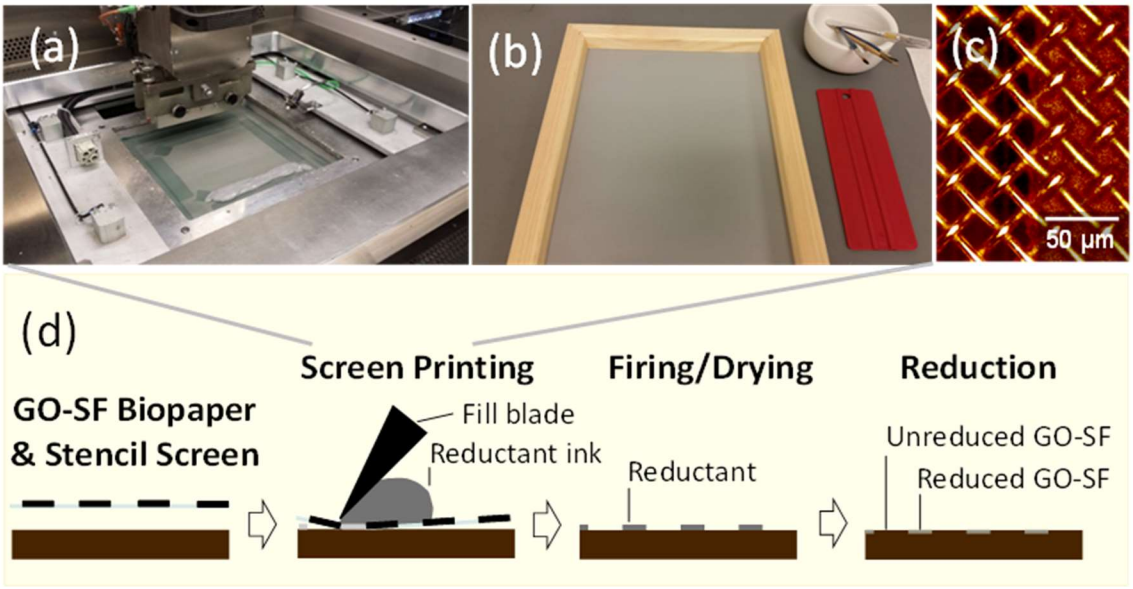

Figure 5.1. a) Automated screen printer for generating high resolution micro-scale conductive features at large volumes (~200 cm2/s). b) Hobbyist screen printing setup. c) Stencil screen with open mesh on left showing 25 µm mesh openings, and masked mesh on right by photoemulsifier. d) Screen printing process for the micro-patterned reduction of graphene-silk biopapers.

Using low-cost, portable craft supplies such as a hobbyist screen printing kit and stencils cut in office paper, we can pattern the reductant ink in ambient conditions to produce complex geometry conductive micro-features in the GO-SF film such as a "bulls-eye" pattern comprising of concentric circles (Figure 5.2a), and 100-µm gaps of insulating unreduced GO-SF between strips of conductive reduced GO-SF (Figure 5.2b). We also demonstrate the ability to pattern with high fidelity across large areas by fabricating repeated arrays of a motif on 400 cm^2 GO-SF drop-cast sheets (Figure 5.2c,d). Using an automated screen printer setup with a high-resolution steel wire cloth screen, we demonstrate the ability to pattern higher precision 70-µm conductive fingers and busbars in strong and tough GO-SF at the rate of ~300 cm^2/s (2400 cm^2/pass, ~7.5 passes/minute). Crucial to the robustness and reliability of this technique is the screen, which not only enables patterns to be generated with non-continuous feature elements (such as concentric

circles in the “bull’s eye” pattern); and acts as a uniform spacer between the blade and the substrate, providing spatial control over ink distribution (Figure 5.2).

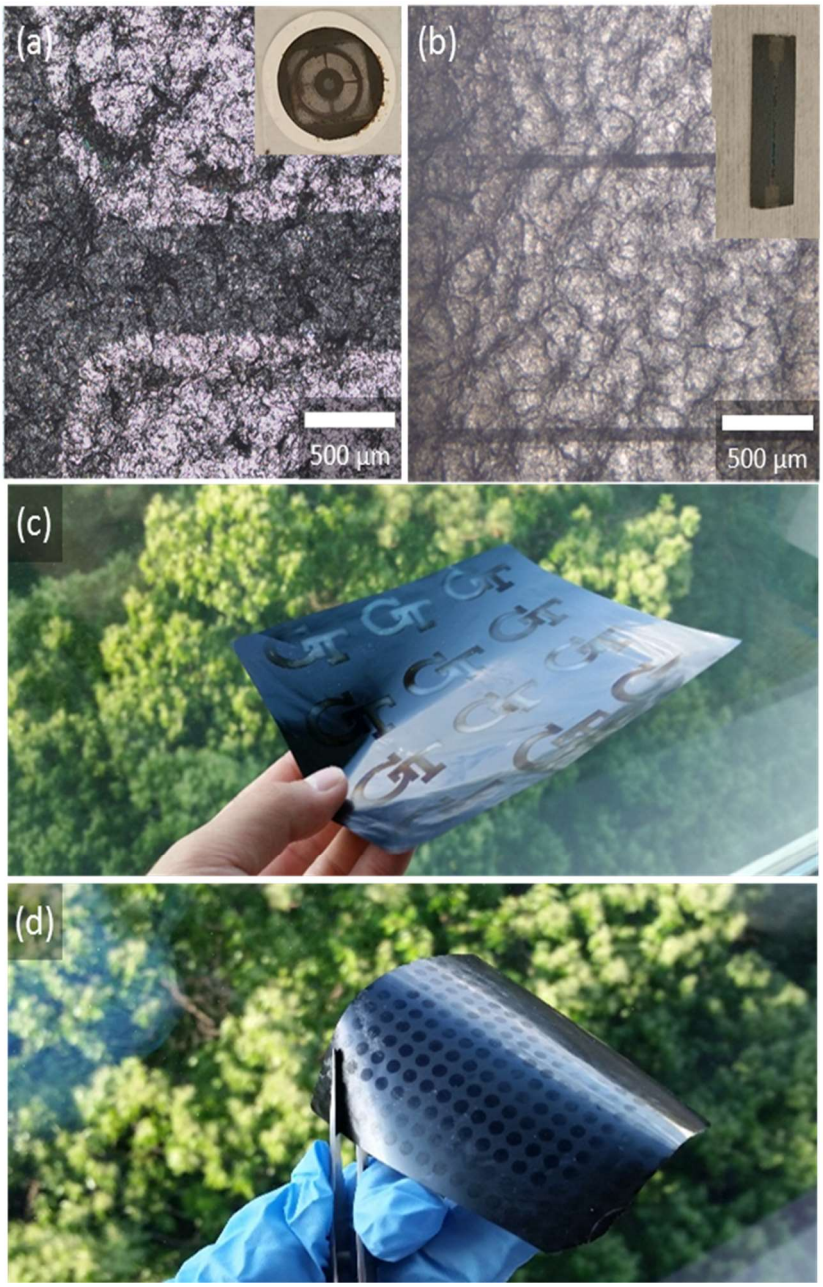

Figure 5.2. Large-scale printing of micro-scale features by seriography-guided reduction. Optical micrographs of microscale patterns showing a) the corner of a bullseye target pattern, and b) 1.5 mm strips with 100 µm unreduced GO-SF gaps. GO-SF sheets printed with conductive d) array of ‘Georgia Tech’ logos and e) array of circles, preserving pattern fidelity across large areas (>20cm x 20cm).

5.3.2 Critical properties of Screen Printed GO-SF biopapers

Efficient chemical conversion by reductant. The geometry-localized chemical conversion of the GO component to conductive rGO by the reductant paste was independently verified using X-ray photoelectron spectroscopy (XPS) and Raman spectroscopy mapping. Figure 5.3a shows an optical micrograph of well-defined Al busbars and 70-μm fingers screen printed onto GO-SF. Raman mapping of the sample after reduction (Figure 5.3b,d) revealed that the regions in contact with the reductant paste exhibited a marked increase in the I_D/I_G ratio from 0.92 to 1.19, where I_D corresponds to the areal intensity of the GO D-band peak centered at 1350 cm^{-1} and I_G corresponds to that of the G-band peak centered at 1600 cm^{-1}.[245,246]

Examination of the Raman point spectra revealed that GO-SF treatment by the reductant paste also yields a narrowing of the D-band full width half max. Both the increase in the I_D/I_G ratio and narrowing of the D-band are observed in GO-SF reduced by hydrazine, are in alignment with observations from other GO reduction methods, and suggests the introduction of defects to the sp^2 structure during the reduction process.[245,247] Figure 5.3c compares XPS spectra obtained from regions in contact with (inside busbar), and masked from (between fingers) the Al reductant.

From peak fitting the high-resolution scans of the carbon 1s region, we find that regions treated with the reductant paste exhibited a decrease in the carbon composition participating in bonding with oxygenated moieties (includes C-OH, COOH etc.), and an increase in non-oxygenated carbon (includes C-C/C=C) composition from 49.8 to 60.2 At%. Peak analysis of the survey spectra found that treatment by Al paste produced a

significant increase in C/O atom ratio from 2.4 to 3.6, supporting the fact that treatment of GO by the aluminum paste leads to the reduction of GO, increasing the carbon content of reductant-treated film by removal of oxygenated functional groups.

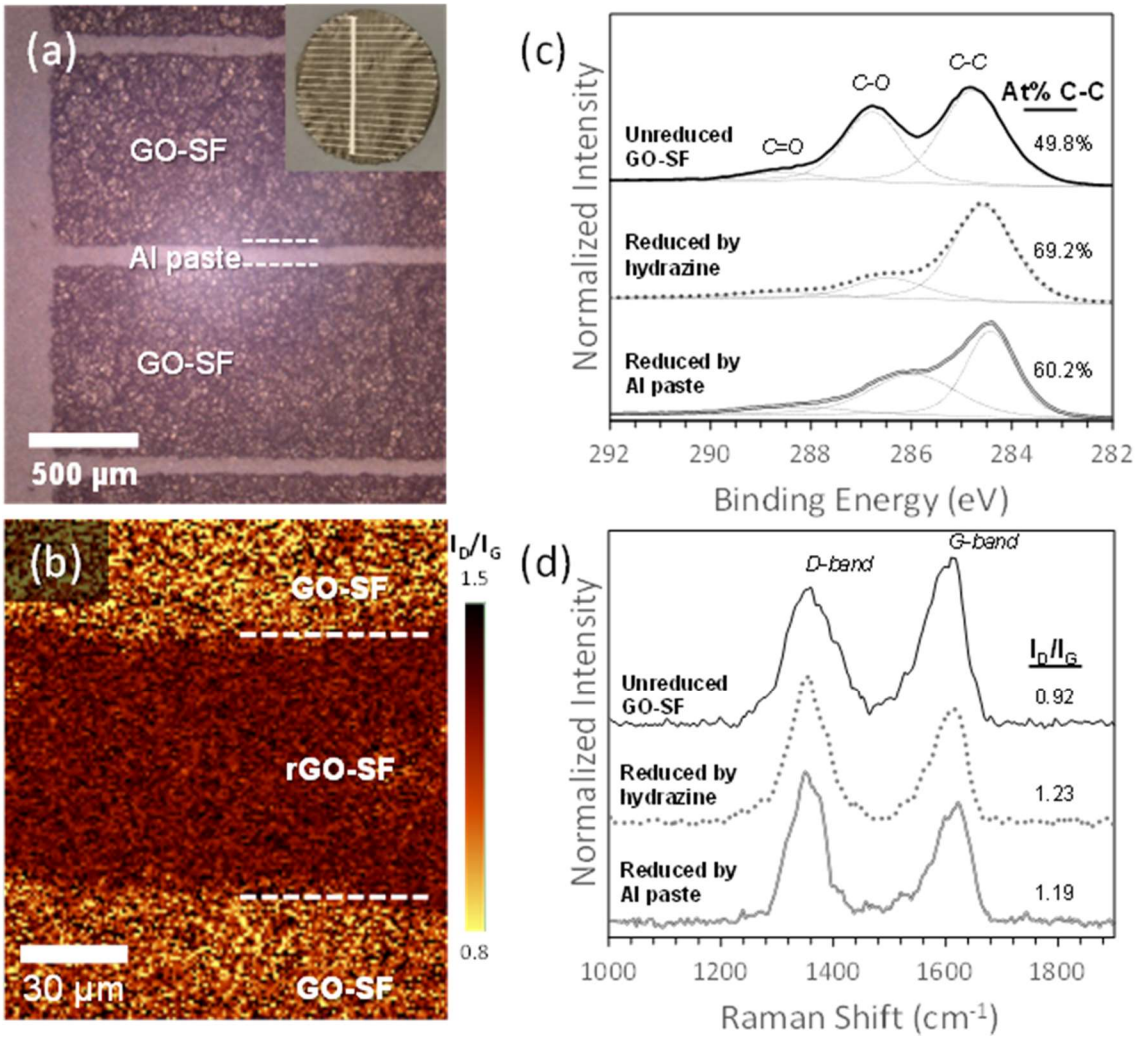

Figure 5.3. Spectroscopic evidence for localized GO conversion. a) Before reduction, optical micrograph of Al busbars and 70-µm fingers screen printed onto a GO-SF biocomposite film. b) After reduction, 532-nm laser Raman map of 70-µm wide rGO-SF fingers. The color scale indicates the ID/IG ratio for the spectra collected at each pixel. c) Carbon 1s XPS and d) Raman point spectra comparison of unreduced GO-SF, GO-SF reduced by hydrazine vapor, and GO-SF reduced by the Al paste.

The reduction across large-areas was observed to be highly uniform by visual inspection of large-area reduced GO biopapers, and by Raman mapping across a 150 × 150 μm^2 region (Figure 5.3b) showing Raman D/G peak ratio shift well-confined desired patterned features. The uniformity of reduction by this technique was additionally verified through comparison of carbon 1s XPS spectra collected from different locations on a large-area reduced GO-SF sheet.

The conversion of GO to rGO by the screen printed aluminum paste was also accompanied by a change in visual appearance from dull and black in the untreated GO-SF film, to shiny and grey in the reduced areas (Figure 5.2b-e). Four point probe measurements show that the features transformed by the reductant paste exhibited over a six order of magnitude increase in in-plane electrical conductivity from 8.7×10^{-3} S/m to 1.1×10^{4} S/m (Figure 4a)—a dramatic change from an insulator with comparable conductivity to damp wood, to a semi-metal with conductivity exceeding that of doped conductive polymers such as PEDOT:PSS.[248,249] High resolution XPS spectra in the Al 2p signal region revealed the efficient removal of residual aluminum in the reduced GO-SF composite, confirming that the changes in optical and electronic properties are not a result of residual metal from the printed features.

Resilience under folding stresses and chemical attack. Due to the strong, tough, yet flexible nature of the GO-SF substrate, this increased conductivity in printed features is retained even after applying large bending stresses. Figure 5.4b shows the ratio of initial to final conductance after bending of a reduced GO-SF wire fabricated along the length of a GO-SF strip. The inset photographs show a top-down view of the GO-SF strip in the

bend test apparatus. We observed that subjecting the patterned GO-SF strip to 2000 bending-unbending cycles from 0° to 90° (corresponding a bend radius of ~3 mm) led to an average 2% decrease in conductance, while 2000 folding-unfolding cycles from 0° to 180° (corresponding a bend radius of ~0.5 mm) led to an average 5% decrease in conductance (Figure 5.4b). This small change in relative conductance could be attributed to rearrangement of constituent rGO flakes in the film, especially expanding along pre-existing defects. These minor changes in relative conductivity, within one standard deviation in replicates, indicate the high resilience of GO-SF films under large stresses and deformation.

The retention of conductivity after bending and folding cycles in our reduced GO-SF circuits is comparable or superior to previously reported flexible conductive materials such as conjugated polymer composites,[250] Ag nanoparticle-based inks,[251] and graphene-based inks.[252] These tests suggest that gluing GO sheets with a biopolymer binder (such as silk) is an efficient path toward protecting the integrity of flexible electronics against dissolution and large bending deformations—common conditions faced by devices interfaced on human/biological surfaces.

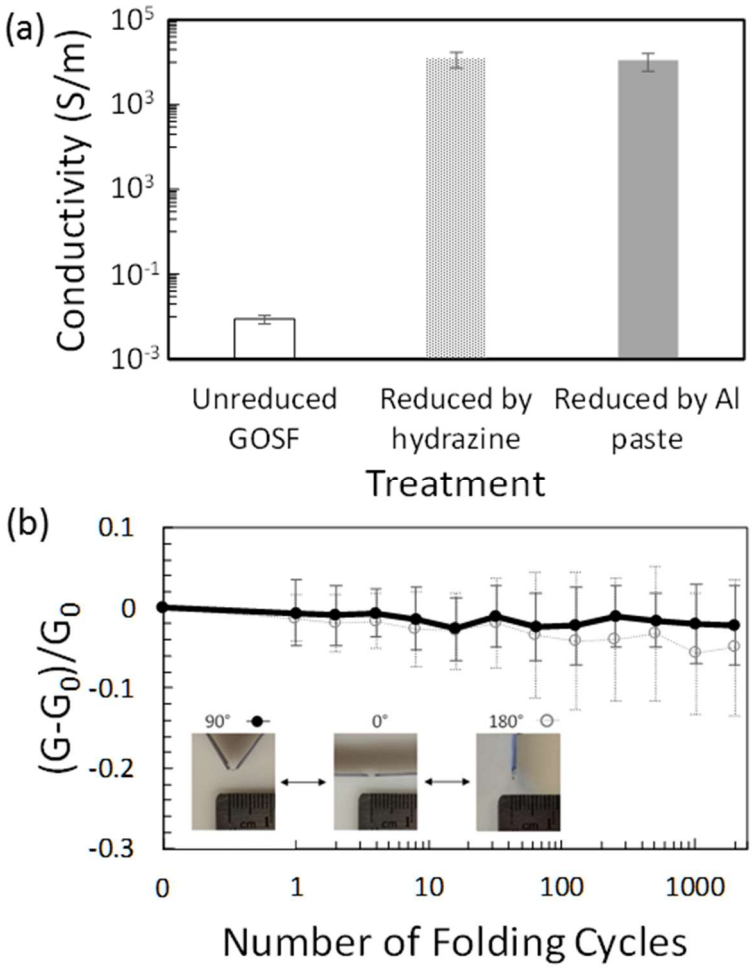

Figure 5.4. Conductivity of GO-SF treated by reductant. a) Graph comparing conductivity between GO-SF that is unreduced, reduced by hydrazine vapor, and reduced by screen printed Al paste. Error bar represents 5x standard deviation. b) Ratio of final to initial conductance in screen printed conductive rGO-SF strips across 2000 bending cycles at 90° ($r_{bend} \approx 3\ mm$) and at 180° ($r_{bend} \approx 0.5\ mm$).

Creases and wrinkles could be observed in samples after the bending tests, but these defects do not propagate through the thickness of the film to form tears or rupture within the testing conditions here. Optical microscopy of patterned GO-SF films after folding cycles show that direction of crease propagation in films is independent of the direction of patterned lines. Scanning electron microscopy of sectioned GO-SF films before and after folding reveal that the layered architecture of the biopaper is able to accommodate folding stresses cycles. Visual inspection of the optical micrographs support that the geometry of

conductive patterns generated on film likely has low stress-concentration effects that would weaken the mechanical integrity of the GO-SF. In addition to displaying high stability under folding stresses, the patterned GO-SF films exhibited high stability under agitation in common solvents, and under acidic and basic conditions. In contrast, pristine GO without the SF binder (such as traditional "GO paper") are not stable under agitation in water, and susceptible to delamination and visible redissolution.

5.3.3 Foldable, flexible environmental sensors

Capacitive proximity sensing. To demonstrate the versatility, ease-of-use and potential for rapid-prototyping of the screen printing reduction technique, we applied this technique to generate graphene-based circuitry in flexible electronics for proximity and humidity sensing applications. Figure 5.4a shows the schematic of a co-planar capacitive displacement sensor consisting of conductive rGO-SF (gray in scheme) parallel plates and wires separated by the insulating GO-SF (brown) film. The potential difference between the two conductive plates are recorded by a potentiostat using a two electrode open-circuit setup. Moving an external dielectric object (yellow ball) closer to midpoint of the device cuts into the electric field built up along the plates, polarizing the charges to generate a potential response that was measured to be inversely proportional to the distance between the external object and sensor (Figure 5.4b,c). Typical GO-SF sensors fabricated with 50 mm × 5 mm coplanar conductive plates were found to have a detection range of ~30 cm for a waving gesture by a human hand.

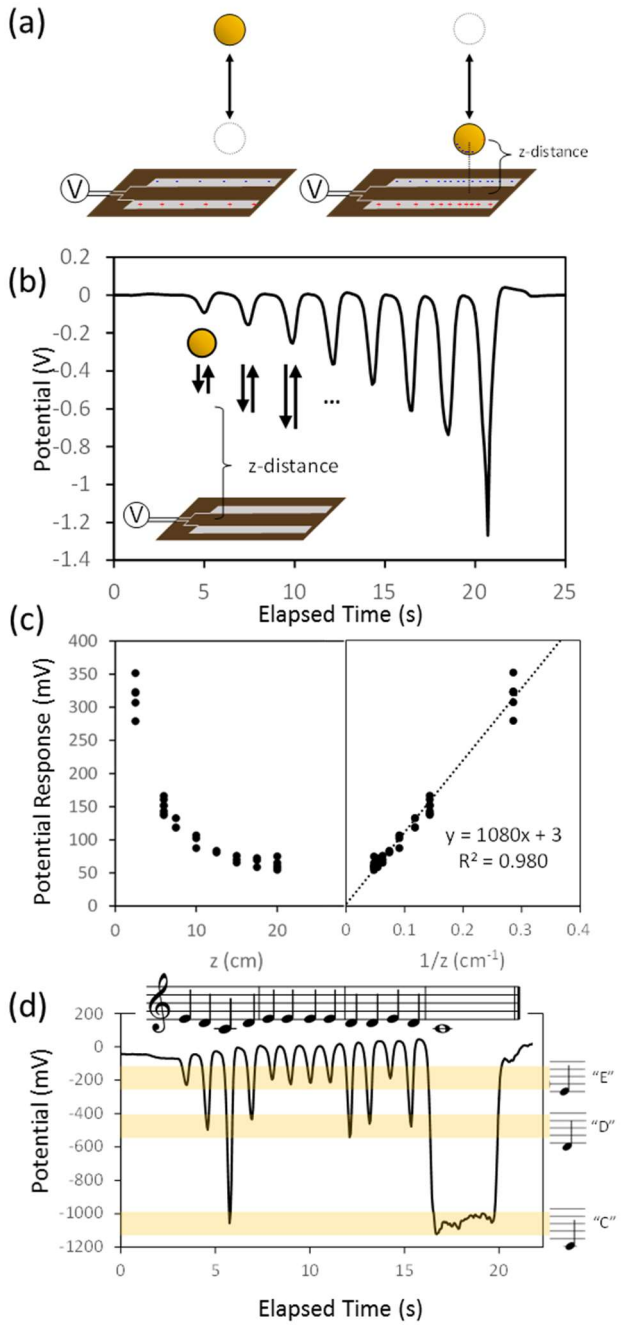

Figure 5.5. Printed GO-SF capacitive position sensor. a) Moving a dielectric object (yellow circle) closer to or farther from the midpoint of the conductive plates alters the distribution of charges supported. b) Recording of raw potential difference between plates as the dielectric object is brought closer-to then father-away from the sensor. c) Potential response and log potential response compared to the z-distance. d) Demonstration of controlled response in proximity sensor by fine-motor gestures. Magnitude of potential response corresponds to note pitch; length of potential response corresponds to note duration.

Controlling the z-position of the dielectric object produces a precise, predictable response that was leveraged to generate a representation of the last stanza of the song "Mary had a Little Lamb" (Figure 5.4d). The magnitude of the potential response (small, medium, large) corresponds to the pitch of the note ("E", "D", and "C" respectively) in the musical score. Attached video file shows a live recording by the GO-SF proximity sensor of the motion of a human hand—generating responses by 1) decreasing z-distance between hand and sensor (large, medium, small response), 2) increasing z-distance (small, medium, large response), and 3) changing z-distance in rapid succession. We envisage that flexible elements for detecting motion, such as the patterned GO-SF demonstrated in this work, will play a key role in the intimate integration of next-generation body monitors and control interfaces on the human body.

Resisitve moisture sensing. Figure 5.6a shows the schematic of resistive moisture sensors printed onto GO-SF film via seriography-guided reduction to a conductive state. A highly conductive reduced wire is fabricated onto GO-SF film with periodic 100 μm dielectric GO-SF gaps. Exposure of unreduced regions to moisture promotes ionic conductivity, leading to a steep drop in resistance across the length of the rGO-SF wire. For instance, under ambient temperature (25 °C), moving the screen-printed GO-SF moisture sensor into a ~97% RH chamber (maintained under saturated K_2SO_4) resulted in a nearly two order of magnitude decrease in resistance within 3.0 seconds (Figure 5.6b). Moving the device out into ambient air (~20% RH) recovers the baseline device resistance after ~1 minute.

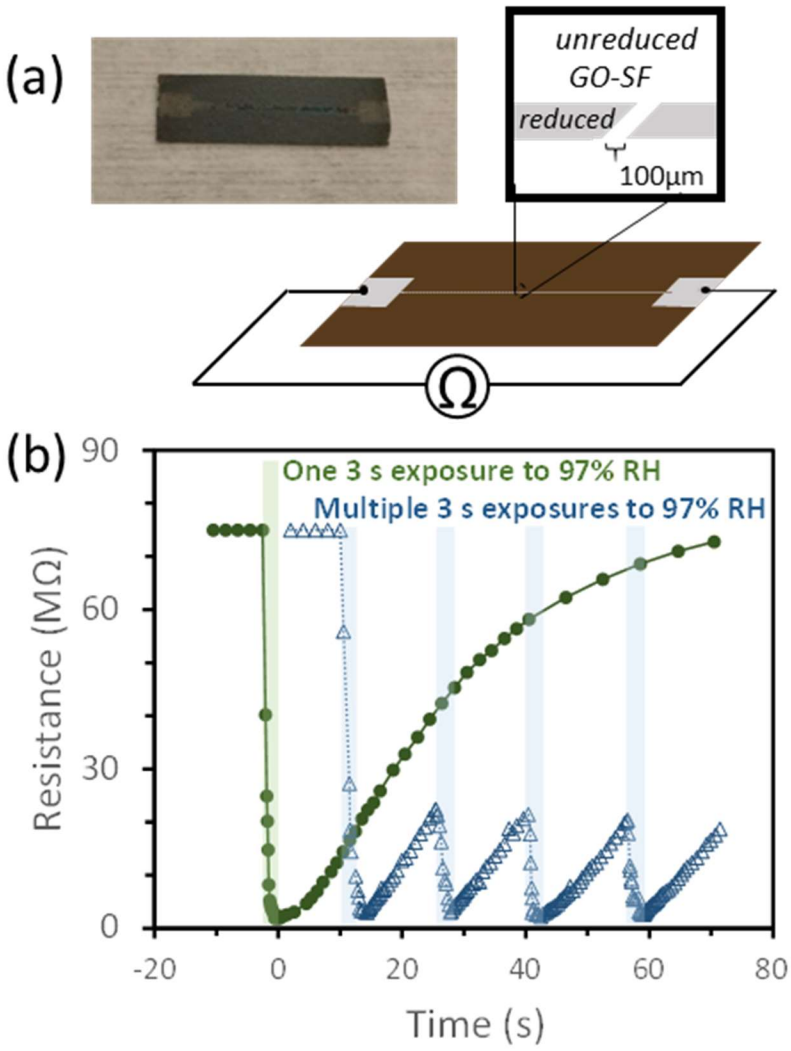

Figure 5.6. Printed GO-SF resistive moisture sensor. a) A conductive reduced wire GO-SF is separated by 100-µm gaps of insulating unreduced GO-SF with a 1.5 mm periodicity. b) Monitoring humidity sensor resistance as a function of humidity for one 3 s exposure to 97% RH with complete recovery of initial resistance (filled green circles), and for multiple 3 s exposures to 97% RH (empty blue triangles).

The response time and sensitivity of this micropatterned GO-SF resistive humidity sensor is competitive with or better than other recently reported graphene-based humidity sensors.[253–257] The facile control over rGO-SF geometry by stencil design also affords a processing route for manipulating humidity sensor characteristics such as sensitivity and response times. Of graphene-based humidity sensors, our screen printed GO-SF sensor is

the only device design that is self-supporting (not backed on a bulky substrate), and does not require the use of elaborate cleanroom based techniques, such as deposition of metal contacts or wafer etching.

Although we showcase two applications—environmental moisture sensor and proximity sensor—in this work, we believe that seriography-guided reduction can offer an important role in the fabrication flexible, large-area microelectronic systems. For instance, we suggest microelectronics fabricated on strong, tough graphene biopapers can be integrated into clothing or comfortably worn on the body. Flexible GO biopapers can be patterned with an array of capacitors for powering body-mounted electronics, and with multiple antennas to transmit information to and from body-mounted sensors.

5.4 Conclusion

This work demonstrates seriography-guided reduction as an affordable, portable, high-throughput route toward generating functional microcircuits across large-areas in strong, tough graphene-silk biopapers. These films are both mechanically and chemically robust, resisting thousands of folding cycles and agitation under varied chemical environments.

The generalizable mechanism for the conversion of graphene oxide by the printed reductant means that this technique can be extended to a broad envelope of present and future graphene-based materials, assembled by different methods, enhanced by different binders. In contrast to existing fabrication schemes, this approach allows for the direct printing-in of conductive circuitry applied toward flexible resistive humidity sensors and capacitive

proximity sensors. Novel approaches for generating robust, resilient, flexible electronics will play a major role in advancing commercial focus beyond conventional wafer-based electronics. We showcase the versatility of seriography-guided reduction through microcircuits designed as proof-of-concept environmental sensors and wearable machine inputs. The simultaneous integration of sensory and command interfaces in robust, compliant thin film nanocomposites will facilitate the proliferation of ubiquitous, pervasive, flexible device components operating under real-world conditions as a part of next-generation smart environments.

CHAPTER 6. Photolithography-Guided Reduction

6.1 Introduction

We report for the first time the generation of flexible micro-supercapacitors in a graphene oxide-silk layered bionanocomposite. Generation of micro-patterned electrodes with sub-micron spatial resolution was accomplished using a novel resist-stenciling technique, enabling the transfer of complex microcircuit designs to a graphene oxide-silk layered substrate as chemically-reduced features micro-features across wafer-length scales. Resist-stenciling can produce micro-patterned reduction features with over 10 times the feature density compared to techniques such as laser-scribing or screen printing. As a proof-of-concept, resist-stenciling was used to fabricate the first 2D micro-supercapacitors integrated into a layered graphene bionanocomposite. These demonstrated a specific capacitance of ~128 F/g, good capacitance retention under charge cycling (87.5% after 2000 cycles), and repeated mechanical bending (82.2% after 20 cycles). Resist-stenciling leverages tools currently in use by the microelectronics industry to enable the scalable, high-resolution conversion of layered nanocomposites into microelectronic circuit, storage and sensing elements.

The world is seeing a proliferation of distributed networks of miniaturized sensors and computers.[258] Connecting and powering these ubiquitous devices presents new challenges not met by current fabrication technologies. For instance, devices interfaced on clothing, on skin, or in the human body need to be soft and flexible, while conventional electronics

are hard and rigid, unable to maintain performance to accommodate bending arising from bodily motion.[48] Additionally, renewable and readily-available sources of energy (including light, wind, wasted energy in body motion, mechanical vibrations, and heat) cannot provide constant power, and are also distributed in nature. One promising avenue is the development next-generation energy-storage devices that are flexible to accommodate diverse use scenarios; and sufficiently small and low-cost to be ubiquitously placed to connect energy harvesters with sensing and computational components.[259]

Graphene oxide (GO) is a prospective candidate material for flexible conductors and energy storage. GO can be exfoliated from earth-abundant graphite using solution-scalable methods, and can adopt a wide gamut of mechanical and electronic properties via its reduction or surface modification.[18,260,261] The structure of GO consists of a monolayer hexagonal network of sp^2 hybridized carbon interspersed with sp^3 carbon bearing oxygen-containing functional groups, with hydroxyl and epoxy groups at the basal plane, and carboxy and carbonyl groups at sheet edges.[262] The removal of these oxygenated groups *via* reduction processes can produce an increase in conductivity by several orders of magnitude (up to 10^4 S/m in graphene oxide-silk fibroin, GO-SF, composites), opening a route toward applications in flexible energy storage.[263–265] Much work has also focused on the assembly of nanocomposites, whereby GO acts as 2D 'bricks' bound by 1D polymeric binders to yield nacre-like structures designed for superior mechanical properties, including extreme tensile strength (526.7 MPa in GO-chitosan),[7] Young's modulus, toughness (13.9 MJ/m^3 reduced graphene oxide-silk fibroin, GO-SF),[266] and stretchability (up to 10.1% in GO-polyvinyl alcohol).[267] Synergistic effects arise from confined networks of intermolecular interactions to produce materials with superior mechanical

properties in composites otherwise comprised of soft constituent components.[19,75,158,268] However, the investigation of layered graphene composites has been largely confined to structural applications,[262,269] and only a few publications explored multifunctional applications or applications in microelectronic components.[270]

Exploration into introducing electrical conductivity into GO via reduction reactions began in earnest in the last decade,[262] and have yielded a plethora of chemical and physical methods. Chemical methods include reduction of GO by diverse reductants such hydrazine,[271,272] melamine,[273] anodic metals,[141,274] ascorbic acid;[275] while physical methods include reduction by thermal annealing,[231,276] electrochemistry,[277,278] microwave pulses,[234] and light irradiation.[279–281] However, most works focus on the indiscriminate, areal reduction of GO. These methods cannot localize the generation of conductive reduced GO features within the critical dimensions required by modern microelectronics, with current generation package substrates approaching sub-10-μm line width/space, and image pixels of camera phones at 1.5 μm.[282–284]

High resolution, patterned reduction of graphene oxide on the single-micron length scale have been reported using strategies such as laser scribing,[285–287] ion beam conversion,[288–290] or contact by hot probe.[239] While these techniques can achieve reduced GO features with critical dimensions of approaching 100-μm for laser scribing, 20-nm for ion beam, and 12-nm for hot probe, ultimately, they are based on serial techniques that cannot scale for high-volume manufacturing across wafer- and panel- sized substrates.

In this work, we demonstrate the efficient fabrication of a flexible, micro-supercapacitors in a flexible, yet mechanically-robust, graphene oxide (GO) bionanocomposite paper

through a novel resist-stenciling technique. This technique employs photolithography to generate a photoresist stencil, coupled with electron beam deposition to localize the placement of chemically-reduced features in the bionanocomposite at photolithographic length scales—demonstrating micro-structured reduced GO features with sub-micron critical dimensions (as small as 0.8-μm). Our method can be generalized to enable the generation of micro-scale electrodes, antennae and interconnects in graphene oxide-based composites, opening a route to leverage the incredible breadth of mechanical and electronic properties of GO and its derivative films.

6.2 Methods

Vacuum-assisted layer-by-layer assembly of GO-SF biopapers. SF binder was extracted from the cocoon of the *Bombyx mori* silkworm in accordance with protocols pioneered by Kaplan *et. al*.[291] Briefly, *B. mori* cocoons were cut and boiled in 0.02 MHa_2CO_2 for 30 min, then washed 3 times with ultrapure (18.2 MΩ-cm) water to yield degummed silk fibers. Silk fibers were solubilized in 9.3 M LiBr (at 1:10 wt. ratio of silk fiber to LiBr solution) at 60 °C for 2 hours. The solubilized SF was dialyzed against water to yield an aqueous stock solution of SF in water at a concentration of 50 mg/ml. Graphene oxide (GO) flakes were exfoliated according to the method of Hummers' from natural graphite powder (325 mesh, Alfa Aesar, USA) and diluted by ultrapure water to 5 mg/ml.[79] To the GO dispersion was stirred the SF suspension to yield 3% dry weight SF. The GO-SF was collected onto a membrane filter (Pall Versapor, acrylic copolymer, 0.2μm pore size) via a

vacuum filtration setup to yield GO-SF biopapers with a flat side (filter side), and a rough side (air side).

Fabricating of resist stencil to guide biopaper reduction. The rough side of the GO-SF biopaper was mounted against a glass slide by glue stick. A patterned phototresist layer acts as a stencil to protect regions again reduction. In a typical experiment, negative-tone NR9-1500py ((Futurrex, Frankling, NJ, USA) was diluted in cyclohexanone and spin-coated onto the GO-SF biopaper to yield a 500-nm layer. The resist was exposed to 365nm UV through a chrome photomask (PhotoSciences Inc.) with computer-aided design of microelectrode arrays. The resist was soft-baked and post-exposure baked at reduced temperature (80°C), as typical bake temperatures of 150°C was found to cause warping in GO-SF biopaper. Resist was immersion-developed (3:1 RD6/water) to yield stencil pattern protecting regions of the GO-SF against subsequent metal-assisted reduction.

Generation of conductive micro-traces in GO-SF biopapers. Electrochemical reduction of exposed GO-SF was undertaken by using a metal-assisted reduction technique based on methods previously reported by our lab.[264,265] A 500-nm thick layer of Al, an anodic metal, was deposited via E-beam deposition (Mark 50, CHA Industries) onto the resist-stenciled GO-SF biopaper. The Al-coated GO-SF was dampened with ultrapure water (18.2 MΩ-cm), and clamped between PFTE blocks to undergo reduction for 4-hr, generating a depth of reduction feature of 1.2 μm as determined in a previous work.[265] The Al-coated GO-SF is agitated in acetone to strip the residual resist, and lifting off large regions of coated Al. Residual Al was removed by washing the GO-SF biopaper in 0.1M HCl, and ultrapure

water to yield GO-SF biopapers with micro-patterned conductive regions in the negative pattern of the photomask.

Characterizing reduced features in GO-SF biopapers. Reduced features on GO-SF biopapers were imaged by optical microscopy using a Leica DM 4000, and by low-voltage cold field emission scanning electron microscopy (Hitachi SU8230). Verification of chemical reduction was done by X-ray photoelectron spectroscopy (Thermo Scientific K-alpha), and Raman spectroscopy (Alpha-WiTec Alpha 300R, 532-nm laser).

Fabricating and characterizing micro-supercapacitors integrated into GO-SF biopaper. Conductive features were fabricated in the shape of interdigitated electrode pairs using resist stenciling to guide the reduction of GO-SF biopaper. The reduction patterned biopaper was soaked in 6M KOH for 1-hr under vacuum to allow for intercalaction of electrolyte. The electrode busbars were clamped against Pt wires and connected to potentiostat (VersaSTAT 3, Princeton Applied Research) for CV characterization at different scan rates (10, 50, 100, 200, 500, and 1000 mV/s). C_{sp} was evaluated by voltammetric charge divided by potential window, scan rate and mass of active material. Voltammetric charge was determined by sum of integrated area of anodic and cathodic sweeps. The mass of the reduced GO-SF active material was determined by expression: active material area × reduction depth × GO-SF density, where reduction depth is 1.16 μm, and reduced GO-SF density of 1.8 g/cm^3.[265] Cyclic bending/unbending was performed by mechanical manipulation of patterned GO-SF within a hinge (bend angle 90°, bend radius ~1 mm) at 100 mV/s.

6.3 Results

Guiding metal-assisted reduction via photolithography. **Figure 6.1** shows the process scheme for generating conductive micro-traces using resist templating. A typical photolithography process is employed to generate a resist-based mask that protects selective loci of underlying GO-SF from contacting the reductant. Using electron-beam deposition, an anodic metal such as Al is deposited through the resist mask. Here, the patterned resist acts as a conformal stencil to enable the transfer of the reduction pattern onto the underlying layered nanocomposite. GO-SF in contact with the aluminum undergoes controlled reduction as explored in a previous work.[265] The E-beam deposition of other common deposited metals such as Cu and Ti can also induce reduction, though to a lesser extent than by Al as demonstrate in a previous work.[152,265] Stripping the residual resist and washing the GO-SF biopaper lifts off the deposited Al and reveals reduced, conductive features written into the surface of the GO-SF biopaper (**Figure 6.2**).

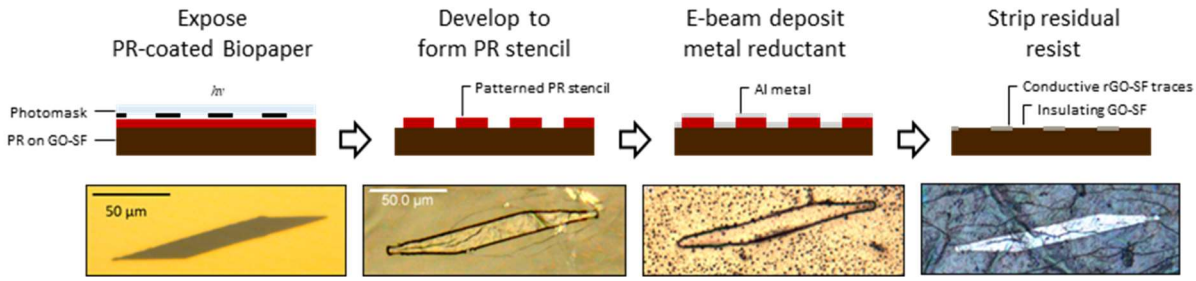

Figure 6.1 Fabrication of conductive micro-traces in flexible, strong, tough GO-SF biopapers via photolithography to guide metal-assisted reduction. Inset images show from left to right, optical micrographs at each step of i) photomask, ii) resist with transferred mask pattern, iii) deposition of aluminum reductant, and iv) conductive feature patterned in GO-SF after stripping resist.

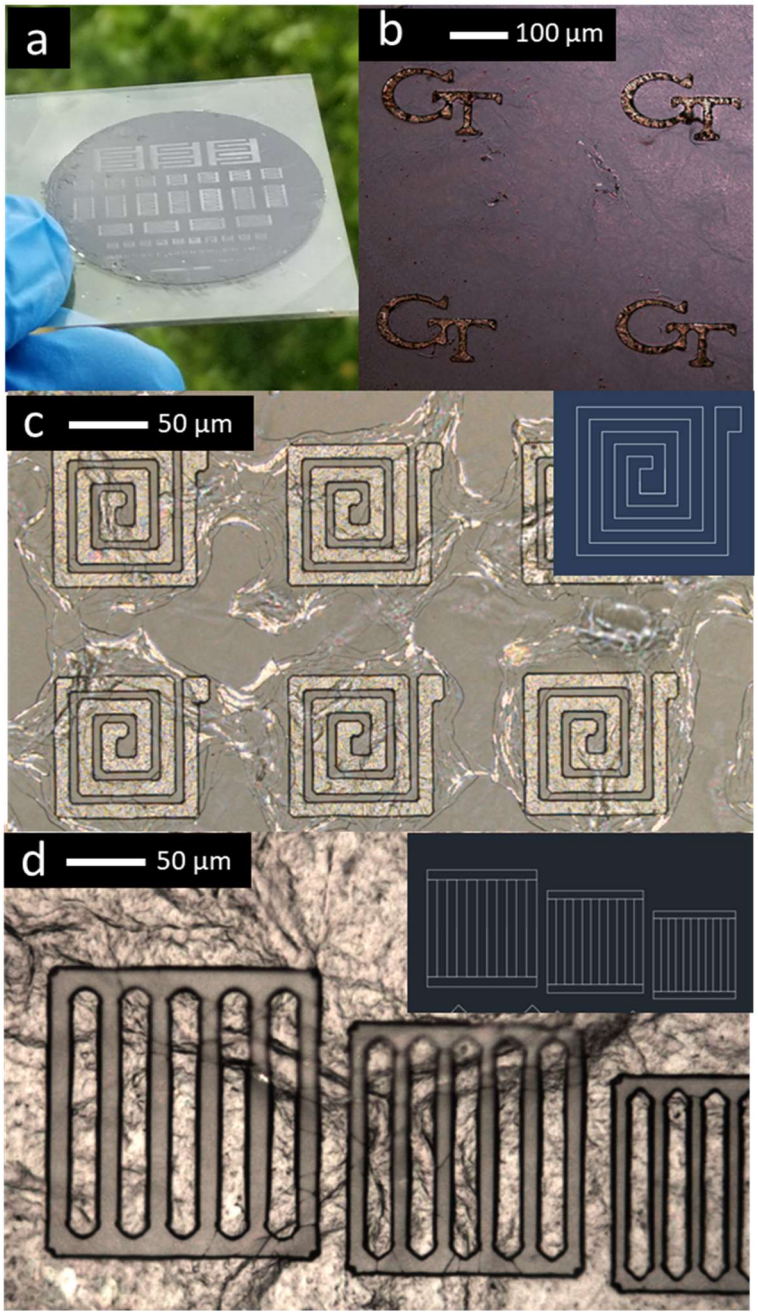

Figure 6.2. a) Photograph showing GO-SF biopaper patterned with an array of micro-supercapacitors. Optical micrographs of micro-patterned reduced GO-SF by resist stenciling in the b) Georgia Tech logo, c) antenna motifs, and d) grating motifs.

The resist-stenciled method for patterned reduction described here is highly compatible with common photolithography processes. Herein, we successfully generated conductive features using both representative positive and negative tone resist stencils respectively.

Modifications were made (see methods) to avoid baking at high temperatures, which would cause warpage of the GO-SF biopaper due to mismatching coefficients of thermal expansion between layers and trapped moisture within the GO-SF. Reducing warpage ensured flat contact between the photomask and the resist-coated GO-SF to ensure optimal pattern transfer. The spin-coated resist helped make smooth inherent roughness on the surface of the GO-SF biopaper (R_q = 52 nm). Conformal contact between the resist mask and the GO-SF biopaper means the resist stencil acts as a hard stop against the reducing agent contacting protected areas. Other scalable methods of patterned reduction cannot ensure conformal contact. For instance, in shadow masking flash lithography, separation between mask and GO-based substrate creates broad drop-off of reducing radiation intensity;[281] while in stamping, asperities may block contact in surrounding loci to the reductant.[141] While screen printing can create conformal contact between reductant and GO composite surface, the deposited reductant may deform due prior to and during firing to fix the reductant paste shape.[264]

Characterizing reduction of GO component. **Figure 6.2**a shows a photograph of a GO-SF biopaper with patterned chemically-reduced features. Regions of the biopaper that have undergone reduction change in visual appearance from the dull and brown characteristic of protected GO-SF biopaper to a grey and shiny appearance.[262] **Figure 6.2**b-d shows optical micrographs illustrating the wide variety of accessible geometries of conductive features that can be formed by the patterned reduction process. Using a common negative tone resist system, we obtained conductive features in the GO-SF with line widths as small as 800nm. This critical dimension of conductive features written into the biopapers in this study was found to be defined by the dimensions of the resist stencil that is generated on

top of the GO-SF biopaper. We expect the critical dimension of stencil features can be made even smaller with further optimization of process variables in the exposure, bake and development steps. However, resist stencil features would be unlikely to match reported resolution limits on ideal substrates like polished Si, due to the biopaper substrate having a higher roughness which interferes with photomask placement during exposure, and lower thermal conductivity which may produce suboptimal bake times that affect resist development profiles.

Besides change in visual appearance after guided reduction by resist stencil, **Figure 6.3** shows independent confirmation of chemical conversion by X-ray photoelectron spectroscopy (XPS) and Raman spectroscopy analyses. XPS reveals that the C/O ratio increases in regions exposed by the resist stencil to 3.6±0.2, whereas protected regions retain the C/O ratio of 2.3±0.1 matching the C/O ratio of the as-prepared biopaper.[141] This increase in the C/O ratio supports the partial removal of oxygen-containing moieties from the surface of GO-SF biopaper exposed by the resist stencil. The C1s spectra collected was deconvoluted into peaks centered around binding energies of 284.7, 286.5, and 288.5 eV; corresponding to carbon in the chemical states C-C, C-O, and C=O/O-C=O respectively. Deconvoluted spectra show that the biopaper protected by the resist stencil has a significant fraction of surface carbon in higher binding energy chemical states, characteristic of carbon in oxygenated moieties represented in common models of GO.[262] Surface carbon in the biopaper unprotected by the resist stencil shifts toward lower energy chemical states indicative of sp3 and sp2 carbon-carbon bonds.

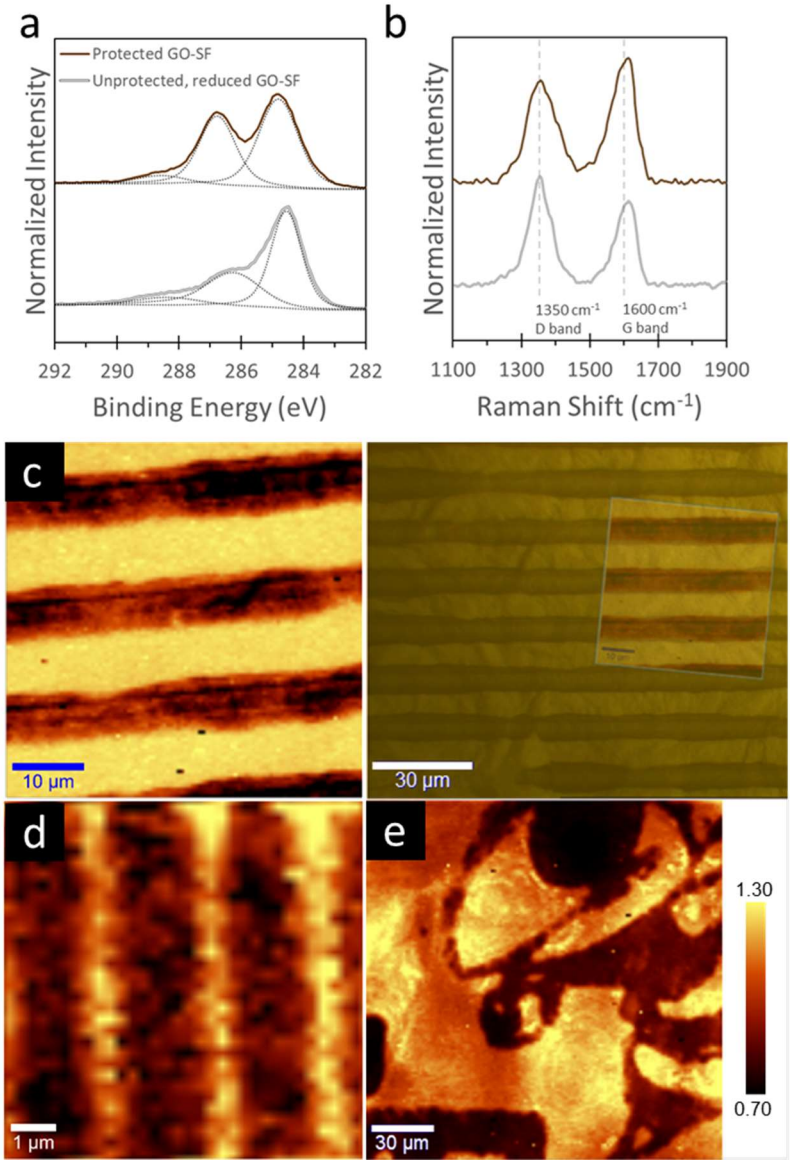

Figure 6.3. a) XPS, and b) Raman point spectra showing GO-SF biopaper before (top, solid brown line) and after (bottom, hollow grey line) photolithography guided reduction. c) Raman mapping of 1350 cm^{-1} D-band to 1600 cm^{-1} G-band peak intensity ratio of c) 10-um lines (optical micrograph overlay on right), d) 800-nm lines, and e) "Buzz" the Georgia Tech mascot.

Figure 6.3b shows Raman spectra collected from biopaper points protected and unprotected by the resist stencil. The D and G-bands (centered at 1350 and 1600 cm^{-1} respectively) from graphitic materials are clearly visible in each case. Regions unprotected

by the resist stencil and exposed to the Al metal reductant show a simultaneous decrease in D-band width and increase in relative D-band peak intensity from 0.92 to 1.19. This increase in D-to-G band peak intensity is indicative of graphitization associated with GO reduction.[292] We use this change in relative peak intensity to map the areal extent of reduction (**Figure 6.3**c-e), with lighters colors signifying chemical reduction and corresponding to regions exposed by the resist stencil. Raman mapping reveals that features in the resist stencil such as fine 0.8-μm width lines, and curves in complex patterns such as in "Buzz" translate into reduced features. Examination of Raman mapping of line patterns (**Figure 6.3**c, d) also reveal an abrupt transition in peak intensity ratio with a width that corresponds with the stencil pattern line width of 10um and 0.8um respectively.

Integrated micro-supercapacitors on GO-SF biopapers. We demonstrate the application of resist stencil-guided chemical reduction by fabricating integrated, nonflammable micro-supercapacitors into flexible GO-SF biopapers with enhanced mechanical robustness. Interdigitated electrode pairs are fabricated across the surface of GO-SF biopapers (**Figure 6.2**a), as small as $9*10^{-4}$ mm^2 in footprint area, and having 2-um interdigitated finger width and gap separation. While pristine GO on its own has properties that promote energy storage such as high specific surface area and surface moieties that promote pseudo-capacitive faradaic reactions, its performance as an active material is limited by low electrical conductivity due to the presence of oxygenated moieties that disrupt the sp^2 basal plane.[263,293] While the presence of interspersed SF in GO-SF biopapers promote GO flake spacing, it further lowers the conductivity to ~1×10^{-2} S/m.[265] On the other hand, metal-assisted reduction increases electrical conductivity of GO-SF by over 6 orders of magnitude up to 1.5×10^{-2} S/m.[265] As a control, Pt wires secured with a spacing of 2.4 mm

by micromanipulators across protected GO-SF show negligible integrated area and capacitance by CV testing.

Here, resist stenciling enables the rational placement of micro-structured reduced GO-SF features as interdigitated fingers and busbars to facilitate charge collection, and electric double layer formation across the large area at the patterned electrode surface and edges. We showcase the fabrication of interdigitated microelectrodes with as small as 2-μm fingers, and $9*10^{-4}$ mm^2 footprint.

Solid state micro - double layer capacitors (EDLCs) were fabricated by swelling the produced and patterned GO-SF paper in an aqueous 6M KOH solution to induce ionic conductivity and effectively fabricate a silk gel electrolyte. Reduced portions of the paper serve as electrodes, while the electronically insulative portion in between the electrodes serves as a separator. Using cyclic voltammetry (CV), we investigate the charge storage behavior of the micro-patterned GO-SF.

EDLCs with a rather thick (400 μm width) busbars collecting current from interdigitated and still relatively thick (200 μm) width fingers (**Figure 6.4**a, inset), forming symmetric electrodes. The separator membrane portion was designed to exhibit serpentine shape and a relatively large width of 200 μm (Figure 4a, inset). Note that "regular" commercial devices typically utilize thinner (75-50 μm) electrodes and thinner (10-25 μm) separators to achieve higher power capabilities. We utilized larger dimensions for simplicity sufficient for this proof-of-concept device fabrication.

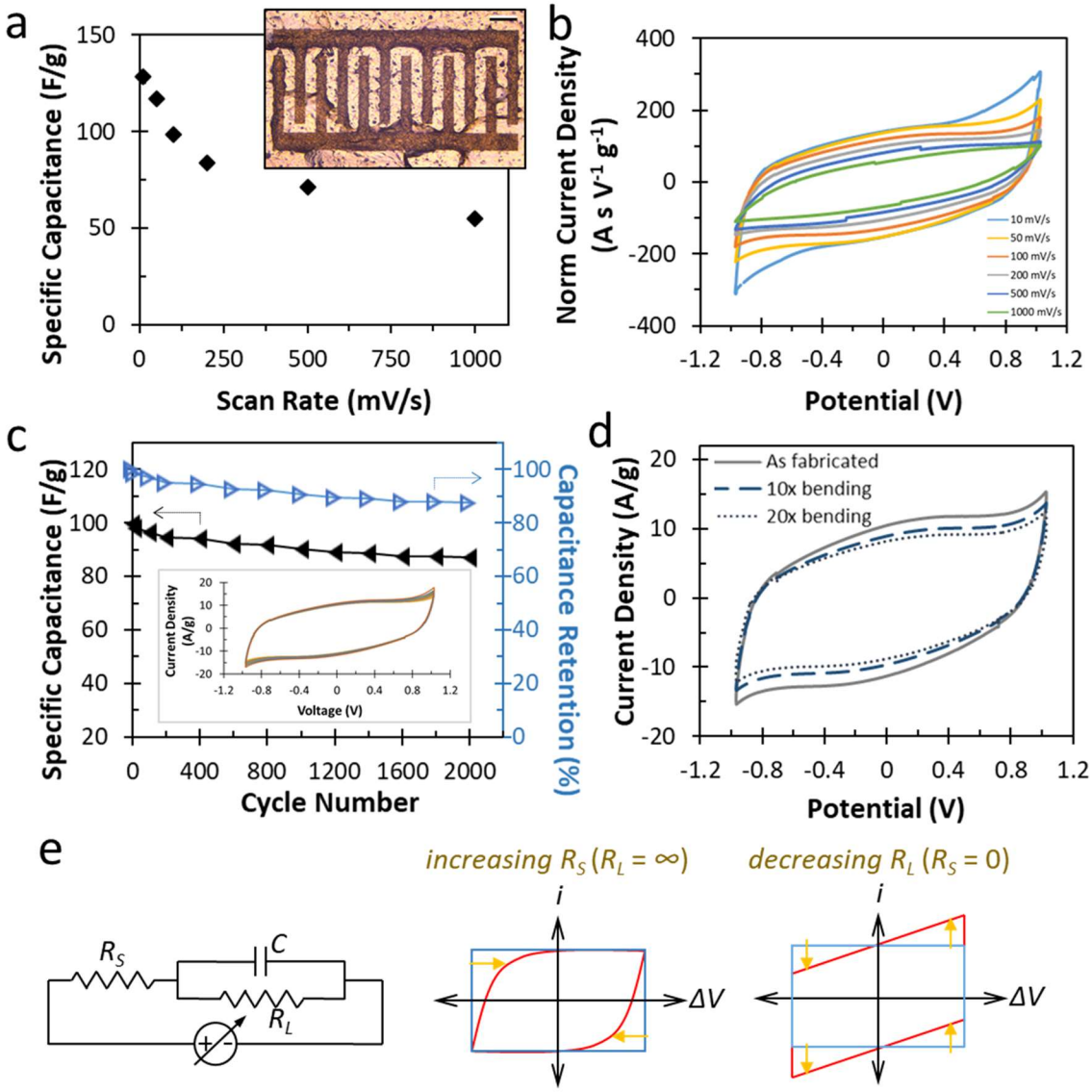

Figure 6.4. a) Scan rate dependent specific capacitance in 6M KOH of reduced GO-SF EDLC shown in inset (scale bar 500 μm). b) CV profiles of GO-SF EDLC normalized by scan rate. c) Charge cycling behavior of GO-SF EDLC. Inset shows CV profiles from 1st cycle through the 2000th cycle. d) GO-SF EDLC behavior at 100 mV/s under repeated mechanical agitation by bending at 90°. e) Simple equivalent circuit model of a EDLC device and the effect of changing the solution resistance (R_S) or leakage resistance (R_L) on the cyclic voltammogram profile.

As a control, Pt wires secured with a spacing of 2.4 mm by micromanipulators across protected GO-SF show negligible integrated area and capacitance by CV testing. At a scan

rate of 10 mV/s, the specific capacitance (C_{sp}) of fabricated devices reach ~130 F/g, which is comparable with many reduced GO-based and activated carbon-based electrodes reported previously (up to ~150 F/g in aqueous KOH-based gel electrolytes).[294–297] Distortion from the perfect horizontal rectangular shape of an ideal EDLC CV (**Figure 6.4**b) might be expected due to large electrode and separator dimensions and the associated increased contribution of the electrolyte resistance as well as other factors.[298]

Figure 6.4e illustrates the effects of increasing the equivalent series resistance (R_S) and increasing the leakage current (or decreasing the leakage resistance, R_L) on the shape of the cyclic voltammogram curve, given a simple equivalent circuit model of an EDLC. Clearly, in the experimental curves, a significant equivalent series resistance is revealed. Runaway electrolyte decomposition at extreme potentials (discussed more below) may be described as a form of current leakage current, but cannot be described with a constant resistance R_L. (Given the large equivalent series resistance and significant current runaway at extreme potentials, we do not try to deconvolute the magnitude of any potential difference-independent/constant leakage resistance.) More specifically, such distortions may generally be associated with (i) kinetic limitations (e.g., insufficiently fast ion transport from the bulk of the electrolyte to the graphene surface to form a double layer), particularly evident at faster sweep rates; (ii) leakage current (e.g., due to insufficiently high electric resistance of the GO-SF composite or parasitic side reactions); (iii) electrolyte decomposition (particularly at higher voltages) and (iv) various redox processes (e.g., pseudocapacitance reactions). Reducing electrode/separation layer dimensions by, for example, 4 times or more (to approach typical dimensions in commercial EDLCs) should enhance the rate performance of the device by over 16 times and reduce the contribution

of the electrolyte resistance to the slope observed in the CV curves by 4 times. Based on the low electrical conductivity in GO-SF layer, which should be reduced further upon silk swelling in the electrolyte we expect that its contribution to the leakage current to be insignificant. The sharp current increase observed at above 0.7V in our symmetric EDLCs is associated with water decomposition and is typical for KOH-based aqueous electrolyte solutions.[295] We do not observe a clear redox peaks within 0.6V. However, this does not necessarily mean that the contributions of Faradaic reactions and pseudocapacitance is negligible because in many cases the pseudocapacitive materials exhibit very broad CV peaks.[299]

In order to observe accelerated aging we tested cycle stability of the produced EDLC at a relatively high maximum voltage of 1V (compared to 0.6V commonly used in academic studies to avoid decomposition of water, electrode drying and formation of micro gas bubbles that further reduce access of electrolyte to the inner electrode surface area. Still the observed stability of micro-EDLCs fabricated in GO-SF was quite reasonable. The device retained ~88 % after 2000 charge cycles, which is in-line with laboratory-fabricated EDLCs with gel electrolytes cycled in a similar voltage range.[295] Yet, it is inferior to EDLCs based on regular aqueous electrolytes, cycled within a lower voltage window and commonly comprising excess of electrolyte, which may show similar capacity retention after over 100,000 cycles or more.

Micro-patterned GO-SF EDLCs also demonstrate high mechanical robustness. Whereas layered composites, such as pristine GO paper, show low wet strength and will swell and fall apart in aqueous solution—the SF binder preserves the integrity of the GO-SF

biopapers in the electrolyte. This enables the micro-supercapacitors fabricated in GO-SF biopapers to undergo repeated 90° bending (bend radius as little as ~1 mm) without tearing. CV profiles show that the GO-SF still preserve a large integrated area, retaining 82.2 ± 7.1% of original capacitance after 10 bending cycles, and 77.0 ± 8.9% capacitance after 20 bending cycles (**Figure 6.4**d). We believe the decreased EDLC performance to arise form bending causing closure of pores on the surface of the reduced GO-SF microelectrodes, decreasing the total electrode surface and ability to support the electrical double layer. However, we note that the capacitance retention is significantly higher for the second set and subsequent sets of bending. This presents a tradeoff whereby the capacitance retention during device operation can be tuned high at the expense of rated capacity by 'priming' the GO-SF micro-supercapacitors via pre-bending.

Unlike the previously reported macroscopic EDLCs, the flat and flexible micro-EDLCs generated by resist-stenciling can readily integrate into miniaturized packages and into current generation 2D integrated circuits. We expect that C_{sp} of GO-SF micro-EDLCs could be further increased with optimization of electrolyte, to enhance microelectrode double layer coverage; and the inclusion of transition metal oxide nanoparticles (such as VOx, CoO, NiO, Fe2O3, RuO_2 or MnO_2) to enhance contribution from pseudocapacitance.[263] In the latter example, highly conductive graphene features generated by resist-stenciling can enhance the traditionally low conductivity associated with oxide-based pseudocapacitive materials.

6.4 Conclusion

We report for the first time the fabrication of sub-micron chemically-reduced features in a graphene oxide-silk bionanocomposite. We accomplish this through guiding the electron-beam deposition of reductant using a photoresist stencil—generating conductive micro-pathways in GO with feature density over an order of magnitude higher than previously reported techniques such by laser-scribing or screen printing. Because this novel technique for GO reduction leverages common wafer- and panel-level scale techniques in the microelectronics industry, it can achieve an unprecedented combination of resolution and manufacturing scalability.

The successful transfer of complex electronic circuits into a layered GO bionanocomposites opens the possibility of robust, tough, yet flexible, electronic components to be assembled from Earth-abundant, low-embedded energy materials such as silkworm silk and graphite. We showcase here that complex reduction features in GO-SF in the form of antenna, wire interconnects, and energy storage devices, as flexible micro-electric double layer capacitors with high specific capacitance of ~130 F/g. The GO-SF micro-supercapacitors are extremely robust—they do not short-circuit and do retain their capacitance even after repeated mechanical bending and charge cycling. This work opens a route for layered nanocomposites to be converted into microelectronic substrates, interconnects and components that can enable the proliferation of ubiquitous sensing and computing.

CHAPTER 7. Stretchable biopapers by computerized dragknife for pop-up electronics

7.1 Introduction

We present a facile, two-step approach that transforms large-area sheets of bio-enabled graphene nanocomposite papers into multi-dimensional geometries for pop-up and stretchable electronics such as wire interconnects and energy harvesters. Water-vapor annealing facilitates the controlled plasticization of the composite paper, allowing highly localized kirigami cuts by programmable drag-knife. By adjusting drag-knife depth, we can generate a micro-scale array of full- and partial-cuts, enabling a purely topological approach toward the elimination of metastable fold states in kirigami structures, and the precise placement of crack fracture paths. Through orthogonal control over bionanocomposite conductivity, we showcase this biopaper system as a platform for prospective soft and shape-transforming electronics.

Modern electronics are largely based on conventional semiconductor components linked by noble metal interconnects through multi-stage print and lithographic processes.[300] However, these devices have an environmentally-harmful lifecycle, often involving toxic chemicals or high embedded energy in material extraction, material processing and waste by-product treatment. Accumulation of such bulky electronic waste in landfills bears

significant threat to environmental and human health.[301,302] Additionally, conventional electronic materials have a fixed form-factor and inability to adapt their shape or performance in response to the external stimuli. Devices fabricated from these materials are bulky, and often cannot accommodate strains without material failure.

In order to accommodate large and complex strain scenarios, some research has recently focused on using kirigami, the art of paper cutting, to inspire the design of stretchable electronic materials.[43,46,210,303–306] However, these studies have been primarily limited to the processing of a small selection of materials such as silicon, paper, and elastomers by binary cutting techniques such as laser cutting,[43] masked ion etching,[46,307], or macroscopic cutting.[308] These techniques are limited to generating one type of cut, through the entirety of the material, and often only in simple geometries such as rectangular cut-patterns that enable simple 1D stretching.

In this work, we introduce a novel programmable drag-knife approach toward the fabrication of kirigami structures of non-traditional graphene papers *reinforced* with silk fibroin (SF) that enables significant 3D strain responses. Unlike previously reported kirigami studies, this approach is the first to afford control over cut pressure, position, depth and biocomposite integrity over large areas, opening a route toward the generation of complex internal biaxial stress distribution control via a combination of partial-cuts as well as through-cuts patterns. Having partial cut depth control enables the design of preferential creasing, programmable directionality for out-of-plane buckling, and pre-defined loci of weakness for controlled material failure. We exploit this art of partial cuts to demonstrate various human-scale structures for pop-up electronics. The drag-knife kirigami approach

suggested here enables the reconfiguration of GO-silk structural and mechanical properties at the macro- and meso-scales, while retaining superior properties such as the capacity for the GO components to be reduced to yield a highly conductive percolating rGO network enabling next-generation reconfigurable bioelectronics by fabricating a GO biopaper energy harvester.

The graphene oxide-silk fibroin (GO-SF) composite system explored in this study have been suggested as advanced bio-enabled nanomaterials for various structural and sensory applications.[19,152,186,309,310] Since the discovery of graphene papers,[142,144] their mechanical and electronic properties have been greatly refined and expanded through the inclusion of composite binders,[8,161,311,312] active functional components,[313–315] and processing control.[316,317] For example, we showed that evaporation of water solvent from a Meyer-bar cast graphene oxide (GO) and silk fibroin (SF) aqueous slurry leaves the GO and SF assembled into a robust, nacre-like multilayered composite across large-areas (up to 0.5 x 0.5 m^2 in this work).[264] The network of hydrogen bonding formed between moieties on GO and SF components assembled in a layered matter are thought to be the origin of synergistic strengthening and toughening with ultimate strength of up to 300 MPa, and toughness of 2.3 MJ m^{-3}.[84]

However, these bionanocomposites have limited processability due to their resulting high mechanical robustness after the constituent components form their network of intramolecular interactions during solvent removal. An additional challenge is that as new bionanocomposites are developed with prioritized strength or modulus, this often makes these materials susceptible to brittle, catastrophic modes of failure at modest strains. This

results in a macroscopic geometry fixed to their as-manufactured form factor as flat sheets either in the shape of the filtration funnel for vacuum-assisted filtration, or the container for cast-drying.

7.2 Methods

Fabrication of GO-SF bionanocomposite papers. The SF binder for the biopapers was extracted from the cocoon of the *Bombyx mori* silkworm in accordance with established sericulture protocols.[291] The suspended SF was dialyzed against water to yield a stock solution concentration of 50 mg/ml. Graphene oxide (GO) flakes were exfoliated from natural graphite powder (325 mesh, Alfa Aesar, USA) using Hummer's method,[79] and diluted by ultrapure water (18.2 MΩ-cm) to 5 mg/ml. The GO dispersion was mixed with the silk fibroin suspension by stirring to yield a GO-to-SF weight ratio of 50:1. The GO-SF dispersion was cast-dried in a dish lined with fluorinated ethylene polymer (Teflon FEP, DuPont), with a typical sheet cast across a 0.5-m by 0.5-m area, with a dry-thickness of 30 microns.

Generation of patterned cuts in GO-SF biopapers. The GO-SF biopaper was mounted onto a vinyl substrate (OraCal 651) as a release liner. The mounted GO-SF biopaper was placed in an enclosed chamber with a humidifier (~100% RH, 1 hr) to enable the GO-SF for cutting by water plasticization. The water-plasticized GO-SF biopaper on substrate was cut using a drag knife (carbide blade 60° from Tormach) under computerized numerical control (Silhouette CAMEO 3) with cuts made by media-moving with a mechanical step

resolution of 10-µm, a typical kerf width of 20-µm, and at speed up to 0.1 m/s. Each pass of cut patterns was designed using a graphics editor (Inkscape), and cut depth controlled by blade offset (1.25x thickness for full cuts, 0.75x thickness for partial cuts). Mountain cuts were made by partial cut from the top side of biopaper. Valley cuts were made by partial cuts from the bottom side of the biopaper--made by turning over the biopaper, aligning against cut fiducial marks, before making second set of partial cuts. Mechanical characterization was performed using a Shimadzu EZ-SX tester. Cut interfaces were characterized using atomic force microscopy (Bruker, Dimension ICON), and scanning electron microscopy (Hitachi SU8230).

Generation of conductive micro-traces in GO-SF biopapers. Highly conductive reduced GO-SF film was generated from the metal-assisted reduction of GO-SF using previously established methods.[264,265] For large-area conductive regions, 500-nm thick Al was deposited onto the cut GO-SF biopapers *via* electron beam evaporation (CHA Mark 50, CHA Industries). For patterned conductive traces with features with a critical dimension as small as 70-um, an Al metallization paste (EFX-37, Monocrystal) was applied through a stencil screen (500TV front-contacting, Haver&Boecker). The Al-patterned GO-SF was dampened with ultrapure water (18.2 MΩ-cm), and clamped between PFTE blocks overnight. Using a stream of water to rinse away the Al yields highly conductive rGO-SF biopaper, with highly conductive features. Verification of extent of reduction utilized X-ray photoelectron spectroscopy (Thermo Scientific K-alpha), and Raman spectroscopy (Alpha-WITec 300R, 532nm laser).

Fabrication of single-electrode triboelectric nanogenerator. A soft PDMS was prepared from a weight ratio of 20:1 Sylgard 184 base to curing agent. A 3-mm thick PDMS base layer was cast into a 3-in Petri dish. Trapped air bubbles were removed by vacuum desiccation, and the PDMS mix was soft-cured (80°C oven for 0.5 hr). A 24-gauge (0.51mm) Cu wire was held in contact with the reduced surface of the cut-patterned GO-SF biopaper, and placed on top of the PDMS base layer. A 3-mm thick PDMS top layer was cast over the rGO-SF biopaper and Cu wire. Trapped air bubbles were removed by vacuum desiccation, and the GO-SF device encapsulated in PDMS was cured (80°C oven for 1.5 hr). The PDMS was cut around the rGO-SF device. The end of the Cu wire was stripped of the PDMS to serve as the current collector.

7.3 Results

7.3.1 Making kirigami structures by numerical-controlled drag knife.

To generate intricate cut patterns with critical cut dimensions as small as 20 microns into bionanocomposites, we introduce a novel two-part drag-knife kirigami process whereby first the biopaper undergoes a water-vapor plasticization, followed by pressure-controlled cutting using a computerized numerical control (CNC) drag knife (**Figure 7.1**a) (see Experimental). In as-cast biographene papers the drag knife plowing leaves visible pull-out features from the separation of the layered GO-SF materials. Therefore, for strong and tough GO-SF biocomposites to be made amenable to kirigami patterning, the GO-SF sheets are treated in water vapor, a known plasticizer for biomaterials.

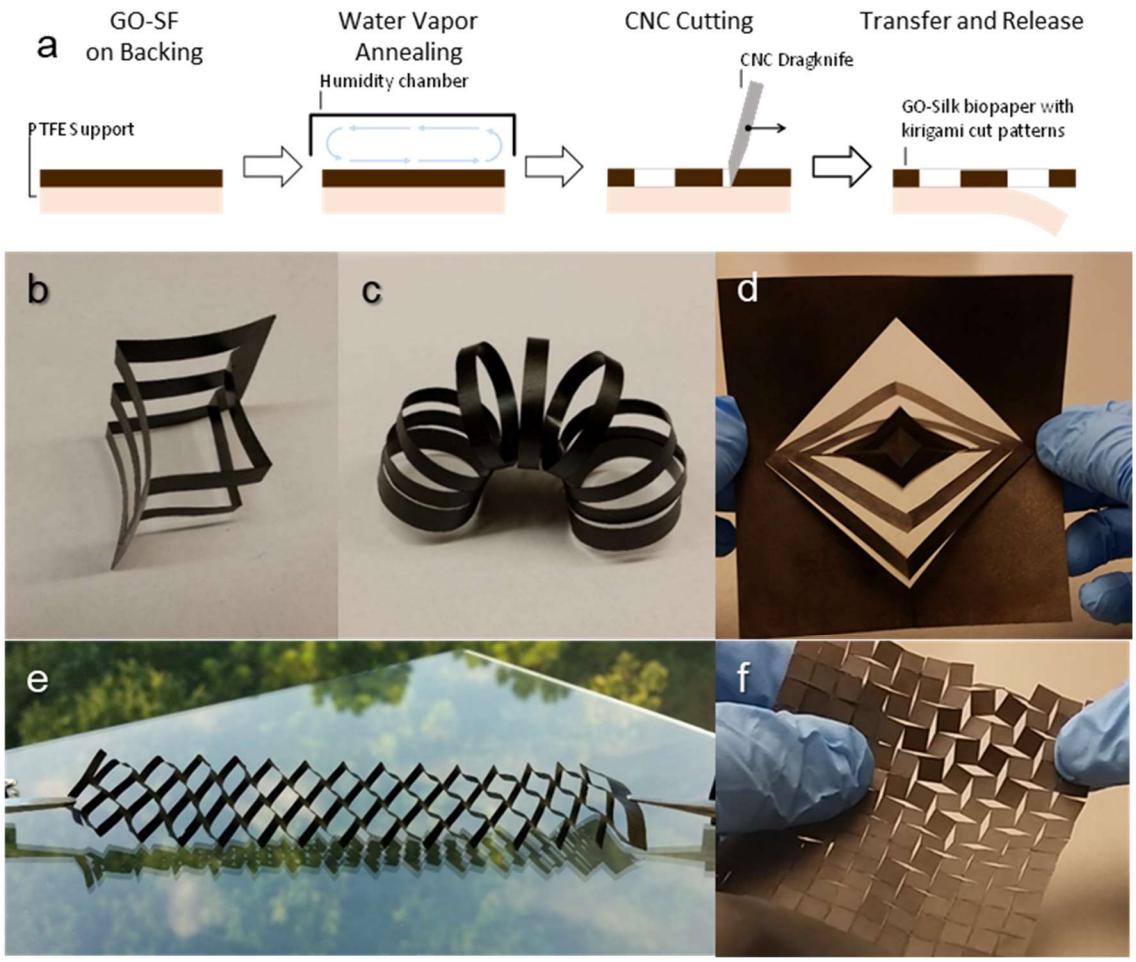

Figure 7.1. a) Schematic of two-step generation of patterned cuts in biographene nanocomposites by drag-knife kirigami. Array of accessible GO-SF biopaper geometries on the human length-scale in the form of b) pop-up box, c) spiral slinky, and d) spinner; e) 1D stretchable pattern of parallel cuts, and f) 2D stretchable auxetic square cuts.

The intercalated water molecules increase free volume in the composite, creating a lubrication effect that facilitates sliding between the component molecules and disrupting the hydrogen bonding network, making otherwise strong and brittle materials susceptible to controlled localized plastic deformation.[318,319] We find that beyond a threshold time of water-vapor treatment of 20 min, the drag knife makes perfect cuts without leaving visible pull-out features from the separation of GO-SF layers. After returning the biopaper to ambient conditions (40% RH), the unperturbed GO-SF retains its dry-state properties.

7.3.2 Controlling GO-silk biopaper cross section through partial cuts.

In the cutting step, pressure is exerted by the edge of a computer-numerical controlled high-angle (60°) blade, displacing the water-plasticized GO-silk biopaper to form cut features with a mechanical step-resolution of 10-μm (see Experimental). The controlled out-of-plane buckling of cut-patterned GO-SF biopapers enables a diverse array of geometries (**Figure 7.1**b-f). The versatility of accessible design patterns opens a route toward the tuning the mechanical properties and shape transformation pattern. Among successfully implemented designs in this study are a 1D stretchable pattern of parallel slits (**Figure 7.1**e), a 2D stretchable auxetic sheet, 3D self-supported pop-up cube and helical spring (**Figure 7.1**b, c), a moving 3D pop-up spinner, and a long, flexible conductive wire interconnect (**Figure 7.3**e). The as-cast GO-SF films are exceptionally strong, with an ultimate strength of 140 MPa with large-area sheets showing an average strain at break of 1.8% and elastic modulus of 7.3 GPa. With one perpendicular partial cut (10- μm blade extension) in a GO-SF biopaper coupon with 2-mm x 40 μm cross section and 20-mm gauge length, we see average ultimate strength of 31 MPa, strain at break of 0.91%, elastic modulus of 3.9 GPa and toughness of 0.11 MPa (**Figure 7.2**c).

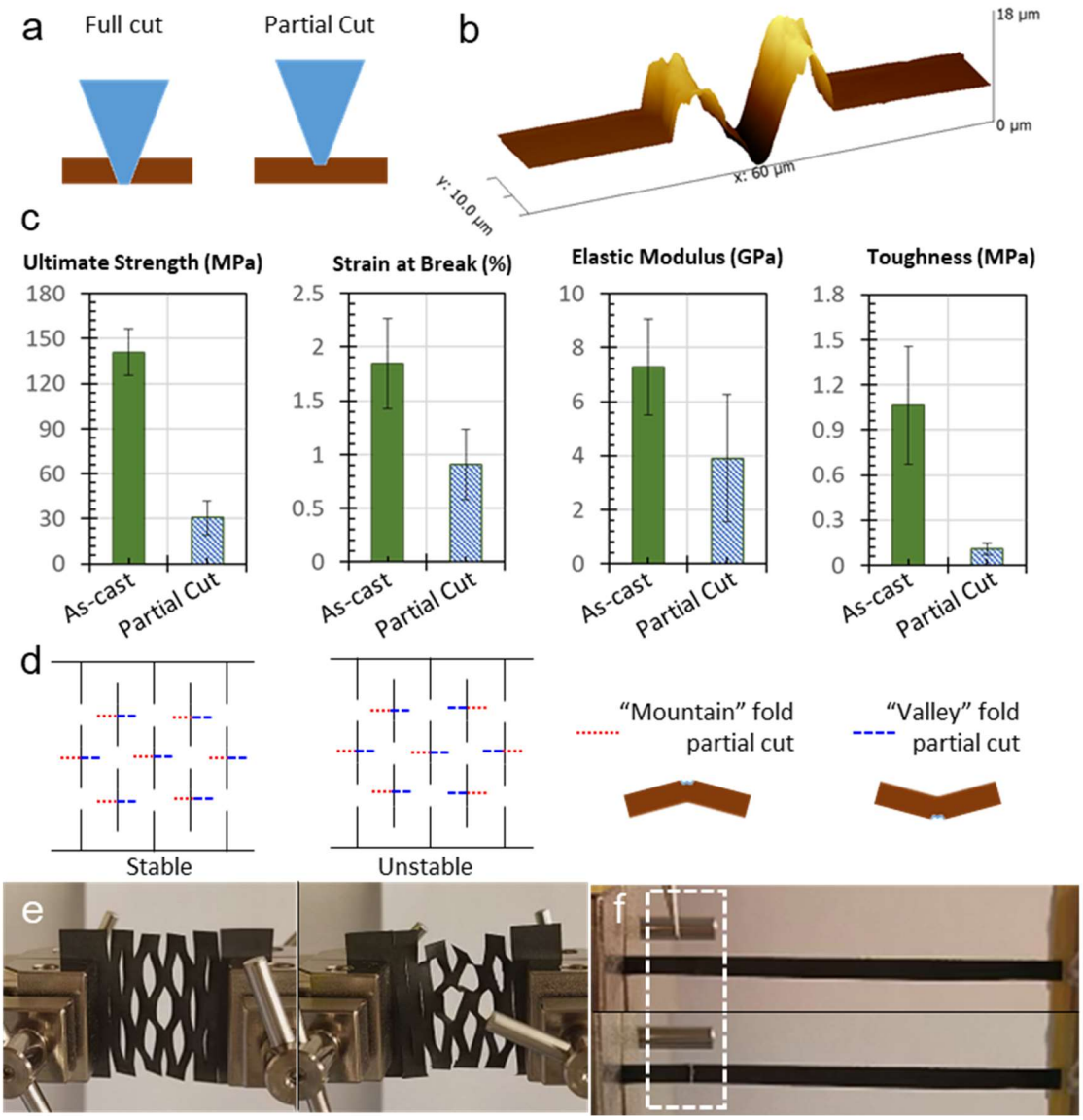

Figure 7.2. a) Drag-knife making full through-cuts, and partial-cuts in GO-SF biopapers. b) Scanning electron micrograph GO-SF biopaper with partial-cuts (scale bar 50µm) tilted at 30°. c) Mechanical properties of GO-SF coupons (20 x 4 x 0.04 mm) both as-cast (green, solid), and with a single partial cut (blue, dashed) with 10 µm blade extension placed perpendicular to axis of tension. d) Schematic showing mountain (M) and valley (V) cuts in 1D stretch pattern with stable (-MV-MV-) and unstable (-MV-VM-) partial cuts. e) Tensile test of standard 1D stretch pattern with stable (left, -MV-MV-) and unstable (right, -MV-VM-) partial cuts. f) Pre-defined weak points for crack propagation via partial cuts, before (top), and after (bottom) application of 2% strain.

The capacity to make *partial cuts* with a controlled depth through substrate material and controlled stress-strain properties (**Figure 7.2**a, c). We invoke these unique cuts for two

demonstrations: the facilitation of directional buckling, and for introducing points for controlled material failure. As known, a typical cut pattern for producing uniaxial stretching is a series of parallel slits that are aligned perpendicular to the direction of stretching.[306] As the material is stretched, macroscopic deformations are allowed through the buckling of slit flaps out-of-plane. For a flat film patterned with through cuts in this parallel slit arrangement, the direction the slit flap initiates buckling to accommodate macroscopic strain is random, arriving at its lowest energy state through geometric frustration in processes whose resultant structures are difficult to predict.[320] Incorporation of the partial cuts suggested here introduces a preferential direction for buckling. By torque equilibrium, a partial cut would induce buckling in the opposing direction. A partial cut from the top surface would result in preferential "mountain" (M) folding, while a partial cut from the bottom surface would result in preferential "valley" (V) folding (**Figure 7.2**d).

Using two cut motifs introduced above, we designed mountain and valley folds through the strategic placement of partial cuts on the top and bottom side of the GO-SF biopaper. By positioning M-partial cuts always to one side of V-partial cuts (MV-MV- etc.), we can controllably generate a stable arrangement where all the slit-flaps are buckling in the same direction (**Figure 7.2**d,e left). By switching the order in the middle of the kirigami structure (MV-MV-VM-VM), we can create a defined unstable arrangement where the slit-flaps are buckling in opposing directions (**Figure 7.2**d,e right). Parallel slit sheets with the corresponding partial cuts to produce the stable and unstable slit flap arrangements.

The positioning of partial cuts can also define loci of mechanical failure. **Figure 7.2**f shows a representative GO-SF biopaper coupon before (top in figure) and after (bottom)

an applied 2% strain. The tweezer tip points toward the position of the partial cut in the sample before applied strain corresponding well with the position of the emerged crack after applied strain. Finally, controllable placing through partial cuts predetermine the crack position and propagation.

7.3.3 Converting drag-knife cut biopapers into highly conductive substrates.

By using a previously described technique of anodic metal-assisted reduction,[265] we convert the GO-SF biopaper from insulating GO to highly-conductive reduced graphene oxide (rGO)—increasing the conductivity by six orders of magnitude up to $1.2*10^4$ S/m at ambient conditions.[64,321] Regions of the GO-SF that undergone reduction could be seen by visual inspection, changing from black in color and dull in luster, to grey and shiny. The changes in the visual appearance, spectroscopic properties, and electronic properties confirm the chemical conversion of the GO-SF biopaper (**Figure 7.3**). We note by XPS that metal-assisted reduction significantly increases the C-to-O atomic ratio in the biopaper from 2.4 to 3.6, and produces a commensurate shift in carbon chemical state away from lower oxygen-containing moieties (such as C-OH and CO_2H centered at 286 eV) to non-oxygenated moieties (such as C-C and C=C, centered at 284.5eV), matching observations in GO reduction by hydrazine or ascorbic acid.[321]

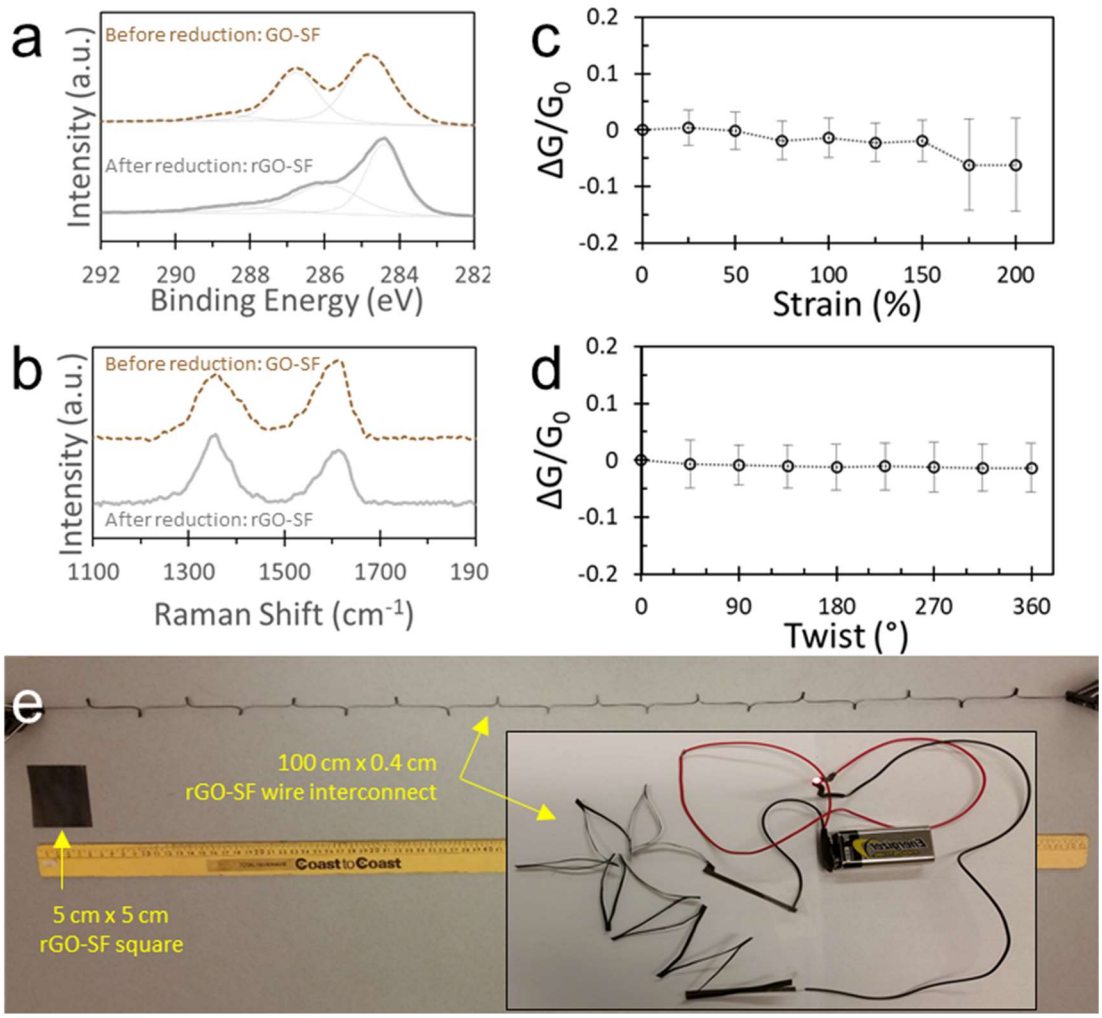

Figure 7.3. a) XPS and b) Raman spectra confirming conversion of GO material to rGO. Conductance averaged aross multiple samples to c) applied strain, and d) twist for the standard 1D stretch coupon. e) Reduced GO-SF sheet cut by drag-knife kirigami to form long conductive trace that can act as flexible, wire-type interconnect. Inset shows rGO-SF wire retains conductivity.

Raman spectroscopy also shows characteristic increase in D-band (centered at 1350 cm^{-1}) to G-band (centered at 1600 cm^{-1}) areal ratio from 0.90 to 1.19, and sharpening of the D-band peak, associated with the reduction of GO.[292,321] Changing the extent of reduction (through longer reduction time, or more reduction cycles), do not show impact to cut-patterns and mechanical performance. The GO-SF biopapers cut with a 1D stretch pattern ("A1" patterned cut), show remarkable invariance of conductance in response to

mechanical agitation such as stretching up to 150% and twisting by up to 360° (**Figure 7.3**c). These observations showcase the robustness of drag-knife patterned GO-SF biopapers as a platform for circuitry for non-rigid use cases.

7.3.4 Assembling kirigami biopaper into highly stretchable energy harvesters.

Finally, the cut-patterned rGO-SF biopaper was assembled as a stretchable, touch-activated energy harvester (**Figure 7.4**a). Conventional single-electrode energy harvesters are constructed from a metal (Cu, Al) surface supported on a surface.[322,323] Due to the difference in electron affinity between the rGO-SF energy harvester and a contacting surface, such as the skin surface of human fingertips, will produce a charge transfer upon contact and release due to through simultaneous processes of contact electrification and electrostatic induction.[259]

We observed that for the rGO-SF device fabricated here, a keystroke touch by a human index finger produces an open-circuit voltage (V_{OC}) and short-circuit current (I_{SC}) of approximately 40 V and 15 nA respectively (**Figure 7.4**b). This device operates as a single-electrode triboelectric nanogenerator, where the rGO-SF biopaper acts as the electrode and the PDMS encapsulation layer as one triboelectric material.[324,325] Human skin or other contact surface works as the other triboelectric material.[326,327]

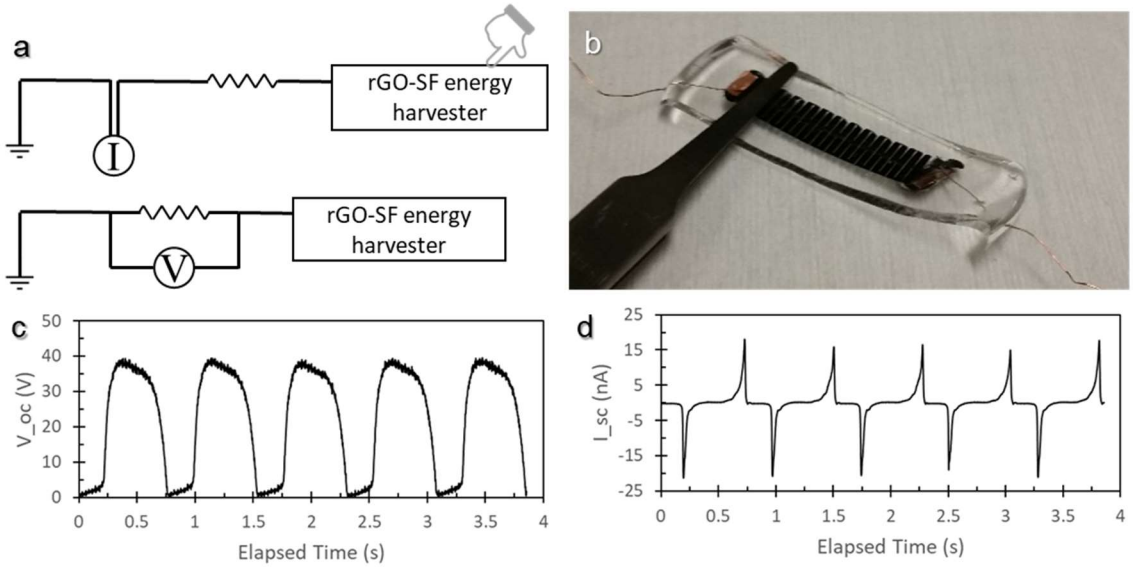

Figure 7.4. a) rGO-SF triboelectric energy harvester in open-circuit and short-circuit configurations for measure current and voltage. b) Assembled rGO-SF energy harvester packaged with Cu tape and Cu wire current collectors. c) Voltage and d) current outputs from tapping by finger the stretchable rGO-SF energy harvester.

When a tapping finger touches the device, positive and negative triboelectric charges will be induced on the surfaces of the skin and PDMS, respectively, due to contact electrification. When the finger leaves the device, the negative charges on PDMS will generate a negative potential on the rGO-SF biopaper due to electrostatic induction and drive electrons to flow from the rGO-SF biopaper to the ground electrode, inducing an electrical current flowing in the other direction. As the skin reapproaches the device, electrons will flow back to the biopaper and induce a current in the opposite direction. When the skin stays on or at a constant distance to the device, the open-circuit output voltage will remain relatively stable, corresponding to the close-to-zero values and the high plateau respectively, and the short-circuit current will stay as zero. As the gap distance between the skin and device changes, the change in voltage and current pulses are observed. Compared to conventional mechanical energy harvesting devices based on electromagnetic

or piezoelectric generator, this single-electrode device has the unique advantage of being highly stretchable. Its flexibility also enables facile application on wide range of objects and generate electricity with almost any moving object.

7.4 Conclusions

In conclusion, we demonstrated large-scale drag-knife kirigami graphene biopapers that are highly stretchable, mechanically robust, conductive, and capable of dramatic shape transformation under strain. The key to enabling the smooth cutting of the strong, tough biopaper is a water-vapor pretreatment that can induce the controlled plasticization resulting in a transient soft, drag-knife processible material. We suggest that this technique can extend across the gamut of hydrogen-bonded biomaterials, and especially useful for transforming superior nano- and micro-structured bionanocomposites into functional meso- and human-scale 2D and 3D form factors.

A crucial advantage of drag-knife kirigami approach demonstrated here is the capacity to reliably generate full and partial-cut patterns that we leverage into generation 1) loci for controlled material failure, 2) loci for preferential creasing, and 3) control over folding direction. As the fundamentals and applications of kirigami are further explored, we believe these added capabilities will be critical in the facile and controllable generation of new kirigami structures including in novel materials with shape transformation.

Furthermore, we show that the generation of conductive microtraces in GO-SF biopapers through controlled reduction can be done in tandem and affords orthogonal control over

generated electronic properties. Drag-knife kirigami increases strain tolerance in the bionanocomposite system that has otherwise low strain-at-break, while patterned reduction generates a conductive network of microtraces. Combining the two processing techniques produces the stretchable triboelectric nanogenerator in a robust bionanocomposite paper. This GO-SF nanogenerator is mechanically reconfigurable, and can be extended into the wide array of 1D stretchable, 2D auxetic, and 3D pop-up geometries.

In summary, we have shown that a combination of water-vapor annealing and drag-knife kirigami opens a route toward the generation of a diverse array of stretchable and pop-up structures in a GO-SF nanocomposite biopaper. Through a novel design motif of partial cuts, we demonstrate unprecedented control over directional buckling for 3D shape changing structures and pre-programmed failure position in stretchable biopaper systems. The facile and robust generation of full or partial cut patterns will expand the gamut of new structures accessible by the art of kirigami and origami. By combining the versatile human-scale pop-up and stretchable structures generated in GO biopaper, with the capacity of GO to undergo reduction to yield highly conductive rGO, we showcase GO-SF as a prospective platform for next-generation soft electronics as flexible interconnects, and stretchable energy harvesters.

CHAPTER 8. Discussion / Conclusion

8.1 General Conclusions

This work advances the understanding of how precise, patterned changes to morphology and surface chemistry occurring at the micro- length scale in layered bionanocomposites can give rise to emergent material properties. While recent research trends have seen the proliferation of layered composites comprised of 1D and 2D, bio-derived and active-synthetic components, the obsession on purely focusing on materials assembly to elevate specific material properties such as strength and toughness may miss a host of prospective applications for newly developed bionanocomposites.

Through the application of a small set of facile, orthogonal post-processing that is applied to graphene-silk biopapers, we engineer the localized mechanical strains, molecular-scale component interactions, and surface presence of functional groups. These directed modifications create new properties based in flexible, robust bionanocomposite papers such as increased conductivity, stretchability, energy storage capacity, energy harvesting capacity, and mechanical property tuning (**Figure 8.1**).

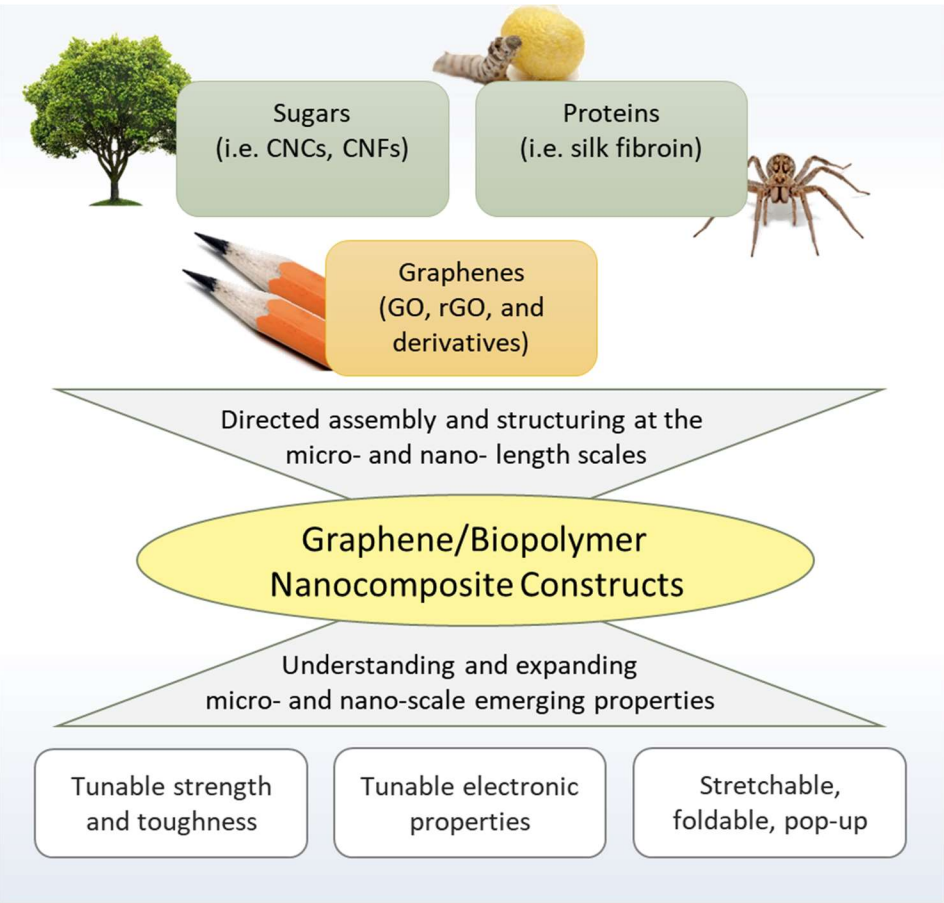

Figure 8.1. Summary of approach of this dissertation toward understanding and expanding new material properties arising from the directed microstructural processing of layered graphene-biopolymer bionanocomposites.

We showcase that post-processing transformation of bionanocomposites include the transformation of protein secondary structure to induce mechanical property enhancement; localization of chemical reduction to generate flexible resistive humidity sensors, capacitive haptic sensors, and wafer-scale arrays of electric double-layer capacitors; and the localization of geometrical voids to create programmable points of fracture and complex, yet algorithmic buckling, which can transform large-area dragknife-cut biopapers into a platform for 3D pop-up electronics.

First, we describe the post-processing transformation of graphene-silk by a facile water-vapor annealing step. Temperature-controlled water vapor annealing initiates the β-sheet transformation of the SF protein binder along hydrophobic regions in GO basal plane of biopapers. Water vapor acts as a plasticizer, intercalating between GO-SF layers. Extended annealing induces transformation of the unstable SF mesophase into larger 3D β-sheet domains that increase energy of sliding between GO layers. This highly localized SF rearrangement yields a significant increase in ultimate strength, Young's modulus, and toughness by up to 41%, 75% and 45% respectively—among the highest reported strength and toughness for graphene-based nanocomposites. This work helps build an understanding of protein nanocomposites that tune the interaction between components after the initial nanocomposite assembly. Resultant structureas have superior mechanical stability and increased resistance to solvation by solvents, enabling aqueous post-processing without risk of delamination of layered components.

Next, we report the first print-scalable patterned reduction of a GO nanocomposite paper. We found anodic Al particles placed in intimate contact with GO-SF induces a chemical reduction of the underlying layer, increasing biopaper conductivity by 6 orders of magnitude up to 1.5×10^4 S/m (an order of magnitude higher than doped GaAs). Dispersing the Al particles in a thixotropic ink allows the reductant to be localized onto the biopapers with a critical dimension of 70-μm through screen printing mesh. We print arrays of reduced GO-SF features across 400-cm^2, demonstrating this process to generate significantly larger processing volume than previously reported serial reduction techniques such as by laser scribing. Taking advantage of the high electronic conductivity of reduced pathways, and variable ionic conductivity of unreduced GO-SF, we fabricate sensing

elements into GO-SF biopapers including a resistive humidity sensor, and capacitive proximity sensor.

Our work shows using photolithography to guide the placement of e-beam deposited reductant to result in an over two-order of magnitude increase in feature density from previously described screen printing and laser scribing techniques. This novel approach enables the fabrication of even sub-micron (800-μm critical dimension) conductive traces in insulating GO-SF biopaper. The high resolution and high fidelity of localized conductive features enables the generation of wafer-scale arrays of micro-supercapacitors with extremely high capacitance retention in response to flexion (>80% after 20 bending cycles). Conventional active materials for electrochemical capacitors are highly porous to accommodate double layer formation across large areas, but cannot typically accommodate bending stresses due to disruption of brittle porous structure. However, the patterned micro-supercapacitors integrated onto the surface of GO-SF biopapers is a new paradigm for designing ultrathin capacitors that support charge across micro-scale roughness generated across thin reduced surface. This allows for the relatively high capacitance, and the superior capacitance retention despite repeated mechanical agitation.

Finally, we invoke our knowledge of water-vapor effect on biopapers for the controlled placement of voids into GO-SF biopapers through numerical controlled dragknife cuts. Pursuing this design strategy allows the first time the generation of simultaneous microscale areal- and height- controlled cuts in layered bionanocomposites. Cuts and partial cuts into a 2D material create controlled points of weakness that enable otherwise strong, tough GO-SF biopapers to flex and stretch without inducing material failure.

Electronic components fabricated into the surface of GO-SF biopapers can adopt the mechanical properties of the underlying biopaper. Such printed GO-SF electronics can stretch and pop-up, yielding complex 3D architectures that can serve as a platform for conformable electronics on interfaces such as textiles or on the human body.

8.2 Significance and broader impact

There is a growing trend of connection between people and devices, such as such a computers, monitors, and control systems. By proxy, the increased integration of information flow between physical objects and human controllers will enable humans to better sense, react, think about, communicate with and control their surroundings—all leading to immediate implications in disparate fields including healthcare, automation, emergency/disaster relief, and telecommunication.

Conventional electronic materials such as metals and semiconductors can form high-performance connections between physical objects and computers in stationary, office-like operating conditions. However, the trend toward pervasive sensing and computing means that more connections will need to be made under non-ideal conditions that is beyond the reach of current material systems. For instance, this could be on the curved surface of farm products, on the flexible surface of clothing, on the stretchable surface of skin, along sterile lining within body tissues.

The research presented in this dissertation signifies a thrust toward a new class of materials, layered bionanocomposites, as prospective materials for non-rigid human-centered

electronics. Fine control over material properties via micro-scale localization of structure and chemistry reveals new properties for biopapers to be used for the first time in sensing, energy transduction, electrical interconnects.

Through engineering of protein ordering in bionanocomposites, key mechanical properties such as strength, toughness and modulus can be significantly enhanced to ensure material survival under more mechanical agitation. Programmable geometry into bionanocomposites through micropatterned full- and partial- cuts enables an additional route to controlling stress-strain behavior, increasing strain-at-break over a hundred-fold, controlling sheet effective plasticization, while also allow for control over buckling behavior and fracture locale. This unprecedented control over different aspects of bionanocomposite properties will expand the use-cases for these materials for diverse mechanical property requirements both on the macroscopic and microscopic scales.

Engineering stress-strain behavior of materials at the single-molecule or intermolecular assembly level often requires serendipitous, experiment-driven studies due to component-specific interactions. However, the techniques employed in the study and transformation of the graphene-silk material system here can be applied more generally across bionanocomposite systems with micro-patterned geometry and chemistry.

Applications for the work presented here extends beyond the realm of flexible electronics. The unusual properties of patterned bionanocomposites are attractive for a host of biomedical applications. Micropatterned voids and partial cuts into planar-fabricated bionanocomposites create softness that increase interfacing with various body tissues. Micropatterned chemistries can direct cell and biomarker adhesion, for instance in

controlling directional cell growth, and in sensing circuits where electrodes have targeting agents with preferential binding for species of interest. Differential extents of reduction GOs also produces anti-biofouling properties in otherwise highly biocompatible GOs. Manipulation of layered bionanocomposites at the sub-few micron size scale can also produce changes to as stretchable gratings and as coated dyes.

Finally, the micro-patterns investigated in this work are rudimentary in design (1D rectangular cut patterns, interdigitated circuits). However, advances in physics is still producing new insights on how controlled geometry at the micro-scale can induce new modes of material deformation; and still discovering new electrode and antenna architectures for optimized ion intercalation and EM wave transfer respectively. Real systems may also require compensation from ideal system designs. Proximity corrections, over-correction and under-corrections may be necessary in micro-patterned cuts and surface chemistries to enforce desired properties. In all these cases, the directed processing approaches presented here can be modified to adapt to these new discoveries, unlike bottom-up approaches that rely upon difficult to predict assembly processes and would require a complete rework to realize *de novo* designs.

Despite the impressive properties of soft components such as 2D molecular flakes (i.e. graphenes), and 1D biopolymers (i.e. silk), it is their combination into layered composites (i.e. graphene-silk biopapers) that produce the synergistic strengthening, toughening for desirable mechanics in flexible applications—far beyond what corresponding strategies can achieve in adding non-rigidity into hard material such as metals (i.e. Au, Cu) and semiconductors (i.e. Si, GaAs). However, in terms of material performance, layered

bionanocomposites cannot yet match in device performance—only achieving competitive properties in niche areas such as high capacitance due to graphene's high surface area. We expect that further research into the conversion of these soft composite components, or the assembly with dispersible active materials to contribute new properties or elevate performance in existing uses. For instance, we introduced the modification of graphene oxide and silk components through doping and attachment of pendant groups. Additionally, we suggest that integrating high aspect ratio metal nanoparticles can produce synergistic light-harnessing effects for high-performance photothermal materials, and integrating transition metal oxides to allow for pseudocapacitive contributions to material capacitance.

As the need for flexible, soft, stretchable device components build, we also expect the establishment of testing standards that will help drive the exploration of non-rigid device components. New use-cases, testing standards, and advances in analogous technologies (i.e. improved photolithography techniques from semiconductor industry, screen printing from solar cell industry) will also increase the utilize of the bionanocomposite material systems investigated here. These open opportunities make layered bionanocomposites a promising material system for use in the future as both structural materials and as device components.

Research Dissemination

This work has been conveyed to the scientific community through the following publications, presentations, and inventions:

Relevant Publications:

(1) Ma, R.; Gordon, D.A.; Yushin, G.; Tsukruk, V. V. Resist Stenciling for Sub-Micron Conductive Traces in Graphene-Silk Biopapers. **2018**. *Submitted.*

(2) Ma, R.; Wu. C.; Wang, Z.L.; Tsukruk, V. V. Graphene-Silk Biopapers by Controlled Drag-Knife Kirigami for Pop-Up Microcircuits. **2018**. *Submitted.*

(3) Xiong, R.; Grant, A. M.; Ma, R.; Zhang, S.; Tsukruk, V. V. Naturally-Derived Biopolymer Nanocomposites: Interfacial Design, Properties and Emerging Applications. *Mater. Sci. Eng. R Rep.* **2018**, *125*, 1–41.

(4) Savchak, M.; Borodinov, N.; Burtovyy, R.; Anayee, M.; Hu, K.; Ma, R.; Grant, A.; Li, H.; Cutshall, D. B.; Wen, Y.; et al. Highly Conductive and Transparent Reduced Graphene Oxide Nanoscale Films via Thermal Conversion of Polymer-Encapsulated Graphene Oxide Sheets. *ACS Appl. Mater. Interfaces* **2018**, *10* (4), 3975–3985.

(5) Borodinov, N.; Gil, D.; Savchak, M.; Gross, C. E.; Yadavalli, N. S.; Ma, R.; Tsukruk, V. V.; Minko, S.; Vertegel, A.; Luzinov, I. En Route to Practicality of the Polymer Grafting Technology: One-Step Interfacial Modification with Amphiphilic Molecular Brushes. *ACS Appl. Mater. Interfaces* **2018**, *10* (16), 13941–13952.

(6) Ma, R.; Tsukruk, V. V. Seriography-Guided Reduction of Graphene Oxide Biopapers for Wearable Sensory Electronics. *Adv. Funct. Mater.* **2017**, *27* (10), 1604802.

(7) Kim, S.; Geryak, R. D.; Zhang, S.; Ma, R.; Calabrese, R.; Kaplan, D. L.; Tsukruk, V. V. Interfacial Shear Strength and Adhesive Behavior of Silk Ionomer Surfaces. *Biomacromolecules* **2017**, *18* (9), 2876–2886.

(8) Smith, M. J.; Malak, S. T.; Jung, J.; Yoon, Y. J.; Lin, C. H.; Kim, S.; Lee, K. M.; Ma, R.; White, T. J.; Bunning, T. J.; et al. Robust, Uniform, and Highly Emissive Quantum Dot–Polymer Films and Patterns Using Thiol–Ene Chemistry. *ACS Appl. Mater. Interfaces* **2017**, *9* (20), 17435–17448.

(9) Xiong, R.; Kim, H. S.; Zhang, S.; Kim, S.; Korolovych, V. F.; Ma, R.; Yingling, Y. G.; Lu, C.; Tsukruk, V. V. Template-Guided Assembly of Silk Fibroin on Cellulose Nanofibers for Robust Nanostructures with Ultrafast Water Transport. *ACS Nano* **2017**, *11* (12), 12008–12019.

(10) Xiong, R.; Hu, K.; Grant, A. M.; Ma, R.; Xu, W.; Lu, C.; Zhang, X.; Tsukruk, V. V. Ultrarobust Transparent Cellulose Nanocrystal-Graphene Membranes with High Electrical Conductivity. *Adv. Mater.* **2016**, *28* (7), 1501–1509.

(11) Wang, Y.; Ma, R.; Hu, K.; Kim, S.; Fang, G.; Shao, Z.; Tsukruk, V. V. Dramatic Enhancement of Graphene Oxide/Silk Nanocomposite Membranes: Increasing Toughness, Strength, and Young's Modulus via Annealing of Interfacial Structures. *ACS Appl. Mater. Interfaces* **2016**, *8* (37), 24962–24973.

Relevant Inventions:

(1) Ma, R., Tsukruk, V. V., *Screen printing generation of microcircuits in graphene-based composites and textiles*. US Appl., 62/436,228, filed Dec 2016.
(2) Ma, R., Tsukruk, V. V., *Photolithography-guided reduction of microtraces in graphene-based composites and textiles*. GTRC Invention Disclosure 7933, filed June 2018.
(3) Ma, R., Tsukruk, V. V., *Programmable drag-knife for generation of cut patterns in graphene-based composites.* GTRC Invention Disclosure 7935, filed June 2018.

Relevant Presentations:

(1) *Ubiquitous Sensing on Strong, Tough GO-SF Composites.* Presented at Institute for Electronics and Nanotechnology Technical Exchange Conference, Atlanta GA. **2018.**
(2) *Origami and Kirigami for Flexible and Stretchable Silk-Graphene Sensory Circuits.* Poster presented at Solvay MSE Poster Symposium, Atlanta GA. **2017.** (best in show award, 1st in division)
(3) *Fabrication of Conductive Microtraces in Bionanocomposite Papers.* Presented at Georgia Tech Soft Matter Symposium, Atlanta GA. **2017.**
(4) *Position Sensory Electronics Printed on Graphene Biopapers.* Poster presented at Georgia Tech/Industry Technical Exchange Forum, Atlanta GA. **2017.**
(5) *Screen Printed Circuits on Strong, Tough GO-SF Composites.* Presented at Georgia Tech User Science and Engineering Review, Atlanta GA. **2016.**
(6) *Micropatterned Reduction of Graphene Oxide Papers.* Poster presented at Georgia Tech Polymer Network. **2016.** (best in show award)
(7) *Flexible Sensors in Silk Fibroin-Graphene Oxide Biocomposite Papers*. Poster presented at Solvay MSE Poster Symposium, Atlanta GA. **2016.** (1st in division)
(8) *Integrated Supercapacitors Fabricated in Bio-Inspired Graphene Oxide-Silk Fibroin Nanocomposites*. Presented at Materials Research Society Fall Meeting and Exhibit, Boston MA. **2015.**
(9) *Highly Conductive Pathways in Graphene Oxide Biopaper*. Presented at Materials Research Society Fall Meeting and Exhibit, Boston MA. **2015.**

References

(1) Wagner, H. D. Nanocomposites: Paving the Way to Stronger Materials. *Nat. Nanotechnol.* **2007**, *2* (12), 742–744.

(2) Marcus, R. K.; Baeumner, A. J. Fiber-Based Platforms for Bioanalytics. *Anal. Bioanal. Chem.* **2016**, *408* (5), 1281–1283.

(3) Zhang, M.; Wang, Y.; Huang, L.; Xu, Z.; Li, C.; Shi, G. Multifunctional Pristine Chemically Modified Graphene Films as Strong as Stainless Steel. *Adv. Mater.* **2015**, n/a-n/a.

(4) Wan, S.; Li, Y.; Peng, J.; Hu, H.; Cheng, Q.; Jiang, L. Synergistic Toughening of Graphene Oxide–Molybdenum Disulfide–Thermoplastic Polyurethane Ternary Artificial Nacre. *ACS Nano* **2015**, *9* (1), 708–714.

(5) Xiong, Z.; Liao, C.; Han, W.; Wang, X. Mechanically Tough Large-Area Hierarchical Porous Graphene Films for High-Performance Flexible Supercapacitor Applications. *Adv. Mater.* **2015**, *27* (30), 4469–4475.

(6) Liu, P.; Jin, Z.; Katsukis, G.; Drahushuk, L. W.; Shimizu, S.; Shih, C.-J.; Wetzel, E. D.; Taggart-Scarff, J. K.; Qing, B.; Vliet, K. J. V.; et al. Layered and Scrolled Nanocomposites with Aligned Semi-Infinite Graphene Inclusions at the Platelet Limit. *Science* **2016**, *353* (6297), 364–367.

(7) Wan, S.; Peng, J.; Li, Y.; Hu, H.; Jiang, L.; Cheng, Q. Use of Synergistic Interactions to Fabricate Strong, Tough, and Conductive Artificial Nacre Based on Graphene Oxide and Chitosan. *ACS Nano* **2015**, *9* (10), 9830–9836.

(8) Chen, K.; Shi, B.; Yue, Y.; Qi, J.; Guo, L. Binary Synergy Strengthening and Toughening of Bio-Inspired Nacre-like Graphene Oxide/Sodium Alginate Composite Paper. *ACS Nano* **2015**, *9* (8), 8165–8175.

(9) Wang, Y.; Ma, R.; Hu, K.; Kim, S.; Fang, G.; Shao, Z.; Tsukruk, V. V. Dramatic Enhancement of Graphene Oxide/Silk Nanocomposite Membranes: Increasing Toughness and Strength via Annealing of Interfacial Structures. *ACS Appl. Mater. Interfaces* **2016**.

(10) Tokarev, I.; Tokareva, I.; Minko, S. Gold-Nanoparticle-Enhanced Plasmonic Effects in a Responsive Polymer Gel. *Adv. Mater.* **2008**, *20* (14), 2730–2734.

(11) Jiang, C.; Markutsya, S.; Pikus, Y.; Tsukruk, V. V. Freely Suspended Nanocomposite Membranes as Highly Sensitive Sensors. *Nat. Mater.* **2004**, *3* (10), 721–728.

(12) Luzinov, I.; Minko, S.; Tsukruk, V. V. Adaptive and Responsive Surfaces through Controlled Reorganization of Interfacial Polymer Layers. *Prog. Polym. Sci.* **2004**, *29* (7), 635–698.

(13) Jung, Y. H.; Chang, T.-H.; Zhang, H.; Yao, C.; Zheng, Q.; Yang, V. W.; Mi, H.; Kim, M.; Cho, S. J.; Park, D.-W.; et al. High-Performance Green Flexible Electronics Based on Biodegradable Cellulose Nanofibril Paper. *Nat. Commun.* **2015**, *6*, 7170.

(14) Sydney Gladman, A.; Matsumoto, E. A.; Nuzzo, R. G.; Mahadevan, L.; Lewis, J. A. Biomimetic 4D Printing. *Nat. Mater.* **2016**, *15* (4), 413–418.

(15) Tao, H.; Marelli, B.; Yang, M.; An, B.; Onses, M. S.; Rogers, J. A.; Kaplan, D. L.; Omenetto, F. G. Inkjet Printing of Regenerated Silk Fibroin: From Printable Forms to Printable Functions. *Adv. Mater.* **2015**, *27* (29), 4273–4279.

(16) Kim, S.; Marelli, B.; Brenckle, M. A.; Mitropoulos, A. N.; Gil, E.-S.; Tsioris, K.; Tao, H.; Kaplan, D. L.; Omenetto, F. G. All-Water-Based Electron-Beam Lithography Using Silk as a Resist. *Nat. Nanotechnol.* **2014**, *9* (4), 306–310.

(17) Barthelat, F.; Yin, Z.; Buehler, M. J. Structure and Mechanics of Interfaces in Biological Materials. *Nat. Rev. Mater.* **2016**, *1*, 16007.

(18) Hu, K.; Kulkarni, D. D.; Choi, I.; Tsukruk, V. V. Graphene-Polymer Nanocomposites for Structural and Functional Applications. *Prog. Polym. Sci.* **2014**, *39* (11), 1934–1972.

(19) Xiong, R.; Grant, A. M.; Ma, R.; Zhang, S.; Tsukruk, V. V. Naturally-Derived Biopolymer Nanocomposites: Interfacial Design, Properties and Emerging Applications. *Mater. Sci. Eng. R Rep.* **2018**, *125*, 1–41.

(20) Waldrop, M. M. The Chips Are down for Moore's Law. *Nat. News* **2016**, *530* (7589), 144.

(21) Li, T.; Mastro, M.; Dadgar, A. *III–V Compound Semiconductors: Integration with Silicon-Based Microelectronics*; CRC Press, 2010.

(22) Tummala, R. R.; Rymaszewski, E. J.; Klopfenstein, A. G. *Microelectronics Packaging Handbook: Technology Drivers*; Springer Science & Business Media, 2012.

(23) Majidi, C. Soft Robotics: A Perspective—Current Trends and Prospects for the Future. *Soft Robot.* **2013**, *1* (1), 5–11.

(24) Suo, Z.; Ma, E. Y.; Gleskova, H.; Wagner, S. Mechanics of Rollable and Foldable Film-on-Foil Electronics. *Appl. Phys. Lett.* **1999**, *74* (8), 1177–1179.

(25) Wang, Z. L.; Gao, R. P.; Pan, Z. W.; Dai, Z. R. Nano-Scale Mechanics of Nanotubes, Nanowires, and Nanobelts. *Adv. Eng. Mater.* **2001**, *3* (9), 657.

(26) Espinosa, H. D.; Bernal, R. A.; Minary-Jolandan, M. A Review of Mechanical and Electromechanical Properties of Piezoelectric Nanowires. *Adv. Mater.* **2012**, *24* (34), 4656–4675.

(27) Calahorra, Y.; Shtempluck, O.; Kotchetkov, V.; Yaish, Y. E. Young's Modulus, Residual Stress, and Crystal Orientation of Doubly Clamped Silicon Nanowire Beams. *Nano Lett.* **2015**, *15* (5), 2945–2950.

(28) McDowell, M. T.; Leach, A. M.; Gall, K. Bending and Tensile Deformation of Metallic Nanowires. *Model. Simul. Mater. Sci. Eng.* **2008**, *16* (4), 045003.

(29) Cavallo, F.; G. Lagally, M. Semiconductors Turn Soft: Inorganic Nanomembranes. *Soft Matter* **2010**, *6* (3), 439–455.

(30) Huang, G.; Mei, Y. Thinning and Shaping Solid Films into Functional and Integrative Nanomembranes. *Adv. Mater.* **2012**, *24* (19), 2517–2546.

(31) Kim, D.-H.; Rogers, J. A. Bend, Buckle, and Fold: Mechanical Engineering with Nanomembranes. *ACS Nano* **2009**, *3* (3), 498–501.

(32) Markutsya, S.; Jiang, C.; Pikus, Y.; Tsukruk, V. V. Freely Suspended Layer-by-Layer Nanomembranes: Testing Micromechanical Properties. *Adv. Funct. Mater.* **2005**, *15* (5), 771–780.

(33) Xu, S.; Yan, Z.; Jang, K.-I.; Huang, W.; Fu, H.; Kim, J.; Wei, Z.; Flavin, M.; McCracken, J.; Wang, R.; et al. Assembly of Micro/Nanomaterials into Complex, Three-Dimensional Architectures by Compressive Buckling. *Science* **2015**, *347* (6218), 154–159.

(34) Kim, D.-H.; Ahn, J.-H.; Choi, W. M.; Kim, H.-S.; Kim, T.-H.; Song, J.; Huang, Y. Y.; Liu, Z.; Lu, C.; Rogers, J. A. Stretchable and Foldable Silicon Integrated Circuits. *Science* **2008**, *320* (5875), 507–511.

(35) Kang, S.-K.; Murphy, R. K. J.; Hwang, S.-W.; Lee, S. M.; Harburg, D. V.; Krueger, N. A.; Shin, J.; Gamble, P.; Cheng, H.; Yu, S.; et al. Bioresorbable Silicon Electronic Sensors for the Brain. *Nature* **2016**, *530* (7588), 71–76.

(36) Jang, K.-I.; Li, K.; Chung, H. U.; Xu, S.; Jung, H. N.; Yang, Y.; Kwak, J. W.; Jung, H. H.; Song, J.; Yang, C.; et al. Self-Assembled Three Dimensional Network Designs for Soft Electronics. *Nat. Commun.* **2017**, *8*, 15894.

(37) Kim, B. H.; Lee, J.; Won, S. M.; Xie, Z.; Chang, J.-K.; Yu, Y.; Cho, Y. K.; Jang, H.; Jeong, J. Y.; Lee, Y.; et al. Three-Dimensional Silicon Electronic Systems Fabricated by Compressive Buckling Process. *ACS Nano* **2018**.

(38) Norton, J. J. S.; Lee, D. S.; Lee, J. W.; Lee, W.; Kwon, O.; Won, P.; Jung, S.-Y.; Cheng, H.; Jeong, J.-W.; Akce, A.; et al. Soft, Curved Electrode Systems Capable of Integration on the Auricle as a Persistent Brain–Computer Interface. *Proc. Natl. Acad. Sci.* **2015**, *112* (13), 3920–3925.

(39) Chen, B. G.; Liu, B.; Evans, A. A.; Paulose, J.; Cohen, I.; Vitelli, V.; Santangelo, C. D. Topological Mechanics of Origami and Kirigami. *Phys. Rev. Lett.* **2016**, *116* (13), 135501.

(40) Sussman, D. M.; Cho, Y.; Castle, T.; Gong, X.; Jung, E.; Yang, S.; Kamien, R. D. Algorithmic Lattice Kirigami: A Route to Pluripotent Materials. *Proc. Natl. Acad. Sci.* **2015**, *112* (24), 7449–7453.

(41) Rafsanjani, A.; Bertoldi, K. Buckling-Induced Kirigami. *Phys. Rev. Lett.* **2017**, *118* (8), 084301.

(42) Callens, S. J. P.; Zadpoor, A. A. From Flat Sheets to Curved Geometries: Origami and Kirigami Approaches. *Mater. Today* **2018**, *21* (3), 241–264.

(43) Shyu, T. C.; Damasceno, P. F.; Dodd, P. M.; Lamoureux, A.; Xu, L.; Shlian, M.; Shtein, M.; Glotzer, S. C.; Kotov, N. A. A Kirigami Approach to Engineering Elasticity in Nanocomposites through Patterned Defects. *Nat. Mater.* **2015**, *14* (8), 785–789.

(44) Xu, W.; Qin, Z.; Chen, C.-T.; Kwag, H. R.; Ma, Q.; Sarkar, A.; Buehler, M. J.; Gracias, D. H. Ultrathin Thermoresponsive Self-Folding 3D Graphene. *Sci. Adv.* **2017**, *3* (10), e1701084.

(45) Neville, R. M.; Scarpa, F.; Pirrera, A. Shape Morphing Kirigami Mechanical Metamaterials. *Sci. Rep.* **2016**, *6*, 31067.

(46) Xu, L.; Wang, X.; Kim, Y.; Shyu, T. C.; Lyu, J.; Kotov, N. A. Kirigami Nanocomposites as Wide-Angle Diffraction Gratings. *ACS Nano* **2016**, *10* (6), 6156–6162.

(47) Lamoureux, A.; Lee, K.; Shlian, M.; Forrest, S. R.; Shtein, M. Dynamic Kirigami Structures for Integrated Solar Tracking. *Nat. Commun.* **2015**, *6*, 8092.

(48) Lipomi, D. J.; Bao, Z. Stretchable and Ultraflexible Organic Electronics. *MRS Bull.* **2017**, *42* (2), 93–97.

(49) Amjadi, M.; Kyung, K.-U.; Park, I.; Sitti, M. Stretchable, Skin-Mountable, and Wearable Strain Sensors and Their Potential Applications: A Review. *Adv. Funct. Mater.* **2016**, *26* (11), 1678–1698.

(50) Chen, Z.; Xi, J.; Huang, W.; Yuen, M. M. F. Stretchable Conductive Elastomer for Wireless Wearable Communication Applications. *Sci. Rep.* **2017**, *7* (1), 10958.

(51) Park, M.; Park, J.; Jeong, U. Design of Conductive Composite Elastomers for Stretchable Electronics. *Nano Today* **2014**, *9* (2), 244–260.

(52) Moon, G. D.; Lim, G.-H.; Song, J. H.; Shin, M.; Yu, T.; Lim, B.; Jeong, U. Highly Stretchable Patterned Gold Electrodes Made of Au Nanosheets. *Adv. Mater.* **2013**, *25* (19), 2707–2712.

(53) Lee, S.; Shin, S.; Lee, S.; Seo, J.; Lee, J.; Son, S.; Cho, H. J.; Algadi, H.; Al-Sayari, S.; Kim, D. E.; et al. Ag Nanowire Reinforced Highly Stretchable Conductive Fibers for Wearable Electronics. *Adv. Funct. Mater.* **2015**, *25* (21), 3114–3121.

(54) Catenacci, M. J.; Reyes, C.; Cruz, M. A.; Wiley, B. J. Stretchable Conductive Composites from Cu–Ag Nanowire Felt. *ACS Nano* **2018**, *12* (4), 3689–3698.

(55) Kim, B. S.; Shin, K.-Y.; Pyo, J. B.; Lee, J.; Son, J. G.; Lee, S.-S.; Park, J. H. Reversibly Stretchable, Optically Transparent Radio-Frequency Antennas Based on Wavy Ag Nanowire Networks. *ACS Appl. Mater. Interfaces* **2016**, *8* (4), 2582–2590.

(56) Stoyanov, H.; Kollosche, M.; Risse, S.; Waché, R.; Kofod, G. Soft Conductive Elastomer Materials for Stretchable Electronics and Voltage Controlled Artificial Muscles. *Adv. Mater.* **2013**, *25* (4), 578–583.

(57) Choong, C.-L.; Shim, M.-B.; Lee, B.-S.; Jeon, S.; Ko, D.-S.; Kang, T.-H.; Bae, J.; Lee, S. H.; Byun, K.-E.; Im, J.; et al. Highly Stretchable Resistive Pressure Sensors Using a Conductive Elastomeric Composite on a Micropyramid Array. *Adv. Mater.* **2014**, *26* (21), 3451–3458.

(58) Printz, A. D.; Savagatrup, S.; Burke, D. J.; Purdy, T. N.; Lipomi, D. J. Increased Elasticity of a Low-Bandgap Conjugated Copolymer by Random Segmentation for Mechanically Robust Solar Cells. *RSC Adv.* **2014**, *4* (26), 13635–13643.

(59) Müller, C.; Goffri, S.; Breiby, D. W.; Andreasen, J. W.; Chanzy, H. D.; Janssen, R. a. J.; Nielsen, M. M.; Radano, C. P.; Sirringhaus, H.; Smith, P.; et al. Tough, Semiconducting Polyethylene-Poly(3-Hexylthiophene) Diblock Copolymers. *Adv. Funct. Mater.* **2007**, *17* (15), 2674–2679.

(60) Xu, J.; Wang, S.; Wang, G.-J. N.; Zhu, C.; Luo, S.; Jin, L.; Gu, X.; Chen, S.; Feig, V. R.; To, J. W. F.; et al. Highly Stretchable Polymer Semiconductor Films through the Nanoconfinement Effect. *Science* **2017**, *355* (6320), 59–64.

(61) Oh, J. Y.; Rondeau-Gagné, S.; Chiu, Y.-C.; Chortos, A.; Lissel, F.; Wang, G.-J. N.; Schroeder, B. C.; Kurosawa, T.; Lopez, J.; Katsumata, T.; et al. Intrinsically Stretchable and Healable Semiconducting Polymer for Organic Transistors. *Nature* **2016**, *539* (7629), 411–415.

(62) Wool, R.; Sun, X. S. *Bio-Based Polymers and Composites*; Academic Press, 2011.

(63) Habibi, Y.; Lucia, L. A.; Rojas, O. J. Cellulose Nanocrystals: Chemistry, Self-Assembly, and Applications. *Chem. Rev.* **2010**, *110* (6), 3479–3500.

(64) Dreyer, D. R.; Park, S.; Bielawski, C. W.; Ruoff, R. S. The Chemistry of Graphene Oxide. *Chem. Soc. Rev.* **2010**, *39* (1), 228–240.

(65) Pérez-Rigueiro, J.; Viney, C.; Llorca, J.; Elices, M. Silkworm Silk as an Engineering Material. *J. Appl. Polym. Sci.* **1998**, *70* (12), 2439–2447.

(66) Gosline, J. M.; Guerette, P. A.; Ortlepp, C. S.; Savage, K. N. The Mechanical Design of Spider Silks: From Fibroin Sequence to Mechanical Function. *J. Exp. Biol.* **1999**, *202* (23), 3295–3303.

(67) Shao, Z.; Vollrath, F. Materials: Surprising Strength of Silkworm Silk. *Nature* **2002**, *418* (6899), 741–741.

(68) Jeon, J.-H.; Cheedarala, R. K.; Kee, C.-D.; Oh, I.-K. Dry-Type Artificial Muscles Based on Pendent Sulfonated Chitosan and Functionalized Graphene Oxide for Greatly Enhanced Ionic Interactions and Mechanical Stiffness. *Adv. Funct. Mater.* **2013**, *23* (48), 6007–6018.

(69) Yadav, S. K.; Jung, Y. C.; Kim, J. H.; Ko, Y.-I.; Ryu, H. J.; Yadav, M. K.; Kim, Y. A.; Cho, J. W. Mechanically Robust, Electrically Conductive Biocomposite Films Using Antimicrobial Chitosan-Functionalized Graphenes. *Part. Part. Syst. Charact.* **2013**, *30* (8), 721–727.

(70) Campos, J. M.; Ferraria, A. M.; do Rego, A. M. B.; Ribeiro, M. R.; Barros-Timmons, A. Studies on PLA Grafting onto Graphene Oxide and Its Effect on the Ensuing Composite Films. *Mater. Chem. Phys.* **2015**, *166*, 122–132.

(71) Yang, Q.; Saito, T.; Berglund, L. A.; Isogai, A. Cellulose Nanofibrils Improve the Properties of All-Cellulose Composites by the Nano-Reinforcement Mechanism and Nanofibril-Induced Crystallization. *Nanoscale* **2015**, *7* (42), 17957–17963.

(72) Klemm, D.; Kramer, F.; Moritz, S.; Lindström, T.; Ankerfors, M.; Gray, D.; Dorris, A. Nanocelluloses: A New Family of Nature-Based Materials. *Angew. Chem. Int. Ed.* **2011**, *50* (24), 5438–5466.

(73) Wegst, U. G.; Bai, H.; Saiz, E.; Tomsia, A. P.; Ritchie, R. O. Bioinspired Structural Materials. *Nat. Mater.* **2015**, *14* (1), 23–36.

(74) Iwamoto, S.; Kai, W.; Isogai, A.; Iwata, T. Elastic Modulus of Single Cellulose Microfibrils from Tunicate Measured by Atomic Force Microscopy. *Biomacromolecules* **2009**, *10* (9), 2571–2576.

(75) Xiong, R.; Hu, K.; Grant, A. M.; Ma, R.; Xu, W.; Lu, C.; Zhang, X.; Tsukruk, V. V. Ultrarobust Transparent Cellulose Nanocrystal-Graphene Membranes with High Electrical Conductivity. *Adv. Mater.* **2016**, *28* (7), 1501–1509.

(76) Wicklein, B.; Kocjan, A.; Salazar-Alvarez, G.; Carosio, F.; Camino, G.; Antonietti, M.; Bergström, L. Thermally Insulating and Fire-Retardant Lightweight Anisotropic Foams Based on Nanocellulose and Graphene Oxide. *Nat. Nanotechnol.* **2015**, *10* (3), 277–283.

(77) Zhu, H.; Luo, W.; Ciesielski, P. N.; Fang, Z.; Zhu, J. Y.; Henriksson, G.; Himmel, M. E.; Hu, L.; others. Wood-Derived Materials for Green Electronics, Biological Devices, and Energy Applications. *Chem Rev* **2016**, *116* (16), 9305–9374.

(78) Moon, R. J.; Martini, A.; Nairn, J.; Simonsen, J.; Youngblood, J. Cellulose Nanomaterials Review: Structure, Properties and Nanocomposites. *Chem. Soc. Rev.* **2011**, *40* (7), 3941–3994.

(79) Hummers Jr, W. S.; Offeman, R. E. Preparation of Graphitic Oxide. *J. Am. Chem. Soc.* **1958**, *80* (6), 1339–1339.

(80) Zhu, Y.; Murali, S.; Cai, W.; Li, X.; Suk, J. W.; Potts, J. R.; Ruoff, R. S. Graphene and Graphene Oxide: Synthesis, Properties, and Applications. *Adv. Mater.* **2010**, *22* (35), 3906–3924.

(81) Yoo, B. M.; Shin, H. J.; Yoon, H. W.; Park, H. B. Graphene and Graphene Oxide and Their Uses in Barrier Polymers. *J. Appl. Polym. Sci.* **2014**, *131* (1).

(82) Yang, Y.-H.; Bolling, L.; Priolo, M. A.; Grunlan, J. C. Super Gas Barrier and Selectivity of Graphene Oxide-Polymer Multilayer Thin Films. *Adv. Mater.* **2013**, *25* (4), 503–508.

(83) Yin, Y.; Hu, K.; Grant, A. M.; Zhang, Y.; Tsukruk, V. V. Biopolymeric Nanocomposites with Enhanced Interphases. *Langmuir* **2015**, *31* (39), 10859–10870.

(84) Hu, K.; Gupta, M. K.; Kulkarni, D. D.; Tsukruk, V. V. Ultra-Robust Graphene Oxide-Silk Fibroin Nanocomposite Membranes. *Adv. Mater.* **2013**, *25* (16), 2301–2307.

(85) Atwood, J. L.; Steed, J. W. *Encyclopedia of Supramolecular Chemistry*; CRC Press, 2004; Vol. 1.

(86) Ghosh, A.; Rao, K. V.; George, S. J.; Rao, C. N. R. Noncovalent Functionalization, Exfoliation, and Solubilization of Graphene in Water by Employing a Fluorescent Coronene Carboxylate. *Chem. Eur. J.* **2010**, *16* (9), 2700–2704.

(87) Georgakilas, V.; Otyepka, M.; Bourlinos, A. B.; Chandra, V.; Kim, N.; Kemp, K. C.; Hobza, P.; Zboril, R.; Kim, K. S. Functionalization of Graphene: Covalent and Non-Covalent Approaches, Derivatives and Applications. *Chem. Rev.* **2012**, *112* (11), 6156–6214.

(88) Long, B.; Manning, M.; Burke, M.; Szafranek, B. N.; Visimberga, G.; Thompson, D.; Greer, J. C.; Povey, I. M.; MacHale, J.; Lejosne, G.; et al. Non-Covalent Functionalization of Graphene Using Self-Assembly of Alkane-Amines. *Adv. Funct. Mater.* **2012**, *22* (4), 717–725.

(89) Han, Y.; Xu, Z.; Gao, C. Ultrathin Graphene Nanofiltration Membrane for Water Purification. *Adv. Funct. Mater.* **2013**, *23* (29), 3693–3700.

(90) Xu, H.; Xie, L.; Wu, D.; Hakkarainen, M. Immobilized Graphene Oxide Nanosheets as Thin but Strong Nanointerfaces in Biocomposites. *ACS Sustain. Chem. Eng.* **2016**, *4* (4), 2211–2222.

(91) Uddin, M. E.; Layek, R. K.; Kim, H. Y.; Kim, N. H.; Hui, D.; Lee, J. H. Preparation and Enhanced Mechanical Properties of Non-Covalently-Functionalized Graphene Oxide/Cellulose Acetate Nanocomposites. *Compos. Part B Eng.* **2016**, *90*, 223–231.

(92) Nie, L.; Liu, C.; Wang, J.; Shuai, Y.; Cui, X.; Liu, L. Effects of Surface Functionalized Graphene Oxide on the Behavior of Sodium Alginate. *Carbohydr. Polym.* **2015**, *117*, 616–623.

(93) Wang, H.; Maiyalagan, T.; Wang, X. Review on Recent Progress in Nitrogen-Doped Graphene: Synthesis, Characterization, and Its Potential Applications. *Acs Catal.* **2012**, *2* (5), 781–794.

(94) Joshi, R. K.; Carbone, P.; Wang, F.-C.; Kravets, V. G.; Su, Y.; Grigorieva, I. V.; Wu, H. A.; Geim, A. K.; Nair, R. R. Precise and Ultrafast Molecular Sieving through Graphene Oxide Membranes. *Science* **2014**, *343* (6172), 752–754.

(95) Rein, M.; Richter, N.; Parvez, K.; Feng, X.; Sachdev, H.; Kläui, M.; Müllen, K. Magnetoresistance and Charge Transport in Graphene Governed by Nitrogen Dopants. *ACS Nano* **2015**, *9* (2), 1360–1366.

(96) Cheng, C.; Jiang, G.; Garvey, C. J.; Wang, Y.; Simon, G. P.; Liu, J. Z.; Li, D. Ion Transport in Complex Layered Graphene-Based Membranes with Tuneable Interlayer Spacing. *Sci. Adv.* **2016**, *2* (2), e1501272.

(97) Liu, J.; Cui, L.; Losic, D. Graphene and Graphene Oxide as New Nanocarriers for Drug Delivery Applications. *Acta Biomater.* **2013**, *9* (12), 9243–9257.

(98) Compton, O. C.; Cranford, S. W.; Putz, K. W.; An, Z.; Brinson, L. C.; Buehler, M. J.; Nguyen, S. T. Tuning the Mechanical Properties of Graphene Oxide Paper and Its Associated Polymer Nanocomposites by Controlling Cooperative Intersheet Hydrogen Bonding. *Acs Nano* **2012**, *6* (3), 2008–2019.

(99) Kawai, S.; Benassi, A.; Gnecco, E.; Söde, H.; Pawlak, R.; Feng, X.; Müllen, K.; Passerone, D.; Pignedoli, C. A.; Ruffieux, P.; et al. Superlubricity of Graphene Nanoribbons on Gold Surfaces. *Science* **2016**, *351* (6276), 957–961.

(100) Berman, D.; Erdemir, A.; Sumant, A. V. Few Layer Graphene to Reduce Wear and Friction on Sliding Steel Surfaces. *Carbon* **2013**, *54*, 454–459.

(101) Yang, K.; Feng, L.; Shi, X.; Liu, Z. Nano-Graphene in Biomedicine: Theranostic Applications. *Chem. Soc. Rev.* **2013**, *42* (2), 530–547.

(102) Lee, Y.-W.; An, G.-H.; Kim, B.-S.; Hong, J.; Pak, S.; Lee, E.-H.; Cho, Y.; Lee, J.; Giraud, P.; Cha, S. N.; et al. Synergistic Effects of a Multifunctional Graphene Based Interlayer on Electrochemical Behavior and Structural Stability. *ACS Appl. Mater. Interfaces* **2016**, *8* (27), 17651–17658.

(103) Yang, X.; Wang, Y.; Huang, X.; Ma, Y.; Huang, Y.; Yang, R.; Duan, H.; Chen, Y. Multi-Functionalized Graphene Oxide Based Anticancer Drug-Carrier with Dual-Targeting Function and PH-Sensitivity. *J. Mater. Chem.* **2011**, *21* (10), 3448–3454.

(104) Liu, J.; Fu, S.; Yuan, B.; Li, Y.; Deng, Z. Toward a Universal "Adhesive Nanosheet" for the Assembly of Multiple Nanoparticles Based on a Protein-Induced Reduction/Decoration of Graphene Oxide. *J. Am. Chem. Soc.* **2010**, *132* (21), 7279–7281.

(105) Zhang, J.; Zhang, F.; Yang, H.; Huang, X.; Liu, H.; Zhang, J.; Guo, S. Graphene Oxide as a Matrix for Enzyme Immobilization. *Langmuir* **2010**, *26* (9), 6083–6085.

(106) Wahid, M. H.; Eroglu, E.; Chen, X.; Smith, S. M.; Raston, C. L. Entrapment of Chlorella Vulgaris Cells within Graphene Oxide Layers. *Rsc Adv.* **2013**, *3* (22), 8180–8183.

(107) Yang, Y.; Zhang, Y.-M.; Chen, Y.; Zhao, D.; Chen, J.-T.; Liu, Y. Construction of a Graphene Oxide Based Noncovalent Multiple Nanosupramolecular Assembly as a Scaffold for Drug Delivery. *Chem. Eur. J.* **2012**, *18* (14), 4208–4215.

(108) Georgakilas, V.; Tiwari, J. N.; Kemp, K. C.; Perrnan, J. A.; Bourlinos, A. B.; Kim, K. S.; Zboril, R. Noncovalent Functionalization of Graphene and Graphene Oxide for Energy Materials, Biosensing, Catalytic, and Biomedical Applications. **2016**.

(109) Fernández-Merino, M. J.; Paredes, J. I.; Villar-Rodil, S.; Guardia, L.; Solís-Fernández, P.; Salinas-Torres, D.; Cazorla-Amorós, D.; Morallon, E.; Martínez-Alonso, A.; Tascón, J. M. D. Investigating the Influence of Surfactants on the Stabilization of Aqueous Reduced Graphene Oxide Dispersions and the Characteristics of Their Composite Films. *Carbon* **2012**, *50* (9), 3184–3194.

(110) Carrasco, P. M.; Montes, S.; García, I.; Borghei, M.; Jiang, H.; Odriozola, I.; Cabañero, G.; Ruiz, V. High-Concentration Aqueous Dispersions of Graphene Produced by Exfoliation of Graphite Using Cellulose Nanocrystals. *Carbon* **2014**, *70*, 157–163.

(111) Choi, E.-Y.; Han, T. H.; Hong, J.; Kim, J. E.; Lee, S. H.; Kim, H. W.; Kim, S. O. Noncovalent Functionalization of Graphene with End-Functional Polymers. *J. Mater. Chem.* **2010**, *20* (10), 1907–1912.

(112) Pollard, A. J.; Perkins, E. W.; Smith, N. A.; Saywell, A.; Goretzki, G.; Phillips, A. G.; Argent, S. P.; Sachdev, H.; Müller, F.; Hüfner, S.; et al. Supramolecular Assemblies Formed on an Epitaxial Graphene Superstructure. *Angew. Chem. Int. Ed.* **2010**, *49* (10), 1794–1799.

(113) Li, M.; Wang, Y.; Liu, Q.; Li, Q.; Cheng, Y.; Zheng, Y.; Xi, T.; Wei, S. In Situ Synthesis and Biocompatibility of Nano Hydroxyapatite on Pristine and Chitosan Functionalized Graphene Oxide. *J. Mater. Chem. B* **2013**, *1* (4), 475–484.

(114) Cano, M.; Khan, U.; Sainsbury, T.; O'Neill, A.; Wang, Z.; McGovern, I. T.; Maser, W. K.; Benito, A. M.; Coleman, J. N. Improving the Mechanical Properties of Graphene Oxide Based Materials by Covalent Attachment of Polymer Chains. *Carbon* **2013**, *52*, 363–371.

(115) Jia, Z.; Wang, Y. Covalently Crosslinked Graphene Oxide Membranes by Esterification Reactions for Ions Separation. *J. Mater. Chem. A* **2015**, *3* (8), 4405–4412.

(116) Wan, Y.-J.; Tang, L.-C.; Gong, L.-X.; Yan, D.; Li, Y.-B.; Wu, L.-B.; Jiang, J.-X.; Lai, G.-Q. Grafting of Epoxy Chains onto Graphene Oxide for Epoxy Composites with Improved Mechanical and Thermal Properties. *Carbon* **2014**, *69*, 467–480.

(117) Feng, L.; Yang, X.; Shi, X.; Tan, X.; Peng, R.; Wang, J.; Liu, Z. Polyethylene Glycol and Polyethylenimine Dual-Functionalized Nano-Graphene Oxide for Photothermally Enhanced Gene Delivery. *Small* **2013**, *9* (11), 1989–1997.

(118) Wojcik, A.; Kamat, P. V. Reduced Graphene Oxide and Porphyrin. An Interactive Affair in 2-D. *ACS Nano* **2010**, *4* (11), 6697–6706.

(119) Pan, Y.; Bao, H.; Sahoo, N. G.; Wu, T.; Li, L. Water-Soluble Poly (N-Isopropylacrylamide)–Graphene Sheets Synthesized via Click Chemistry for Drug Delivery. *Adv. Funct. Mater.* **2011**, *21* (14), 2754–2763.

(120) Ai, W.; Liu, J.-Q.; Du, Z.-Z.; Liu, X.-X.; Shang, J.-Z.; Yi, M.-D.; Xie, L.-H.; Zhang, J.-J.; Lin, H.-F.; Yu, T.; et al. One-Pot, Aqueous-Phase Synthesis of Graphene Oxide Functionalized with Heterocyclic Groups to Give Increased Solubility in Organic Solvents. *RSC Adv.* **2013**, *3* (1), 45–49.

(121) Carpio, I. E. M.; Mangadlao, J. D.; Nguyen, H. N.; Advincula, R. C.; Rodrigues, D. F. Graphene Oxide Functionalized with Ethylenediamine Triacetic Acid for Heavy Metal Adsorption and Anti-Microbial Applications. *Carbon* **2014**, *77*, 289–301.

(122) Liu, J.; Wang, Y.; Xu, S.; Sun, D. D. Synthesis of Graphene Soluble in Organic Solvents by Simultaneous Ether-Functionalization with Octadecane Groups and Reduction. *Mater. Lett.* **2010**, *64* (20), 2236–2239.

(123) Zhao, H.; Wu, L.; Zhou, Z.; Zhang, L.; Chen, H. Improving the Antifouling Property of Polysulfone Ultrafiltration Membrane by Incorporation of Isocyanate-Treated Graphene Oxide. *Phys. Chem. Chem. Phys.* **2013**, *15* (23), 9084–9092.

(124) Jiang, T.; Kuila, T.; Kim, N. H.; Lee, J. H. Effects of Surface-Modified Silica Nanoparticles Attached Graphene Oxide Using Isocyanate-Terminated Flexible Polymer Chains on the Mechanical Properties of Epoxy Composites. *J. Mater. Chem. A* **2014**, *2* (27), 10557–10567.

(125) Thomas, H. R.; Marsden, A. J.; Walker, M.; Wilson, N. R.; Rourke, J. P. Sulfur-Functionalized Graphene Oxide by Epoxide Ring-Opening. *Angew. Chem. Int. Ed.* **2014**, *53* (29), 7613–7618.

(126) Voylov, D.; Saito, T.; Lokitz, B.; Uhrig, D.; Wang, Y.; Agapov, A.; Holt, A.; Bocharova, V.; Kisliuk, A.; Sokolov, A. P. Graphene Oxide as a Radical Initiator: Free Radical and Controlled Radical Polymerization of Sodium 4-

Vinylbenzenesulfonate with Graphene Oxide. *ACS Macro Lett.* **2016**, *5* (2), 199–202.

(127) Kan, L.; Xu, Z.; Gao, C. General Avenue to Individually Dispersed Graphene Oxide-Based Two-Dimensional Molecular Brushes by Free Radical Polymerization. *Macromolecules* **2011**, *44* (3), 444–452.

(128) Cao, Y.; Osuna, S.; Liang, Y.; Haddon, R. C.; Houk, K. N. Diels–Alder Reactions of Graphene: Computational Predictions of Products and Sites of Reaction. *J. Am. Chem. Soc.* **2013**, *135* (46), 17643–17649.

(129) Sarkar, S.; Bekyarova, E.; Niyogi, S.; Haddon, R. C. Diels- Alder Chemistry of Graphite and Graphene: Graphene as Diene and Dienophile. *J. Am. Chem. Soc.* **2011**, *133* (10), 3324–3327.

(130) Li, J.; Li, M.; Zhou, L.-L.; Lang, S.-Y.; Lu, H.-Y.; Wang, D.; Chen, C.-F.; Wan, L.-J. Click and Patterned Functionalization of Graphene by Diels–Alder Reaction. *J. Am. Chem. Soc.* **2016**, *138* (24), 7448–7451.

(131) Luong, N. D.; Sinh, L. H.; Johansson, L.-S.; Campell, J.; Seppälä, J. Functional Graphene by Thiol-Ene Click Chemistry. *Chem. – Eur. J.* **2015**, *21* (8), 3183–3186.

(132) Dai, L. Functionalization of Graphene for Efficient Energy Conversion and Storage. *Acc. Chem. Res.* **2012**, *46* (1), 31–42.

(133) Yuan, W.; Shi, G. Graphene-Based Gas Sensors. *J. Mater. Chem. A* **2013**, *1* (35), 10078–10091.

(134) Wu, S.; He, Q.; Tan, C.; Wang, Y.; Zhang, H. Graphene-Based Electrochemical Sensors. *Small* **2013**, *9* (8), 1160–1172.

(135) Bogue, R. Graphene Sensors: A Review of Recent Developments. *Sens. Rev.* **2014**, *34* (3), 233–238.

(136) Richardson, J. J.; Cui, J.; Björnmalm, M.; Braunger, J. A.; Ejima, H.; Caruso, F. Innovation in Layer-by-Layer Assembly. *Chem. Rev.* **2016**, *116* (23), 14828–14867.

(137) Richardson, J. J.; Björnmalm, M.; Caruso, F. Technology-Driven Layer-by-Layer Assembly of Nanofilms. *Science* **2015**, *348* (6233), aaa2491.

(138) Engel, Y.; Schiffman, J. D.; Goddard, J. M.; Rotello, V. M. Nanomanufacturing of Biomaterials. *Mater. Today* **2012**, *15* (11), 478–485.

(139) Richardson, J. J.; Björnmalm, M.; Caruso, F. Technology-Driven Layer-by-Layer Assembly of Nanofilms. *Science* **2015**, *348* (6233), aaa2491.

(140) Faine, B. *The Complete Guide to Screen Printing*; Writers Digest Books, 1993.

(141) Hu, K.; Tolentino, L. S.; Kulkarni, D. D.; Ye, C.; Kumar, S.; Tsukruk, V. V. Written-in Conductive Patterns on Robust Graphene Oxide Biopaper by Electrochemical Microstamping. *Angew. Chem. Int. Ed.* **2013**, *52* (51), 13784–13788.

(142) Chen, H.; Müller, M. B.; Gilmore, K. J.; Wallace, G. G.; Li, D. Mechanically Strong, Electrically Conductive, and Biocompatible Graphene Paper. *Adv. Mater.* **2008**, *20* (18), 3557–3561.

(143) Putz, K. W.; Compton, O. C.; Palmeri, M. J.; Nguyen, S. T.; Brinson, L. C. High-Nanofiller-Content Graphene Oxide–Polymer Nanocomposites via Vacuum-Assisted Self-Assembly. *Adv. Funct. Mater.* **2010**, *20* (19), 3322–3329.

(144) Dikin, D. A.; Stankovich, S.; Zimney, E. J.; Piner, R. D.; Dommett, G. H. B.; Evmenenko, G.; Nguyen, S. T.; Ruoff, R. S. Preparation and Characterization of Graphene Oxide Paper. *Nature* **2007**, *448* (7152), 457–460.

(145) Cheng, H.; Liu, J.; Zhao, Y.; Hu, C.; Zhang, Z.; Chen, N.; Jiang, L.; Qu, L. Graphene Fibers with Predetermined Deformation as Moisture-Triggered Actuators and Robots. *Angew. Chem. Int. Ed.* **2013**, *52* (40), 10482–10486.

(146) Kim, J.; Jeon, J.-H.; Kim, H.-J.; Lim, H.; Oh, I.-K. Durable and Water-Floatable Ionic Polymer Actuator with Hydrophobic and Asymmetrically Laser-Scribed Reduced Graphene Oxide Paper Electrodes. *ACS Nano* **2014**, *8* (3), 2986–2997.

(147) Lu, L.; Liu, J.; Hu, Y.; Zhang, Y.; Chen, W. Graphene-Stabilized Silver Nanoparticle Electrochemical Electrode for Actuator Design. *Adv. Mater.* **2013**, *25* (9), 1270–1274.

(148) Kim, J. H.; Chang, W. S.; Kim, D.; Yang, J. R.; Han, J. T.; Lee, G.-W.; Kim, J. T.; Seol, S. K. 3D Printing of Reduced Graphene Oxide Nanowires. *Adv. Mater.* **2015**, *27* (1), 157–161.

(149) Gao, W.; Singh, N.; Song, L.; Liu, Z.; Reddy, A. L. M.; Ci, L.; Vajtai, R.; Zhang, Q.; Wei, B.; Ajayan, P. M. Direct Laser Writing of Micro-Supercapacitors on Hydrated Graphite Oxide Films. *Nat. Nanotechnol.* **2011**, *6* (8), 496–500.

(150) Zhang, B.; Zhang, J.; Sang, X.; Liu, C.; Luo, T.; Peng, L.; Han, B.; Tan, X.; Ma, X.; Wang, D.; et al. Cellular Graphene Aerogel Combines Ultralow Weight and High Mechanical Strength: A Highly Efficient Reactor for Catalytic Hydrogenation. *Sci. Rep.* **2016**, *6*.

(151) Lipson, H.; Kurman, M. *Fabricated: The New World of 3D Printing*; John Wiley & Sons, 2013.

(152) Hu, K.; Xiong, R.; Guo, H.; Ma, R.; Zhang, S.; Wang, Z. L.; Tsukruk, V. V. Self-Powered Electronic Skin with Biotactile Selectivity. *Adv. Mater.* **2016**, *28* (18), 3549–3556.

(153) Leist, S. K.; Zhou, J. Current Status of 4D Printing Technology and the Potential of Light-Reactive Smart Materials as 4D Printable Materials. *Virtual Phys. Prototyp.* **2016**, *11* (4), 249–262.

(154) Liu, Y.; Boyles, J. K.; Genzer, J.; Dickey, M. D. Self-Folding of Polymer Sheets Using Local Light Absorption. *Soft Matter* **2012**, *8* (6), 1764–1769.

(155) K. Chee, W.; N. Lim, H.; M. Huang, N.; Harrison, I. Nanocomposites of Graphene/Polymers: A Review. *RSC Adv.* **2015**, *5* (83), 68014–68051.

(156) Rockwood, D. N.; Preda, R. C.; Yücel, T.; Wang, X.; Lovett, M. L.; Kaplan, D. L. Materials Fabrication from Bombyx Mori Silk Fibroin. *Nat. Protoc.* **2011**, *6* (10), 1612–1631.

(157) Hummers, W. S.; Offeman, R. E. Preparation of Graphitic Oxide. *J. Am. Chem. Soc.* **1958**, *80* (6), 1339–1339.

(158) Wang, Y.; Ma, R.; Hu, K.; Kim, S.; Fang, G.; Shao, Z.; Tsukruk, V. V. Dramatic Enhancement of Graphene Oxide/Silk Nanocomposite Membranes: Increasing Toughness, Strength, and Young's Modulus via Annealing of Interfacial Structures. *ACS Appl. Mater. Interfaces* **2016**, *8* (37), 24962–24973.

(159) Ma, R.; Tsukruk, V. V. Seriography-Guided Reduction of Graphene Oxide Biopapers for Wearable Sensory Electronics. *Adv. Funct. Mater.* **2017**, *27* (10).

(160) Sellinger, A.; Weiss, P. M.; Nguyen, A.; Lu, Y.; Assink, R. A.; Gong, W.; Brinker, C. J. Continuous Self-Assembly of Organic–Inorganic Nanocomposite Coatings That Mimic Nacre. *Nature* **1998**, *394* (6690), 256.

(161) Zhao, H.; Yue, Y.; Zhang, Y.; Li, L.; Guo, L. Ternary Artificial Nacre Reinforced by Ultrathin Amorphous Alumina with Exceptional Mechanical Properties. *Adv. Mater.* **2016**, *28* (10), 2037–2042.

(162) Cheng, Q.; Duan, J.; Zhang, Q.; Jiang, L. Learning from Nature: Constructing Integrated Graphene-Based Artificial Nacre. *ACS Nano* **2015**, *9* (3), 2231–2234.

(163) Zhang, N.; Yang, S.; Xiong, L.; Hong, Y.; Chen, Y. Nanoscale Toughening Mechanism of Nacre Tablet. *J. Mech. Behav. Biomed. Mater.* **2016**, *53*, 200–209.

(164) Li, Y.-Q.; Yu, T.; Yang, T.-Y.; Zheng, L.-X.; Liao, K. Bio-Inspired Nacre-like Composite Films Based on Graphene with Superior Mechanical, Electrical, and Biocompatible Properties. *Adv. Mater.* **2012**, *24* (25), 3426–3431.

(165) Sen, D.; Buehler, M. J. Structural Hierarchies Define Toughness and Defect-Tolerance despite Simple and Mechanically Inferior Brittle Building Blocks. *Sci. Rep.* **2011**, *1*, 35.

(166) Mirkhalaf, M.; Dastjerdi, A. K.; Barthelat, F. Overcoming the Brittleness of Glass through Bio-Inspiration and Micro-Architecture. *Nat. Commun.* **2014**, *5*, 3166.

(167) Corni, I.; Harvey, T. J.; Wharton, J. A.; Stokes, K. R.; Walsh, F. C.; Wood, R. J. K. A Review of Experimental Techniques to Produce a Nacre-like Structure. *Bioinspir. Biomim.* **2012**, *7* (3), 031001.

(168) Wang, J.; Cheng, Q.; Tang, Z. Layered Nanocomposites Inspired by the Structure and Mechanical Properties of Nacre. *Chem. Soc. Rev.* **2012**, *41* (3), 1111–1129.

(169) Clegg, W. J.; Kendall, K.; Alford, N. M.; Button, T. W.; Birchall, J. D. A Simple Way to Make Tough Ceramics. *Nature* **1990**, *347* (6292), 455.

(170) Deville, S.; Saiz, E.; Nalla, R. K.; Tomsia, A. P. Freezing as a Path to Build Complex Composites. *Science* **2006**, *311* (5760), 515–518.

(171) Espinosa, H. D.; Juster, A. L.; Latourte, F. J.; Loh, O. Y.; Gregoire, D.; Zavattieri, P. D. Tablet-Level Origin of Toughening in Abalone Shells and Translation to Synthetic Composite Materials. *Nat. Commun.* **2011**, *2*, 173.

(172) Finnemore, A.; Cunha, P.; Shean, T.; Vignolini, S.; Guldin, S.; Oyen, M.; Steiner, U. Biomimetic Layer-by-Layer Assembly of Artificial Nacre. *Nat. Commun.* **2012**, *3*, 966.

(173) Zhong, D.; Yang, Q.; Guo, L.; Dou, S.; Liu, K.; Jiang, L. Fusion of Nacre, Mussel, and Lotus Leaf: Bio-Inspired Graphene Composite Paper with Multifunctional Integration. *Nanoscale* **2013**, *5* (13), 5758–5764.

(174) Cui, W.; Li, M.; Liu, J.; Wang, B.; Zhang, C.; Jiang, L.; Cheng, Q. A Strong Integrated Strength and Toughness Artificial Nacre Based on Dopamine Cross-Linked Graphene Oxide. *ACS Nano* **2014**, *8* (9), 9511–9517.

(175) Cho, J.; Char, K.; Hong, J.-D.; Lee, K.-B. Fabrication of Highly Ordered Multilayer Films Using a Spin Self-Assembly Method. *Adv. Mater.* **2001**, *13* (14), 1076–1078.

(176) Cheng, Y.; Koh, L.-D.; Li, D.; Ji, B.; Zhang, Y.; Yeo, J.; Guan, G.; Han, M.-Y.; Zhang, Y.-W. Peptide–Graphene Interactions Enhance the Mechanical Properties of Silk Fibroin. *ACS Appl. Mater. Interfaces* **2015**, *7* (39), 21787–21796.

(177) Espinosa, H. D.; Rim, J. E.; Barthelat, F.; Buehler, M. J. Merger of Structure and Material in Nacre and Bone–Perspectives on de Novo Biomimetic Materials. *Prog. Mater. Sci.* **2009**, *54* (8), 1059–1100.

(178) Hu, X.; Kaplan, D.; Cebe, P. Dynamic Protein- Water Relationships during β-Sheet Formation. *Macromolecules* **2008**, *41* (11), 3939–3948.

(179) Hu, X.; Shmelev, K.; Sun, L.; Gil, E.-S.; Park, S.-H.; Cebe, P.; Kaplan, D. L. Regulation of Silk Material Structure by Temperature-Controlled Water Vapor Annealing. *Biomacromolecules* **2011**, *12* (5), 1686–1696.

(180) Ling, S.; Li, C.; Adamcik, J.; Wang, S.; Shao, Z.; Chen, X.; Mezzenga, R. Directed Growth of Silk Nanofibrils on Graphene and Their Hybrid Nanocomposites. *ACS Macro Lett.* **2014**, *3* (2), 146–152.

(181) Shao, Z.; Wang, Y.; Song, Y.-F.; Wang, Y.; Chen, X.; Xia, Y.-Y. Graphene/Silk Fibroin Based Carbon Nanocomposites for High Performance Supercapacitors. *J. Mater. Chem. A* **2014**.

(182) Grant, A. M.; Kim, H. S.; Dupnock, T. L.; Hu, K.; Yingling, Y. G.; Tsukruk, V. V. Silk Fibroin–Substrate Interactions at Heterogeneous Nanocomposite Interfaces. *Adv. Funct. Mater.* **2016**, *26* (35), 6380–6392.

(183) Hu, X.; Xu, Z.; Gao, C. Multifunctional, Supramolecular, Continuous Artificial Nacre Fibres. *Sci. Rep.* **2012**, *2*, 767.

(184) Reiter, G.; Hamieh, M.; Damman, P.; Sclavons, S.; Gabriele, S.; Vilmin, T.; Raphaël, E. Residual Stresses in Thin Polymer Films Cause Rupture and Dominate Early Stages of Dewetting. *Nat. Mater.* **2005**, *4* (10), 754.

(185) Kong, J.; Yu, S. Fourier Transform Infrared Spectroscopic Analysis of Protein Secondary Structures. *Acta Biochim. Biophys. Sin.* **2007**, *39* (8), 549–559.

(186) Huang, L.; Li, C.; Yuan, W.; Shi, G. Strong Composite Films with Layered Structures Prepared by Casting Silk Fibroin–Graphene Oxide Hydrogels. *Nanoscale* **2013**, *5* (9), 3780–3786.

(187) Begley, M. R.; Philips, N. R.; Compton, B. G.; Wilbrink, D. V.; Ritchie, R. O.; Utz, M. Micromechanical Models to Guide the Development of Synthetic 'Brick and Mortar'Composites. *J. Mech. Phys. Solids* **2012**, *60* (8), 1545–1560.

(188) Jin, H.-J.; Park, J.; Karageorgiou, V.; Kim, U.-J.; Valluzzi, R.; Cebe, P.; Kaplan, D. L. Water-Stable Silk Films with Reduced β-Sheet Content. *Adv. Funct. Mater.* **2005**, *15* (8), 1241–1247.

(189) Ling, S.; Qi, Z.; Knight, D. P.; Huang, Y.; Huang, L.; Zhou, H.; Shao, Z.; Chen, X. Insight into the Structure of Single Antheraea Pernyi Silkworm Fibers Using Synchrotron FTIR Microspectroscopy. *Biomacromolecules* **2013**, *14* (6), 1885–1892.

(190) Pendolino, F.; Armata, N.; Masullo, T.; Cuttitta, A. Temperature Influence on the Synthesis of Pristine Graphene Oxide and Graphite Oxide. *Mater. Chem. Phys.* **2015**, *164*, 71–77.

(191) Yu, S.; Liu, J.; Zhu, W.; Hu, Z.-T.; Lim, T.-T.; Yan, X. Facile Room-Temperature Synthesis of Carboxylated Graphene Oxide-Copper Sulfide Nanocomposite with High Photodegradation and Disinfection Activities under Solar Light Irradiation. *Sci. Rep.* **2015**, *5*, 16369.

(192) Fang, G.; Zheng, Z.; Yao, J.; Chen, M.; Tang, Y.; Zhong, J.; Qi, Z.; Li, Z.; Shao, Z.; Chen, X. Tough Protein–Carbon Nanotube Hybrid Fibers Comparable to Natural Spider Silks. *J. Mater. Chem. B* **2015**, *3* (19), 3940–3947.

(193) Ling, S.; Qi, Z.; Knight, D. P.; Shao, Z.; Chen, X. Synchrotron FTIR Microspectroscopy of Single Natural Silk Fibers. *Biomacromolecules* **2011**, *12* (9), 3344–3349.

(194) Kercher, A. K.; Nagle, D. C. Microstructural Evolution during Charcoal Carbonization by X-Ray Diffraction Analysis. *Carbon* **2003**, *41* (1), 15–27.

(195) Wang, Q.; Yang, Y.; Chen, X.; Shao, Z. Investigation of Rheological Properties and Conformation of Silk Fibroin in the Solution of AmimCl. *Biomacromolecules* **2012**, *13* (6), 1875–1881.

(196) Li, G.; Zhou, P.; Shao, Z.; Xie, X.; Chen, X.; Wang, H.; Chunyu, L.; Yu, T. The Natural Silk Spinning Process. *FEBS J.* **2001**, *268* (24), 6600–6606.

(197) Su, D.; Jiang, L.; Chen, X.; Dong, J.; Shao, Z. Enhancing the Gelation and Bioactivity of Injectable Silk Fibroin Hydrogel with Laponite Nanoplatelets. *ACS Appl. Mater. Interfaces* **2016**, *8* (15), 9619–9628.

(198) Luo, K.; Yang, Y.; Shao, Z. Physically Crosslinked Biocompatible Silk-Fibroin-Based Hydrogels with High Mechanical Performance. *Adv. Funct. Mater.* **2016**, *26* (6), 872–880.

(199) Kulkarni, D. D.; Kim, S.; Chyasnavichyus, M.; Hu, K.; Fedorov, A. G.; Tsukruk, V. V. Chemical Reduction of Individual Graphene Oxide Sheets as Revealed by Electrostatic Force Microscopy. *J. Am. Chem. Soc.* **2014**, *136* (18), 6546–6549.

(200) National Research Council. *The Flexible Electronics Opportunity*; National Academies Press, 2015.

(201) Wong, W. S.; Salleo, A. *Flexible Electronics: Materials and Applications*; Springer Science & Business Media, 2009.

(202) Kim, D.-H.; Ghaffari, R.; Lu, N.; Rogers, J. A. Flexible and Stretchable Electronics for Biointegrated Devices. *Annu. Rev. Biomed. Eng.* **2012**, *14* (1), 113–128.

(203) Rogers, J. A. Electronics for the Human Body. *J. Am. Med. Assoc.* **2015**, *313* (6), 561–562.

(204) Nathan, A.; Ahnood, A.; Cole, M. T.; Lee, S.; Suzuki, Y.; Hiralal, P.; Bonaccorso, F.; Hasan, T.; Garcia-Gancedo, L.; Dyadyusha, A.; et al. Flexible Electronics: The Next Ubiquitous Platform. *Proc. IEEE* **2012**, *100* (Special Centennial Issue), 1486–1517.

(205) Yoon, J.; Baca, A. J.; Park, S.-I.; Elvikis, P.; Geddes, J. B.; Li, L.; Kim, R. H.; Xiao, J.; Wang, S.; Kim, T.-H.; et al. Ultrathin Silicon Solar Microcells for Semitransparent, Mechanically Flexible and Microconcentrator Module Designs. *Nat. Mater.* **2008**, *7* (11), 907–915.

(206) Mack, S.; Meitl, M. A.; Baca, A. J.; Zhu, Z.-T.; Rogers, J. A. Mechanically Flexible Thin-Film Transistors That Use Ultrathin Ribbons of Silicon Derived from Bulk Wafers. *Appl. Phys. Lett.* **2006**, *88* (21), 213101.

(207) Peng, Y.; Burtovyy, R.; Yang, Y.; Urban, M. W.; Kennedy, M. S.; Kornev, K. G.; Bordia, R.; Luzinov, I. Towards Scalable Fabrication of Ultrasmooth and Porous Thin Carbon Films. *Carbon* **2016**, *96*, 184–195.

(208) Mahajan, A.; Frisbie, C. D.; Francis, L. F. Optimization of Aerosol Jet Printing for High-Resolution, High-Aspect Ratio Silver Lines. *ACS Appl. Mater. Interfaces* **2013**, *5* (11), 4856–4864.

(209) Kaltenbrunner, M.; Sekitani, T.; Reeder, J.; Yokota, T.; Kuribara, K.; Tokuhara, T.; Drack, M.; Schwödiauer, R.; Graz, I.; Bauer-Gogonea, S.; et al. An Ultra-Lightweight Design for Imperceptible Plastic Electronics. *Nature* **2013**, *499* (7459), 458–463.

(210) Blees, M. K.; Barnard, A. W.; Rose, P. A.; Roberts, S. P.; McGill, K. L.; Huang, P. Y.; Ruyack, A. R.; Kevek, J. W.; Kobrin, B.; Muller, D. A.; et al. Graphene Kirigami. *Nature* **2015**, *524* (7564), 204–207.

(211) Khang, D.-Y.; Rogers, J. A.; Lee, H. H. Mechanical Buckling: Mechanics, Metrology, and Stretchable Electronics. *Adv. Funct. Mater.* **2009**, *19* (10), 1526–1536.

(212) Rogers, J. A.; Someya, T.; Huang, Y. Materials and Mechanics for Stretchable Electronics. *Science* **2010**, *327* (5973), 1603–1607.

(213) Ahn, B. Y.; Duoss, E. B.; Motala, M. J.; Guo, X.; Park, S.-I.; Xiong, Y.; Yoon, J.; Nuzzo, R. G.; Rogers, J. A.; Lewis, J. A. Omnidirectional Printing of Flexible, Stretchable, and Spanning Silver Microelectrodes. *Science* **2009**, *323* (5921), 1590–1593.

(214) Matsuhisa, N.; Kaltenbrunner, M.; Yokota, T.; Jinno, H.; Kuribara, K.; Sekitani, T.; Someya, T. Printable Elastic Conductors with a High Conductivity for Electronic Textile Applications. *Nat. Commun.* **2015**, *6*, 7461.

(215) Corea, J. R.; Flynn, A. M.; Lechêne, B.; Scott, G.; Reed, G. D.; Shin, P. J.; Lustig, M.; Arias, A. C. Screen-Printed Flexible MRI Receive Coils. *Nat. Commun.* **2016**, *7*, 10839.

(216) Yamada, T.; Fukuhara, K.; Matsuoka, K.; Minemawari, H.; Tsutsumi, J.; Fukuda, N.; Aoshima, K.; Arai, S.; Makita, Y.; Kubo, H.; et al. Nanoparticle Chemisorption Printing Technique for Conductive Silver Patterning with Submicron Resolution. *Nat. Commun.* **2016**, *7*, 11402.

(217) Calvert, P. Inkjet Printing for Materials and Devices. *Chem. Mater.* **2001**, *13* (10), 3299–3305.

(218) Hu, K.; Gupta, M. K.; Kulkarni, D. D.; Tsukruk, V. V. Ultra-Robust Graphene Oxide-Silk Fibroin Nanocomposite Membranes. *Adv. Mater.* **2013**, *25* (16), 2301–2307.

(219) Hu, K.; Tsukruk, V. V. Tuning the Electronic Properties of Robust Bio-Bond Graphene Papers by Spontaneous Electrochemical Reduction: From Insulators to Flexible Semi-Metals. *Chem. Mater.* **2015**, *27* (19), 6717–6729.

(220) Li, J.; Ye, F.; Vaziri, S.; Muhammed, M.; Lemme, M. C.; Östling, M. Efficient Inkjet Printing of Graphene. *Adv. Mater.* **2013**, *25* (29), 3985–3992.

(221) Shin, K.-Y.; Hong, J.-Y.; Jang, J. Micropatterning of Graphene Sheets by Inkjet Printing and Its Wideband Dipole-Antenna Application. *Adv. Mater.* **2011**, *23* (18), 2113–2118.

(222) Torrisi, F.; Hasan, T.; Wu, W.; Sun, Z.; Lombardo, A.; Kulmala, T. S.; Hsieh, G.-W.; Jung, S.; Bonaccorso, F.; Paul, P. J.; et al. Inkjet-Printed Graphene Electronics. *ACS Nano* **2012**, *6* (4), 2992–3006.

(223) Zhang, L.; Liu, H.; Zhao, Y.; Sun, X.; Wen, Y.; Guo, Y.; Gao, X.; Di, C.; Yu, G.; Liu, Y. Inkjet Printing High-Resolution, Large-Area Graphene Patterns by Coffee-Ring Lithography. *Adv. Mater.* **2012**, *24* (3), 436–440.

(224) Kim, S. H.; Hong, K.; Xie, W.; Lee, K. H.; Zhang, S.; Lodge, T. P.; Frisbie, C. D. Electrolyte-Gated Transistors for Organic and Printed Electronics. *Adv. Mater.* **2013**, *25* (13), 1822–1846.

(225) Hyun, W. J.; Secor, E. B.; Rojas, G. A.; Hersam, M. C.; Francis, L. F.; Frisbie, C. D. All-Printed, Foldable Organic Thin-Film Transistors on Glassine Paper. *Adv. Mater.* **2015**, *27* (44), 7058–7064.

(226) Hyun, W. J.; Secor, E. B.; Hersam, M. C.; Frisbie, C. D.; Francis, L. F. High-Resolution Patterning of Graphene by Screen Printing with a Silicon Stencil for Highly Flexible Printed Electronics. *Adv. Mater.* **2015**, *27* (1), 109–115.

(227) Xu, Y.; Schwab, M. G.; Strudwick, A. J.; Hennig, I.; Feng, X.; Wu, Z.; Müllen, K. Screen-Printable Thin Film Supercapacitor Device Utilizing Graphene/Polyaniline Inks. *Adv. Energy Mater.* **2013**, *3* (8), 1035–1040.

(228) Secor, E. B.; Lim, S.; Zhang, H.; Frisbie, C. D.; Francis, L. F.; Hersam, M. C. Gravure Printing of Graphene for Large-Area Flexible Electronics. *Adv. Mater.* **2014**, *26* (26), 4533–4538.

(229) Pei, S.; Cheng, H.-M. The Reduction of Graphene Oxide. *Carbon* **2012**, *50* (9), 3210–3228.

(230) Park, S.; An, J.; Potts, J. R.; Velamakanni, A.; Murali, S.; Ruoff, R. S. Hydrazine-Reduction of Graphite- and Graphene Oxide. *Carbon* **2011**, *49* (9), 3019–3023.

(231) Jung, I.; Dikin, D. A.; Piner, R. D.; Ruoff, R. S. Tunable Electrical Conductivity of Individual Graphene Oxide Sheets Reduced at "Low" Temperatures. *Nano Lett.* **2008**, *8* (12), 4283–4287.

(232) Dreyer, D. R.; Park, S.; Bielawski, C. W.; Ruoff, R. S. The Chemistry of Graphene Oxide. *Chem Soc Rev* **2010**, *39* (1), 228–240.

(233) Dreyer, D. R.; Murali, S.; Zhu, Y.; Ruoff, R. S.; Bielawski, C. W. Reduction of Graphite Oxide Using Alcohols. *J Mater Chem* **2011**, *21* (10), 3443–3447.

(234) Voiry, D.; Yang, J.; Kupferberg, J.; Fullon, R.; Lee, C.; Jeong, H. Y.; Shin, H. S.; Chhowalla, M. High-Quality Graphene via Microwave Reduction of Solution-Exfoliated Graphene Oxide. *Science* **2016**, 3398.

(235) El-Kady, M. F.; Strong, V.; Dubin, S.; Kaner, R. B. Laser Scribing of High-Performance and Flexible Graphene-Based Electrochemical Capacitors. *Science* **2012**, *335* (6074), 1326–1330.

(236) Yung, K. C.; Liem, H.; Choy, H. S.; Chen, Z. C.; Cheng, K. H.; Cai, Z. X. Laser Direct Patterning of a Reduced-Graphene Oxide Transparent Circuit on a Graphene Oxide Thin Film. *J. Appl. Phys.* **2013**, *113* (24), 244903.

(237) Kymakis, E.; Petridis, C.; Anthopoulos, T. D.; Stratakis, E. Laser-Assisted Reduction of Graphene Oxide for Flexible, Large-Area Optoelectronics. *IEEE J. Sel. Top. Quantum Electron.* **2014**, *20* (1), 106–115.

(238) Hu, K.; Tolentino, L. S.; Kulkarni, D. D.; Ye, C.; Kumar, S.; Tsukruk, V. V. Written-in Conductive Patterns on Robust Graphene Oxide Biopaper by Electrochemical Microstamping. *Angew. Chem. Int. Ed.* **2013**, *52* (51), 13784–13788.

(239) Wei, Z.; Wang, D.; Kim, S.; Kim, S.-Y.; Hu, Y.; Yakes, M. K.; Laracuente, A. R.; Dai, Z.; Marder, S. R.; Berger, C.; et al. Nanoscale Tunable Reduction of Graphene Oxide for Graphene Electronics. *Science* **2010**, *328* (5984), 1373.

(240) *Handbook of Print Media*, 2001 edition.; Kipphan, H., Ed.; Springer: Berlin ; New York, 2001.

(241) Häberlin, H. *Photovoltaics System Design and Practice*, 1 edition.; Wiley: Chichester, West Sussex, 2012.

(242) Krebs, F. C. Fabrication and Processing of Polymer Solar Cells: A Review of Printing and Coating Techniques. *Sol. Energy Mater. Sol. Cells* **2009**, *93* (4), 394–412.

(243) Rockwood, D. N.; Preda, R. C.; Yücel, T.; Wang, X.; Lovett, M. L.; Kaplan, D. L. Materials Fabrication from Bombyx Mori Silk Fibroin. *Nat. Protoc.* **2011**, *6* (10), 1612–1631.

(244) Hummers, W. S.; Offeman, R. E. Preparation of Graphitic Oxide. *J. Am. Chem. Soc.* **1958**, *80* (6), 1339–1339.

(245) Yang, D.; Velamakanni, A.; Bozoklu, G.; Park, S.; Stoller, M.; Piner, R. D.; Stankovich, S.; Jung, I.; Field, D. A.; Ventrice Jr., C. A.; et al. Chemical Analysis of Graphene Oxide Films after Heat and Chemical Treatments by X-Ray Photoelectron and Micro-Raman Spectroscopy. *Carbon* **2009**, *47* (1), 145–152.

(246) Moon, I. K.; Lee, J.; Ruoff, R. S.; Lee, H. Reduced Graphene Oxide by Chemical Graphitization. *Nat. Commun.* **2010**, *1*, 73.

(247) Eigler, S.; Dotzer, C.; Hirsch, A. Visualization of Defect Densities in Reduced Graphene Oxide. *Carbon* **2012**, *50* (10), 3666–3673.

(248) Mark, J. E. *Physical Properties of Polymers Handbook*; Springer, 2007; Vol. 1076.

(249) Crispin, X.; Jakobsson, F. L. E.; Crispin, A.; Grim, P. C. M.; Andersson, P.; Volodin, A.; van Haesendonck, C.; Van der Auweraer, M.; Salaneck, W. R.; Berggren, M. The Origin of the High Conductivity of Poly(3,4-Ethylenedioxythiophene)−Poly(Styrenesulfonate) (PEDOT−PSS) Plastic Electrodes. *Chem. Mater.* **2006**, *18* (18), 4354–4360.

(250) Wang, D.-W.; Li, F.; Zhao, J.; Ren, W.; Chen, Z.-G.; Tan, J.; Wu, Z.-S.; Gentle, I.; Lu, G. Q.; Cheng, H.-M. Fabrication of Graphene/Polyaniline Composite Paper via In Situ Anodic Electropolymerization for High-Performance Flexible Electrode. *ACS Nano* **2009**, *3* (7), 1745–1752.

(251) Russo, A.; Ahn, B. Y.; Adams, J. J.; Duoss, E. B.; Bernhard, J. T.; Lewis, J. A. Pen-on-Paper Flexible Electronics. *Adv. Mater.* **2011**, *23* (30), 3426–3430.

(252) Secor, E. B.; Prabhumirashi, P. L.; Puntambekar, K.; Geier, M. L.; Hersam, M. C. Inkjet Printing of High Conductivity, Flexible Graphene Patterns. *J. Phys. Chem. Lett.* **2013**, *4* (8), 1347–1351.

(253) Bi, H.; Yin, K.; Xie, X.; Ji, J.; Wan, S.; Sun, L.; Terrones, M.; Dresselhaus, M. S. Ultrahigh Humidity Sensitivity of Graphene Oxide. *Sci. Rep.* **2013**, *3*.

(254) Zhang, D.; Tong, J.; Xia, B. Humidity-Sensing Properties of Chemically Reduced Graphene Oxide/Polymer Nanocomposite Film Sensor Based on Layer-by-Layer Nano Self-Assembly. *Sens. Actuators B Chem.* **2014**, *197*, 66–72.

(255) Wang, X.; Xiong, Z.; Liu, Z.; Zhang, T. Exfoliation at the Liquid/Air Interface to Assemble Reduced Graphene Oxide Ultrathin Films for a Flexible Noncontact Sensing Device. *Adv. Mater.* **2015**, *27* (8), 1370–1375.

(256) Wee, B.-H.; Khoh, W.-H.; Sarker, A. K.; Lee, C.-H.; Hong, J.-D. A High-Performance Moisture Sensor Based on Ultralarge Graphene Oxide. *Nanoscale* **2015**, *7* (42), 17805–17811.

(257) Yao, Y.; Chen, X.; Guo, H.; Wu, Z.; Li, X. Humidity Sensing Behaviors of Graphene Oxide-Silicon Bi-Layer Flexible Structure. *Sens. Actuators B Chem.* **2012**, *161* (1), 1053–1058.

(258) Zanella, A.; Bui, N.; Castellani, A.; Vangelista, L.; Zorzi, M. Internet of Things for Smart Cities. *IEEE Internet Things J.* **2014**, *1* (1), 22–32.

(259) Fan, F. R.; Tang, W.; Wang, Z. L. Flexible Nanogenerators for Energy Harvesting and Self-Powered Electronics. *Adv. Mater.* **2016**, *28* (22), 4283–4305.

(260) Yu, X.; Cheng, H.; Zhang, M.; Zhao, Y.; Qu, L.; Shi, G. Graphene-Based Smart Materials. *Nat. Rev. Mater.* **2017**, *2* (9), 17046.

(261) Pramoda, K. P.; Hussain, H.; Koh, H. m.; Tan, H. R.; He, C. B. Covalent Bonded Polymer–Graphene Nanocomposites. *J. Polym. Sci. Part Polym. Chem.* **2010**, *48* (19), 4262–4267.

(262) Gao, W. The Chemistry of Graphene Oxide. In *Graphene Oxide*; Springer, Cham, 2015; pp 61–95.

(263) Shao, Y.; F. El-Kady, M.; J. Wang, L.; Zhang, Q.; Li, Y.; Wang, H.; F. Mousavi, M.; B. Kaner, R. Graphene-Based Materials for Flexible Supercapacitors. *Chem. Soc. Rev.* **2015**, *44* (11), 3639–3665.

(264) Ma, R.; Tsukruk, V. V. Seriography-Guided Reduction of Graphene Oxide Biopapers for Wearable Sensory Electronics. *Adv. Funct. Mater.* **2017**, *27* (10), 1604802.

(265) Hu, K.; Tsukruk, V. V. Tuning the Electronic Properties of Robust Bio-Bond Graphene Papers by Spontaneous Electrochemical Reduction: From Insulators to Flexible Semi-Metals. *Chem. Mater.* **2015**, *27* (19), 6717–6729.

(266) Ling, S.; Wang, Q.; Zhang, D.; Zhang, Y.; Mu, X.; Kaplan, D. L.; Buehler, M. J. Integration of Stiff Graphene and Tough Silk for the Design and Fabrication of Versatile Electronic Materials. *Adv. Funct. Mater. 28* (9), 1705291.

(267) Zhao, N.; Yang, M.; Zhao, Q.; Gao, W.; Xie, T.; Bai, H. Superstretchable Nacre-Mimetic Graphene/Poly(Vinyl Alcohol) Composite Film Based on Interfacial Architectural Engineering. *ACS Nano* **2017**, *11* (5), 4777–4784.

(268) Keten, S.; Xu, Z.; Ihle, B.; Buehler, M. J. Nanoconfinement Controls Stiffness, Strength and Mechanical Toughness of β-Sheet Crystals in Silk. *Nat. Mater.* **2010**, *9* (4), 359–367.

(269) Hu, K.; Kulkarni, D. D.; Choi, I.; Tsukruk, V. V. Graphene-Polymer Nanocomposites for Structural and Functional Applications. *Prog. Polym. Sci.* **2014**, *39* (11), 1934–1972.

(270) Wu, Y.; Farmer, D. B.; Xia, F.; Avouris, P. Graphene Electronics: Materials, Devices, and Circuits. *Proc. IEEE* **2013**, *101* (7), 1620–1637.

(271) Tung, V. C.; Allen, M. J.; Yang, Y.; Kaner, R. B. High-Throughput Solution Processing of Large-Scale Graphene. *Nat. Nanotechnol.* **2009**, *4* (1), 25–29.

(272) Gilje, S.; Han, S.; Wang, M.; Wang, K. L.; Kaner, R. B. A Chemical Route to Graphene for Device Applications. *Nano Lett.* **2007**, *7* (11), 3394–3398.

(273) Sheng, Z.-H.; Shao, L.; Chen, J.-J.; Bao, W.-J.; Wang, F.-B.; Xia, X.-H. Catalyst-Free Synthesis of Nitrogen-Doped Graphene via Thermal Annealing Graphite Oxide with Melamine and Its Excellent Electrocatalysis. *ACS Nano* **2011**, *5* (6), 4350–4358.

(274) Fan, Z.; Wang, K.; Wei, T.; Yan, J.; Song, L.; Shao, B. An Environmentally Friendly and Efficient Route for the Reduction of Graphene Oxide by Aluminum Powder. *Carbon* **2010**, *48* (5), 1686–1689.

(275) Zhang, J.; Yang, H.; Shen, G.; Cheng, P.; Zhang, J.; Guo, S. Reduction of Graphene Oxide via l - Ascorbic Acid. *Chem. Commun.* **2010**, *46* (7), 1112–1114.

(276) Acik, M.; Lee, G.; Mattevi, C.; Chhowalla, M.; Cho, K.; Chabal, Y. J. Unusual Infrared-Absorption Mechanism in Thermally Reduced Graphene Oxide. *Nat. Mater.* **2010**, *9* (10), 840–845.

(277) Shao, Y.; Wang, J.; Engelhard, M.; Wang, C.; Lin, Y. Facile and Controllable Electrochemical Reduction of Graphene Oxide and Its Applications. *J. Mater. Chem.* **2010**, *20* (4), 743–748.

(278) Toh, S. Y.; Loh, K. S.; Kamarudin, S. K.; Daud, W. R. W. Graphene Production via Electrochemical Reduction of Graphene Oxide: Synthesis and Characterisation. *Chem. Eng. J.* **2014**, *251*, 422–434.

(279) Huang, L.; Liu, Y.; Ji, L.-C.; Xie, Y.-Q.; Wang, T.; Shi, W.-Z. Pulsed Laser Assisted Reduction of Graphene Oxide. *Carbon* **2011**, *49* (7), 2431–2436.

(280) Trusovas, R.; Ratautas, K.; Račiukaitis, G.; Barkauskas, J.; Stankevičienė, I.; Niaura, G.; Mažeikienė, R. Reduction of Graphite Oxide to Graphene with Laser Irradiation. *Carbon* **2013**, *52*, 574–582.

(281) Cote, L. J.; Cruz-Silva, R.; Huang, J. Flash Reduction and Patterning of Graphite Oxide and Its Polymer Composite. *J. Am. Chem. Soc.* **2009**, *131* (31), 11027–11032.

(282) Jolivet, E.; Ivankovic, A.; Hsu, V.; Baron, N. *Embedded Dies & Interconnects, Substrates like PCB Trends*; Status of Advanced Substrates; Yole Développement, 2018.

(283) Chen, K.-N.; Tu, K.-N. Materials Challenges in Three-Dimensional Integrated Circuits. *MRS Bull.* **2015**, *40* (3), 219–222.

(284) Fontaine, R. Recent Innovations in CMOS Image Sensors. In *2011 IEEE/SEMI Advanced Semiconductor Manufacturing Conference*; 2011; pp 1–5.

(285) El-Kady, M. F.; Strong, V.; Dubin, S.; Kaner, R. B. Laser Scribing of High-Performance and Flexible Graphene-Based Electrochemical Capacitors. *Science* **2012**, *335* (6074), 1326–1330.

(286) Zhang, Y.; Guo, L.; Wei, S.; He, Y.; Xia, H.; Chen, Q.; Sun, H.-B.; Xiao, F.-S. Direct Imprinting of Microcircuits on Graphene Oxides Film by Femtosecond Laser Reduction. *Nano Today* **2010**, *5* (1), 15–20.

(287) Qiao, Y.-C.; Wei, Y.-H.; Pang, Y.; Li, Y.-X.; Wang, D.-Y.; Li, Y.-T.; Deng, N.-Q.; Wang, X.-F.; Zhang, H.-N.; Wang, Q. Graphene Devices Based on Laser Scribing Technology. *Jpn. J. Appl. Phys.* **2018**, *57* (4S), 04FA01.

(288) Kim, S.; Kulkarni, D. D.; Davis, R.; Kim, S. S.; Naik, R. R.; Voevodin, A. A.; Russell, M.; Jang, S. S.; Tsukruk, V. V.; Fedorov, A. G. Controlling the Physicochemical State of Carbon on Graphene Using Focused Electron-Beam-Induced Deposition. *ACS Nano* **2014**, *8* (7), 6805–6813.

(289) Bell, D. C.; Lemme, M. C.; Stern, L. A.; Williams, J. R.; Marcus, C. M. Precision Cutting and Patterning of Graphene with Helium Ions. *Nanotechnology* **2009**, *20* (45), 455301.

(290) Lobo, D. E.; Fu, J.; Gengenbach, T.; Majumder, M. Localized Deoxygenation and Direct Patterning of Graphene Oxide Films by Focused Ion Beams. *Langmuir* **2012**, *28* (41), 14815–14821.

(291) Rockwood, D. N.; Preda, R. C.; Yücel, T.; Wang, X.; Lovett, M. L.; Kaplan, D. L. Materials Fabrication from Bombyx Mori Silk Fibroin. *Nat. Protoc.* **2011**, *6* (10), 1612–1631.

(292) Moon, I. K.; Lee, J.; Ruoff, R. S.; Lee, H. Reduced Graphene Oxide by Chemical Graphitization. *Nat. Commun.* **2010**, *1*, 73.

(293) Xu, B.; Yue, S.; Sui, Z.; Zhang, X.; Hou, S.; Cao, G.; Yang, Y. What Is the Choice for Supercapacitors: Graphene or Graphene Oxide? *Energy Environ. Sci.* **2011**, *4* (8), 2826–2830.

(294) Yu, H.; Wu, J.; Fan, L.; Xu, K.; Zhong, X.; Lin, Y.; Lin, J. Improvement of the Performance for Quasi-Solid-State Supercapacitor by Using PVA–KOH–KI Polymer Gel Electrolyte. *Electrochimica Acta* **2011**, *56* (20), 6881–6886.

(295) Yang, C.-C.; Hsu, S.-T.; Chien, W.-C. All Solid-State Electric Double-Layer Capacitors Based on Alkaline Polyvinyl Alcohol Polymer Electrolytes. *J. Power Sources* **2005**, *152*, 303–310.

(296) Nohara, S.; Wada, H.; Furukawa, N.; Inoue, H.; Morita, M.; Iwakura, C. Electrochemical Characterization of New Electric Double Layer Capacitor with Polymer Hydrogel Electrolyte. *Electrochimica Acta* **2003**, *48* (6), 749–753.

(297) Iwakura, C.; Wada, H.; Nohara, S.; Furukawa, N.; Inoue, H.; Morita, M. New Electric Double Layer Capacitor with Polymer Hydrogel Electrolyte. *Electrochem. Solid-State Lett.* **2003**, *6* (2), A37–A39.

(298) Verbrugge, M. W.; Liu, P. Analytic Solutions and Experimental Data for Cyclic Voltammetry and Constant-Power Operation of Capacitors Consistent with HEV Applications. *J. Electrochem. Soc.* **2006**, *153* (6), A1237–A1245.

(299) Gu, W.; Sevilla, M.; Magasinski, A.; Fuertes, A. B.; Yushin, G. Sulfur-Containing Activated Carbons with Greatly Reduced Content of Bottle Neck Pores for Double-Layer Capacitors: A Case Study for Pseudocapacitance Detection. *Energy Environ. Sci.* **2013**, *6* (8), 2465–2476.

(300) Franssila, S. *Introduction to Microfabrication*; John Wiley & Sons, 2010.

(301) Kiddee, P.; Naidu, R.; Wong, M. H. Electronic Waste Management Approaches: An Overview. *Waste Manag.* **2013**, *33* (5), 1237–1250.

(302) Premalatha, M.; Tabassum-Abbasi; Abbasi, T.; Abbasi, S. A. The Generation, Impact, and Management of E-Waste: State of the Art. *Crit. Rev. Environ. Sci. Technol.* **2014**, *44* (14), 1577–1678.

(303) Wu, C.; Wang, X.; Lin, L.; Guo, H.; Wang, Z. L. Paper-Based Triboelectric Nanogenerators Made of Stretchable Interlocking Kirigami Patterns. *ACS Nano* **2016**, *10* (4), 4652–4659.

(304) Tang, Y.; Lin, G.; Yang, S.; Yi, Y. K.; Kamien, R. D.; Yin, J. Programmable Kiri-Kirigami Metamaterials. *Adv. Mater.* **2017**, *29* (10).

(305) Wang, W.; Li, C.; Rodrigue, H.; Yuan, F.; Han, M.-W.; Cho, M.; Ahn, S.-H. Kirigami/Origami-Based Soft Deployable Reflector for Optical Beam Steering. *Adv. Funct. Mater.* **2017**, *27* (7).

(306) Xu, L.; Shyu, T. C.; Kotov, N. A. Origami and Kirigami Nanocomposites. *ACS Nano* **2017**, *11* (8), 7587–7599.

(307) Jiang, H.; Khang, D.-Y.; Song, J.; Sun, Y.; Huang, Y.; Rogers, J. A. Finite Deformation Mechanics in Buckled Thin Films on Compliant Supports. *Proc. Natl. Acad. Sci.* **2007**, *104* (40), 15607–15612.

(308) Luo Chong; Yeh Che-Ning; Baltazar Jesus M. Lopez; Tsai Chao-Lin; Huang Jiaxing. A Cut-and-Paste Approach to 3D Graphene-Oxide-Based Architectures. *Adv. Mater.* **2018**, *0* (0), 1706229.

(309) Rui, X.; Kim, H. S.; Zhang, S.; Kim, S.; Korolovych, V. F.; Ma, R.; Yingling, Y. G.; Ly, C.; Tsukruk, V. V. Template-Guided Assembly of Silk Fibroin on Cellulose Nanofibers for Robust Nanostructures with Ultrafast Water Transport. *ACS Nano Submitt.*

(310) Ye, C.; Combs, Z. A.; Calabrese, R.; Dai, H.; Kaplan, D. L.; Tsukruk, V. V. Robust Microcapsules with Controlled Permeability from Silk Fibroin Reinforced with Graphene Oxide. *Small* **2014**, *10* (24), 5087–5097.

(311) Zhang, Y.; Gong, S.; Zhang, Q.; Ming, P.; Wan, S.; Peng, J.; Jiang, L.; Cheng, Q. Graphene-Based Artificial Nacre Nanocomposites. *Chem. Soc. Rev.* **2016**, *45* (9), 2378–2395.

(312) Yeh, C.-N.; Raidongia, K.; Shao, J.; Yang, Q.-H.; Huang, J. On the Origin of the Stability of Graphene Oxide Membranes in Water. *Nat. Chem.* **2015**, *7* (2), 166–170.

(313) Cong, H.-P.; Ren, X.-C.; Wang, P.; Yu, S.-H. Flexible Graphene –Polyaniline Composite Paper for High-Performance Supercapacitor. *Energy Environ. Sci.* **2013**, *6* (4), 1185–1191.

(314) David, L.; Bhandavat, R.; Barrera, U.; Singh, G. Silicon Oxycarbide Glass-Graphene Composite Paper Electrode for Long-Cycle Lithium-Ion Batteries. *Nat. Commun.* **2016**, *7*, 10998.

(315) Cao, J.; Chen, C.; Zhao, Q.; Zhang, N.; Lu, Q.; Wang, X.; Niu, Z.; Chen, J. A Flexible Nanostructured Paper of a Reduced Graphene Oxide–Sulfur Composite for High-Performance Lithium–Sulfur Batteries with Unconventional Configurations. *Adv. Mater.* **2016**, *28* (43), 9629–9636.

(316) Chi, K.; Zhang, Z.; Xi, J.; Huang, Y.; Xiao, F.; Wang, S.; Liu, Y. Freestanding Graphene Paper Supported Three-Dimensional Porous Graphene–Polyaniline Nanocomposite Synthesized by Inkjet Printing and in Flexible All-Solid-State Supercapacitor. *ACS Appl. Mater. Interfaces* **2014**, *6* (18), 16312–16319.

(317) Liu, F.; Song, S.; Xue, D.; Zhang, H. Folded Structured Graphene Paper for High Performance Electrode Materials. *Adv. Mater.* **2012**, *24* (8), 1089–1094.

(318) Hodge, R. M.; Bastow, T. J.; Edward, G. H.; Simon, G. P.; Hill, A. J. Free Volume and the Mechanism of Plasticization in Water-Swollen Poly(Vinyl Alcohol). *Macromolecules* **1996**, *29* (25), 8137–8143.

(319) Chamarthy, S. P.; Diringer, F. X.; Pinal, R. The Plasticization-Antiplasticization Threshold of Water in Microcrystalline Cellulose: A Perspective Based on Bulk Free Volume. In *Water Properties in Food, Health, Pharmaceutical and Biological Systems: ISOPOW 10*; President, D. S. R., Sajjaanantakul, T., Lillford, P. J., Charoenrein, S., Eds.; Wiley-Blackwell, 2010; pp 297–314.

(320) Kang, S. H.; Shan, S.; Košmrlj, A.; Noorduin, W. L.; Shian, S.; Weaver, J. C.; Clarke, D. R.; Bertoldi, K. Complex Ordered Patterns in Mechanical Instability Induced Geometrically Frustrated Triangular Cellular Structures. *Phys. Rev. Lett.* **2014**, *112* (9), 098701.

(321) Pei, S.; Cheng, H.-M. The Reduction of Graphene Oxide. *Carbon* **2012**, *50* (9), 3210–3228.

(322) Yang, Y.; Zhang, H.; Chen, J.; Jing, Q.; Zhou, Y. S.; Wen, X.; Wang, Z. L. Single-Electrode-Based Sliding Triboelectric Nanogenerator for Self-Powered Displacement Vector Sensor System. *ACS Nano* **2013**, *7* (8), 7342–7351.

(323) Kwak, S. S.; Kim, H.; Seung, W.; Kim, J.; Hinchet, R.; Kim, S.-W. Fully Stretchable Textile Triboelectric Nanogenerator with Knitted Fabric Structures. *ACS Nano* **2017**, *11* (11), 10733–10741.

(324) Yang, Y.; Zhou, Y. S.; Zhang, H.; Liu, Y.; Lee, S.; Wang, Z. L. A Single-Electrode Based Triboelectric Nanogenerator as Self-Powered Tracking System. *Adv. Mater.* **2013**, *25* (45), 6594–6601.

(325) Lai Ying-Chih; Deng Jianan; Niu Simiao; Peng Wenbo; Wu Changsheng; Liu Ruiyuan; Wen Zhen; Wang Zhong Lin. Electric Eel-Skin-Inspired Mechanically Durable and Super-Stretchable Nanogenerator for Deformable Power Source and Fully Autonomous Conformable Electronic-Skin Applications. *Adv. Mater.* **2016**, *28* (45), 10024–10032.

(326) Yang, Y.; Zhang, H.; Lin, Z.-H.; Zhou, Y. S.; Jing, Q.; Su, Y.; Yang, J.; Chen, J.; Hu, C.; Wang, Z. L. Human Skin Based Triboelectric Nanogenerators for Harvesting Biomechanical Energy and as Self-Powered Active Tactile Sensor System. *ACS Nano* **2013**, *7* (10), 9213–9222.

(327) Liu Guanlin; Chen Jie; Tang Qian; Feng Li; Yang Hongmei; Li Jien; Xi Yi; Wang Xue; Hu Chenguo. Wireless Electric Energy Transmission through Various Isolated Solid Media Based on Triboelectric Nanogenerator. *Adv. Energy Mater.* **2018**, *0* (0), 1703086.